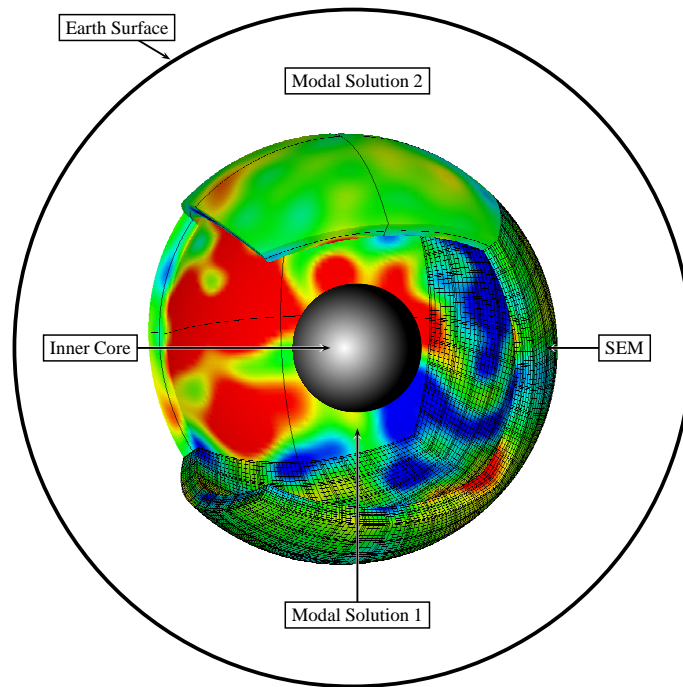


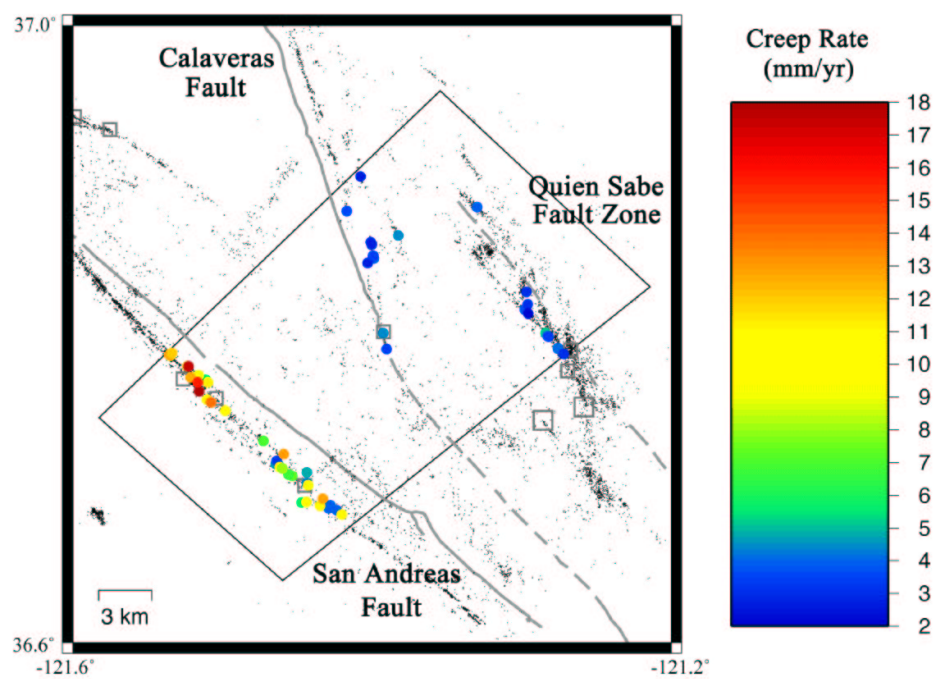
Part III

Ongoing Research Projects



Chapter 15

Source and Geodetic Studies



1. Parkfield Research

R.M. Nadeau, L.R. Johnson, A. Michelini (CRS, Italy), T.V. McEvelly, H.-R. Wenk

1.1 Introduction

The HRSN at Parkfield (Chapter 6) was installed in 1987 to provide a direct test of two hypotheses critical to our understanding of the physics of the earthquake process, with implications for earthquake hazard reduction and the possibilities for short-term earthquake prediction - major goals of the NEHRP:

1) That the earthquake nucleation process produces stress-driven perturbations in physical properties of the rocks in the incipient focal region that are measurable, and

2) That the nucleation process involves progressive and systematic failure that should be observable in the ultralow-magnitude microseismicity ($-1 < M < 2$) with high-resolution locations and source mechanisms.

Analyses of the 14+ years of Parkfield monitoring data have revealed significant and unambiguous departures from stationarity both in the seismicity characteristics and in wave propagation details. Within the presumed M6 nucleation zone we also have found a high V_p/V_s anomaly at depth, where the three M 4.7-5.0 sequences occurred in 1992-94. Synchronous changes well above noise levels have also been seen among several independent parameters, including seismicity rates, average focal depth, S-wave coda velocities, characteristic sequence recurrence intervals, fault creep and water levels in monitoring wells. We have been able to localize the S-coda travel-time changes to the shallow part of the fault zone and demonstrate with numerical modeling the likely role of fluids in the phenomenon. We can connect the changes in seismicity to slip-rate variations evident in other (strain, water level) monitored phenomena. Based on the ubiquitous clusters of repeating microearthquakes, scaling laws have been developed that can be projected to fit earthquakes up to M6, and they predict unprecedented high stress drops and melting on the fault surface for the smallest events. Exhumed fault-zone rocks provide independent evidence for such source conditions. This hypothesis is being debated vigorously in the current literature. Recurrence interval variations in the characteristic event sequences (about one-third of the microearthquake population) have been used to map fault slip rate at depth on the fault surface, and this technique appears to be applicable to other types of faults. Along the way in this exciting discovery process we have challenged the conventional 'constant stress drop' source model, affirmed characteristic earthquake occurrence and developed four-dimensional maps of fault-zone microearthquake processes at the un-

precedented scale of a few meters. The significance of these findings lies in their apparent coupling and interrelationships, from which models for fault-zone process can be fabricated and tested with time. A more fundamental contribution of the project is its production of a continuous baseline, at very high resolution, of both the microearthquake pathology and the subtle changes in wave propagation, providing to the seismological community a dynamic earthquake laboratory available nowhere else. This unique body of observations and analyses has also provided much of the impetus for Parkfield as the preferred site for deep drilling into an active seismogenic fault zone (the SAFOD project), and we have upgraded and expanded the network to improve its view of the drilling target zone on the fault surface.

1.2 Recent BSL/Collaborative Research

Over the past year, data and previously derived theoretical and empirical relationships from Parkfield have served as a basis for investigations on a variety of topics by BSL researchers and collaborators at the Department of Terrestrial Magnetism (Carnegie) and Lawrence Berkeley National Laboratory (LBNL).

Johnson and Nadeau (2002) developed an empirically based earthquake asperity model that explains previously determined earthquake scaling relationships from characteristically repeating earthquake sequences (CS) at Parkfield. Their model suggests fault strength to be highly heterogeneous.

Korneev et al. (2002) have used Fault Zone Guided Waves (FZGW) from HRSN recorded microearthquakes to image the structure of the innermost fault zone using FZGW attenuation.

Niu et al. (2002) have used Parkfield CS events as highly repeating illumination sources to reveal the stress-induced migration of scatterers of seismic energy. By examining the systematics of temporal changes in the coda arrivals of CS events and stress changes inferred from the evolution of deformation at Parkfield, they infer that stress-induced redistribution of fluids along fractures in or adjacent to the fault are taking place.

Using the scaling (Tr-Mo) of CS recurrence intervals (Tr) with seismic moments (Mo) (*Nadeau and Johnson*, 1998) and the its calibration with intermediate scale geodetic measurements at Parkfield, *Schmidt et al.* (2002) and *Nadeau and McEvelly* (2002) are mapping areas of deep fault slip and slip rates along the East Bay Area Hayward Fault and along the central creeping section of the San Andreas Fault (SAF) in California.

In ongoing investigations of the Tr-Mo scaling, BSL researchers have extended the range in Mo over which scaling occurs to over 15 orders of magnitude in Mo (Figure 15.1). This relationship serves as a basis for empirical determinations of earthquake source parameters of area (A), seismic slip (d), and stress drop (Nadeau and Johnson, 1998). These determinations involve relatively few model assumptions and are independent of existing models relating the shape and spectra of seismic waveforms to the mechanics of earthquake sources. Results of the CS based approach have implications that are significantly different from the standard models derived from the waveform base methods.

1.3 Impetus for External Research

Recently, several independent research groups external to Berkeley have attempted to explain the discrepancy between CS based and standard model scaling of source parameters by providing alternative interpretations to that of Nadeau and Johnson for the observed Tr-Mo (e.g. *Anooshehpour and Brune, 2001; Sammis and Rice, 2001; Beeler et al., 2001; Chen and Sammis, 2002*).

These interpretations involve mechanisms in which loading of the CS patches is magnitude dependent. For example, Beeler et al. have proposed a creep-slip mechanism to explain the Tr-Mo discrepancy at small Mo (10^{15} to 10^{18} dyne-cm); however, their model does not appear to provide a satisfactory explanation for Tr-Mo at intermediate Mo earthquakes (approx. magnitudes 1.5 to 5) nor for very small events (magnitudes < 0) (Figure 15.1).

Interpretations based on slip shielding arguments such as those of Sammis and Rice and Anooshehpour and Brune require CS to be located adjacent to or embedded within large locked patches. However, locations of CS appear to be widely distributed and usually well away from large locked zones (e.g. in the central creeping section of the SAF). Furthermore their relationships in the Tr-Mo scaling generally remain consistent with that expected from local geodetic loading rates regardless of proximity to large locked zones.

1.4 Related Research

A number of other recent studies have recognized the significance of the CS systematics and scaling found at Parkfield and have explored their implications from a variety of perspectives. For example with respect to high-precision relative relocations (*Waldhauser and Ellsworth, 2002; Rubin, 2002; Schaff et al., 2002*), and with respect to earthquake physics, seismicity variations and deformation rates along strike-slip and subducting faults in California and Japan (*Matsuzawa et al., 2002; Seno, 2002*).

1.5 SAFOD

Another principal focus of BSL's recent research at Parkfield has been the detailed analysis and monitoring of the characteristics of microseismicity within the drilling and penetration zone of the SAFOD component of the NSF initiative EarthScope. Of particular interest is the evolution of fault zone deformation and detailed seismic structure immediately surrounding the repeating SAFOD M2 target zone, and the recurrence behavior and size of the two potential M2 targets (separated by 70 m).

Using a 3-dimensional double-difference code developed by Alberto Michelini in Italy and a preexisting 3-D cubic splines interpolated velocity model developed from HRSN data (*Michelini and McEvilly, 1991*), we have been able to resolve the relative seismic structure in the target zone in great detail (Nadeau et al., 2001) (Figure 15.2). The relocations indicate that the subhorizontally drilled portion of the SAFOD hole may need to penetrate a seismically active (and the existence of CS imply actively slipping) strand some 300m to the SW before entering the M2 target region.

CS exist on both strands and slip rates on the strands inferred from the Tr of the CS in the strands indicate that both are slipping at about 10 to 15 mm/yr. This suggests a distinct possibility of shearing of the deep borehole casing on the SW strand which needs to be taken into account if long term monitoring of the local target is to take place.

The Tr-Mo relationship and ongoing monitoring of the Tr's of the CS local to the M2 target(s) can also be used to help estimate the expected occurrence time of the next M2 repeat (Figure 15.3). This information will be helpful in the planning of SAF penetration and monitoring efforts, as well as for testing of earthquake recurrence forecast models, and for evaluating the conditions surrounding the M2 target(s) leading up to failure.

The SAFOD experiment will also measure deformation along the deep hole which will provide a direct calibration of slip rates at depth with CS Tr's near the target zone. This will provide ground truth for interpretation of the Tr-Mo relationship, and is crucial for establishing an accurate model of CS recurrence behavior, for interpreting Tr-Mo based source parameter scaling relationships, for the extrapolation of fault and earthquake physics based on the Tr-Mo scaling, and for application of the CS deep fault slip rate method to slipping faults generally.

In regards to the drilling operation, the calibration will also provide a better picture of the M2 target size by providing a more accurate estimate of the partitioning of Mo from the expected M2 event ($Mo = \mu dA$) into its seismic slip (d) and rupture area (A) dimensions. Currently, estimates of the dimensions of the M2 target(s) vary significantly depending on the expected stress drop of the M2 events on the patch. Figure 15.4 shows the 2 potential M2 targets and estimated target sizes based on

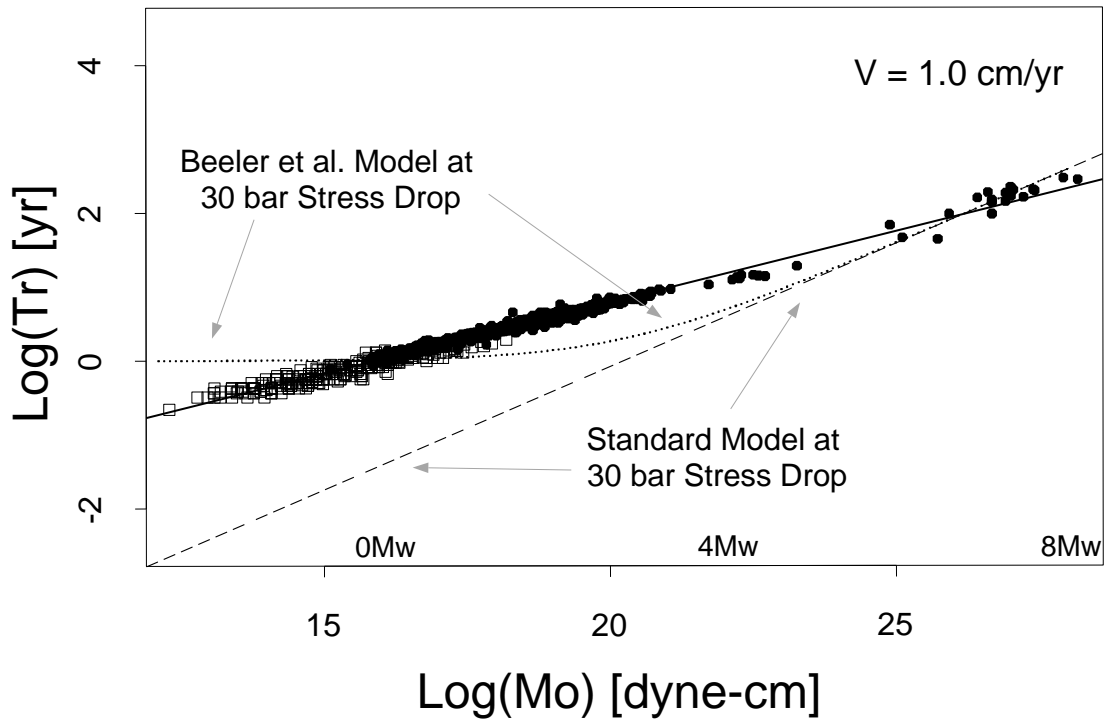


Figure 15.1: Log characteristic sequence recurrence time versus seismic moment normalized to a fault loading rate of 1 cm/yr. Filled circles show data for modern and historical characteristic events in California. Open squares are inferred T_r and M_o of fossil earthquakes (pseudotachylites) near Palm Desert California. Black line is a least squares fit to the characteristic earthquake data.

30 bar stress drop (from a standard constant stress drop model) and 2700 bar stress drop suggested by the T_r - M_o scaling (Nadeau and Johnson, 1998).

More information about the SAFOD project is available on the Web at: <http://www.icdp-online.de/html/sites/sanandreas/objectives/objectives.html> and <http://www.icdp-online.de/html/sites/sanandreas/objectives/proposal.html>

1.6 Acknowledgements

We appreciate support for this project by the USGS NEHRP through grant numbers 01HQGR0057 and 02HQGR0067 and by the NSF through award number 9814605.

1.7 References

Anooshehpour, A. and J.N. Brune, Quasi-Static Slip-Rate Shielding by Locked and Creeping Zones as an Explanation for Small Repeating Earthquakes at Parkfield, *Bull. Seism. Soc. Am.*, *91*, 401-403, 2001.

Beeler, N.M., A simple stick-slip and creep-slip model for repeating earthquakes and its implication for micro-earthquakes at Parkfield, *Bull. Seism. Soc. Am.*, *91*, 1797-1804, 2001.

Burgmann, R., D. Schmidt, R.M. Nadeau, M. d'Alessio, E. Fielding, D. Manaker, T.V. McEvelly, and

M.H. Murray, Earthquake Potential along the Northern Hayward Fault, California, *Science*, *289*, 1178-1182, 2000.

Chen, Y. and C.G. Sammis, A Numerical Asperity Model for Repeating Earthquakes, *Bull. Seism. Soc. Am.*, submitted, 2002.

Johnson, L.R. and R.M. Nadeau, Asperity Model of an Earthquake-Static Problem, accepted, *Bull. Seism. Soc. Am.*, *92*, 672-686, 2002.

Karageorgi, E., R. Clymer and T.V. McEvelly, Seismological studies at Parkfield. II. Search for temporal variations in wave propagation using Vibroseis, *Bull. Seism. Soc. Am.*, *82*, 1388-1415, 1992.

Karageorgi, E.D., T.V. McEvelly and R.W. Clymer, Seismological Studies at Parkfield IV: Variations in controlled-source waveform parameters and their correlation with seismic activity, 1987-1994, *Bull. Seism. Soc. Am.*, *87*, 39-49, 1997.

Korneev, V.A., T.V. McEvelly and E.D. Karageorgi, Seismological Studies at Parkfield VIII: Modeling the Observed Controlled-Source Waveform Changes, *Bull. Seism. Soc. Am.*, *90*, 702-708, 2000.

Korneev, V.A., R.M. Nadeau and T.V. McEvelly, Seismological Studies at Parkfield IX: Fault Zone Imaging using Guided Wave Attenuation, *Bull. Seism. Soc. Am.*, submitted in revision, 2002.

Matsuzawa, T., T. Igarashi and A. Hasegawa, Char-

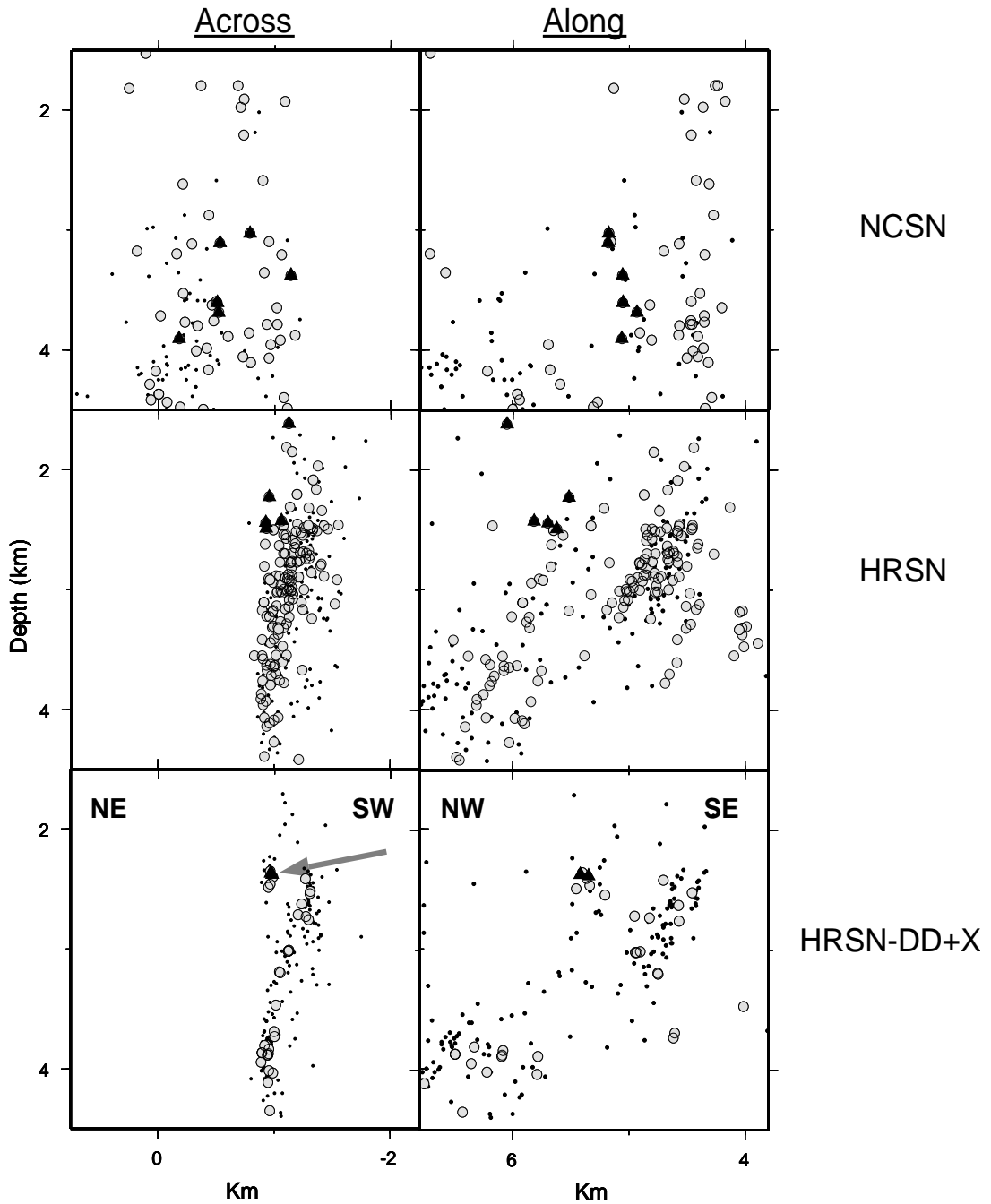


Figure 15.2: A 3x3 km region about the proposed SAFOD drilling target shown in along and across fault sections. Light grey circles show locations of 144 individual characteristically repeating micro-earthquakes from 31 sequences. Black triangles show locations of events from the 2 additional repeating M2 sequences proposed as SAF penetration targets by SAFOD. At lower resolution the repeating quake locations scatter widely. As resolution increases, their locations collapse onto the 33 sites of repeating activity shown in the bottom panels. Black dots are locations of non-repeating seismicity. Note the 2 strands of seismicity shown in the across fault section defining the NE and SW parallel strands. Both are populated with repeating earthquakes (indicating ongoing fault slip). The proposed drilling path direction at penetration (grey arrow) is subhorizontal from the SW to the NE into the M2 targets. Note that both M2 targets occur on the NE strand.

NEXT?!

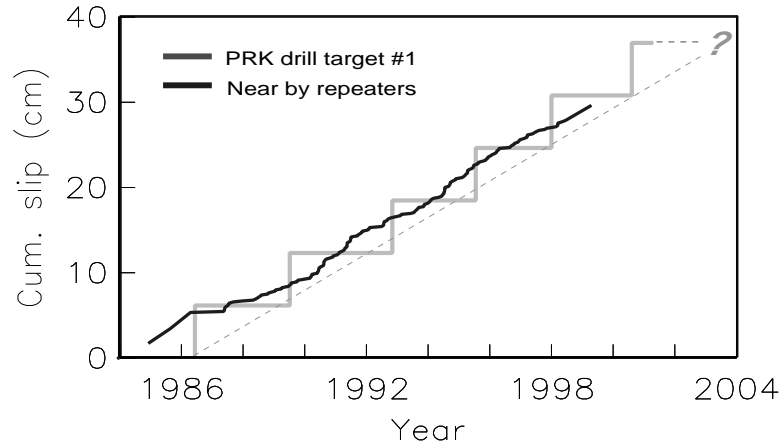


Figure 15.3: Cumulative slip release on characteristically repeating microearthquake sequence (CS) patches in the SAFOD M2 target zone. Gray steps show cumulative release of one of the 2 M2 target sites. Black curve shows cumulative slip of 33 near by CS occurring from 1987-1998.5 normalized to the number of near by CS used. Dashed line shows the average slip release rate of the M2 patch and "?" the approximate repeat date of the M2 target sometime in late 2003 or early 2004, assuming loading rates remain constant. Changes in loading rate on the M2 patch can be inferred from changes in slip release on the nearby patches and used to refine the expected repeat time of the M2.

acteristic Small-earthquake sequence off Sanriku, north-eastern Honshu, Japan, *Geophys. Res. Lett.*, in press, 2002.

Michelini, A. and T.V. McEvelly, Seismological studies at Parkfield I: Simultaneous inversion for velocity structure and hypocenters using B-splines parameterization, *Bull. Seism. Soc. Am.*, 81, 524-552, 1991.

Nadeau, R.M. and L. R. Johnson, Seismological Studies at Parkfield VI: Moment Release Rates and Estimates of Source Parameters for Small Repeating Earthquakes, *Bull. Seism. Soc. Am.*, 88, 790-814, 1998.

Nadeau, R.M., L.R. Johnson and H.-R. Wenk, Are Pseudotachylites Fossil Earthquakes?, *Seism. Res. Lett.*, submitted in revision, 2002.

Nadeau, R.M. and T. V. McEvelly, Seismological Studies at Parkfield V: Characteristic microearthquake sequences as fault-zone drilling targets, *Bull. Seism. Soc. Am.*, 87, 1463-1472, 1997.

Nadeau, R.M. and T.V. McEvelly, Fault slip rates at depth from recurrence intervals of repeating microearthquakes, *Science*, 285, 718-721, 1999.

Nadeau, R.M. and T.V. McEvelly, Spatial and Temporal Heterogeneity of Fault Slip from Repeating Micro-Earthquakes along the San Andreas Fault in Central California, *EOS Trans., Am. Geophys. Union.*, 81, F919, 2000.

Nadeau, R.M., T.V. McEvelly, and A. Michelini, hypocenter Locations at Parkfield and SAFOD Drilling Targets, *Seism. Res. Lett.*, 72, 277, 2001.

Nadeau, R.M. and T.V. McEvelly, Periodic Pulsing of the Tectonic Plate Boundary in Central California, in

prep., 2002.

Niu, F., P.G. Silver, R.M. Nadeau and T.V. McEvelly, Stress-Induced Migration of Seismic Scatterers Associated with the 1993 Parkfield Aseismic Transient, *Science*, submitted, 2002.

Rubin, A., Aftershocks of microearthquakes as probes of the mechanics of rupture, *J. Geophys. Res.*, 107, ESE3 1-16, 2002.

Sammis, C.G. and J.R. Rice, Repeating Earthquakes as Low-Stress-Drop Events at a Border Between Locked and Creeping Fault Patches, *Bull. Seism. Soc. AM.*, 91, 532-537, 2001.

Schaff, D.P., G.H.R. Bokelmann, G.C. Beroza, F. Waldhauser and W.L. Ellsworth, High Resolution Image of Calaveras Fault Seismicity, *J. Geophys. Res.*, in press, 2002.

Schmidt, D.A., R. Burgmann, R.M. Nadeau, and M. d'Alessio, Distribution of aseismic slip-rate on the Hayward fault inferred from seismic and geodetic data, *J. Geophys. Res.*, in prep., 2002.

Seno, T., Fractal asperities, invasion of barriers, and interplate earthquakes, *J. Geophys. Res.*, submitted, 2002.

Waldhauser, F. and W.L. Ellsworth, Fault structure and mechanics of the Hayward Fault, California, from double-difference earthquake locations, *J. Geophys. Res.*, 107, ESE3 1-15, 2002.

Wenk, H.-R., L.R. Johnson, and L. Ratschbacher, Pseudotachylites in the Eastern Peninsular Ranges of California, *Tectonophysics*, 321, 253-277, 2000.

Target Size

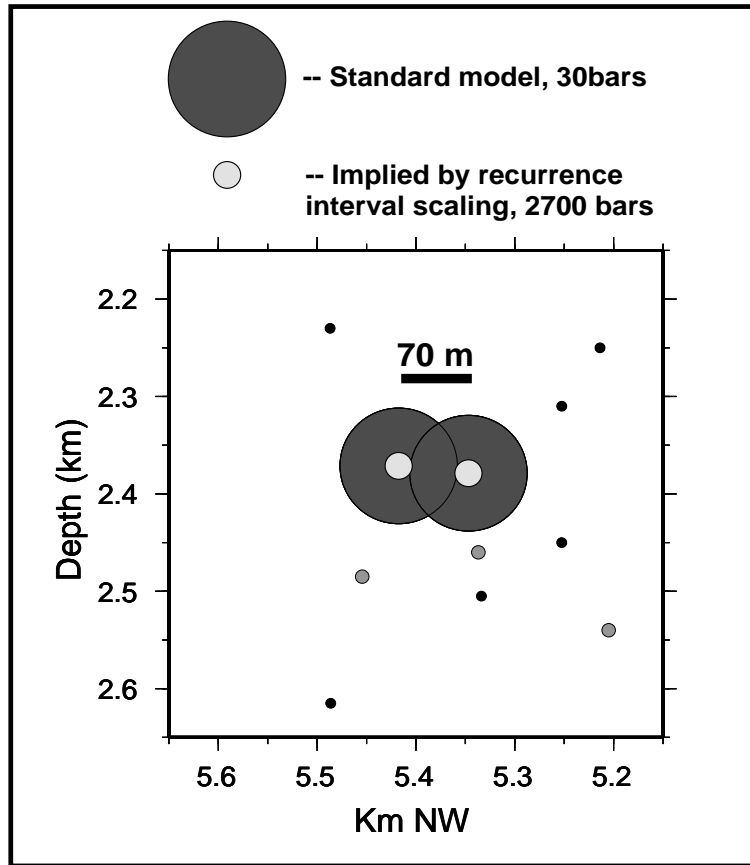


Figure 15.4: Potential M2 targets and estimated dimensions based on 30 bar and 2700 bar stress drops (large dark gray annuli and concentric light gray circles, respectively). Small black circles show near by non-repeating earthquake locations and small gray circles the locations of 3 close in CS, two of which occur on the fault strand some 300 m SW of the strand containing the M2 targets (see discussion in text). The potential targets locate only 70 m apart and yet rupture independently as separate repeated earthquake sequences. At 30 bars their inferred dimensions indicate significant overlap, making their independent rupture difficult to explain. Assuming 2700 bar stress drops, the M2 rupture patches are distinct and separated by some 50 m, making independent rupture more plausible. If patches are indeed this small, they present significantly smaller targets and will require very precise relative locations of the drill-bit relative to the patches in order to achieve monitoring, penetration and sampling of the M2 site as proposed by SAFOD.

2. Deep Fault Slip Kinematics from Characteristic Microearthquakes

R.M. Nadeau, D.C. Templeton, R. Burgmann, and T.V. McEvilly

2.1 Introduction

Analyses of the 14+ years of Parkfield monitoring data have revealed significant and unambiguous departures from stationarity both in the seismicity characteristics and in wave propagation details. Synchronous with these changes have been changes in the repeat times of characteristic microearthquake sequences, T_r , which have been related to slip loading rate variations at depth and which have been used to provide a 4-D image of the evolution of slip rates along the 25 km segment of the San Andreas Fault (SAF) spanning the presumed nucleation region of the next Parkfield M6 earthquake (Nadeau and McEvilly, 1999).

Our ongoing research is showing that this technique is applicable to other faults in Central California, and its more widespread application is revealing unexpected attributes of the kinematics of deformation along these faults and on scales ranging from a few meters to 100's of km.

T_r , is also a particularly well constrained observable that can be theoretically related to a variety of physical processes linked to earthquakes, fault structure, and fault deformation (e.g. overall fault strength, stress drops, fault heterogeneity, fault deformation at depth, slip loading of locked segments, fault healing rates, 'in-situ' friction, and event-event triggering). However to provide accurate measurements of these processes in an absolute sense, accurate calibrations between T_r and various constitutive properties within the fault core (e.g. composition, texture, temperature, stress, slip rate and fluid conditions) are needed. Currently such calibrations must be inferred from surface observations, laboratory experiments and seismic behavior. Ideally, however, they would come from 'in situ' measurement of the fault zone—an expensive proposition.

The National Science Foundation, through its EarthScope initiative (SAFOD component), has recently proposed careful scientific drilling into the seismogenic zone of the active San Andreas (SA) fault at Parkfield. Scientific drilling would sample fault zone properties directly and, as proposed, at the site of a repeating earthquake sequence. This effort promises to significantly enhance our understanding of the physics of of this portion of the SAF and to provide the calibration necessary for relating T_r to the constitutive properties and processes responsible for earthquakes and fault deformation at Parkfield.

At the same time EarthScope, through its PBO and InSAR components, has proposed to increase the detail and extent of deformation measurements along a ma-

ior plate boundary and throughout the country which should greatly improve estimates of fault slip from surface and space based observations. This information, together with the ongoing discovery of widely distributed repeating earthquake sequences in central CA make it feasible to extrapolate (infer) the physical conditions—relative to those found at Parkfield—on 100's of km of fault in central California and elsewhere.

Small repeating earthquakes continue to be discovered in other regions of the world and on other fault types (e.g. convergent boundaries off the coast of Japan (Matsuzawa *et al.*, 2002) and on normal faults in Greece (Dimitrief and McCloskey, 2000). This suggests the possibility of inferring fault conditions elsewhere.

In the U.S., it is conceivable that a collateral benefit of the USARRAY component of EarthScope will be the discovery of a significant number of new repeating earthquake sequences in regions where low magnitude seismicity has not been studied in detail. This has the potential to greatly expand the geographic coverage where inferential methods based on T_r can be applied.

The following subsections summarize the current state of repeating earthquake studies at Berkeley, and give examples of how such studies are already changing our understanding of the kinematics of fault deformation.

2.2 East Bay Faults

Method

The method of determining slip rates from earthquake recurrence has been developed in our research program using data from a borehole network along the active San Andreas fault zone at Parkfield, CA.

Studies at very high resolution of microearthquakes at Parkfield, CA since 1987 revealed a systematic organization in space and time, dominated by spatial clustering of nearly identical, regularly recurring microearthquakes ('characteristic events') on small (meters to 10s of meters) wide patches within the fault zone (Nadeau *et al.*, 1994, 1995; Nadeau and McEvilly, 1997). At Parkfield, nearly half of the 5000+ events in the 1987-1998 catalog exhibit this trait. In general, recurrence intervals (0.5 to 3 yr.) scale with the magnitude of the repeating events for the magnitude range available (M_w -0.7 to 3). Clusters of these characteristic events occur throughout the slipping fault surface. Scalar seismic moments were estimated for 268 micro-quakes contained in 53 repeating sequences and combined with equivalent estimates from 8 similar but larger event sequences from the Stone Canyon section of the fault and the main Parkfield M6 sequence.

These estimates show that seismic moment is being released as a function of time in a very regular manner where repeating earthquakes occur and for a wide range of earthquake magnitude. Measurements of the moment release rate, combined with an assumed tectonic loading rate, lead to estimates of the seismic parameters source area, slip, and recurrence interval. Such parameters exhibit a systematic dependence upon source size over a range of 10^{10} in seismic moment, which can be described by simple scaling relationships (*Nadeau and Johnson, 1998*). What emerges from this analysis of moment release rates is a quantitative description of an earthquake process that is controlled by small strong asperities that occupy less than 1% of the fault area.

A 26-months period of greatly increased activity during the study interval (M4.2, 4.6, 4.7 and 5.0 events and their aftershocks) accompanied changes exceeding 50% in previously stable recurrence intervals. *Langbein et al. (1999)* report on evidence in deformation measurements for a slip rate increase in 1993 at Parkfield. *Nadeau and McEvilly (1999)* show that it is possible under reasonable assumptions to infer the spatial distribution of variations in slip-rate on the fault surface from the changes in recurrence intervals for the characteristic event sequences. The analysis requires an assumption of constant area for the characteristic repeating sources - one easily supported by the lack of any appreciable change in the seismic moments and waveforms (over the 100 Hz bandwidth) associated with the change in recurrence interval.

Northern Hayward Fault

Along the northern Hayward Fault (HF) using surface short period NCSN catalog data, a prototype study using the micro-quake based deep fault slip technique was compared to an inversion of surface and space based geodetic data for fault slip. The comparison showed a good match between the two data types and formalization of joint inversion of the two data sets is currently underway. Results of our prototype study on the northern HF were encouraging and have been published in *Science (Burgmann et al., 2000)*. We have subsequently found sufficient repeating earthquake activity along the southern HF, Calaveras (CF) and Mission (MF) faults to determine deep fault slip rates on those faults as well.

A long enough time base of waveform data recorded on the deep borehole Hayward Fault Network (HFN) has also now become available which promises to allow practical application of the repeating quake method to repeating sequences of much lower magnitude and consequent greater temporal and spatial resolution.

Southern Hayward, Mission and Calaveras Faults

We have completed our initial and computationally intensive search for characteristic sequences on the southern HF, CF and MF faults, using surface NCSN data and

find that seismicity there resembles the clustering found at Parkfield, but at a lower seismicity rate and density. Figure 15.5 shows locations of the NCSN earthquakes that we focused on during the reconnaissance stage of our search for repeaters. This stage of processing characterizes the waveform similarity of all the event pairs separated by 7.5 km or less. Even at reduced catalog completeness (M 1.3) of the NCSN in this area, we see large numbers of highly similar and repeating events (coherency > 0.95) distributed widely on all three faults, indicating the presence of substantial repeating earthquake activity (Figure 15.5). Using NCSN surface data we estimate the fractions of identifiable repeaters to be about 10% 15% and 25%, for the northern HF, southern HF, MF and CF segments respectively.

The lowest fractions are explainable in part by lower slip rates and higher magnitude thresholds, since under these conditions recurrence intervals may be longer than observation times. At Parkfield, where the slip rate is much higher and using NCSN data, the fraction of repeaters is about 48%. In our prototype analysis on the northern HF, we showed that sufficient information was available to resolve spatially varying features of slip using surface NCSN data but that monitoring of short-term temporal variations was not practical with the limited resolution of the surface data on such a slowly moving fault. To the southeast, on the faster moving MF and CF, we are finding sufficient rates of quake repetition to allow us to use NCSN data for monitoring transients (Figure 15.5) as is currently being achieved on the faster slipping SAF to the West (*Nadeau and McEvilly, 2002*).

East-Bay Fault System

Using NCSN arrival times, we have relocated the seismicity along the HF-MF-CF system using the USGS relocation code HypoDD (Figure 15.5) and are evaluating the more highly resolved spatial and temporal seismicity patterns in relation to surface and spaced based deformation estimates, to the spatial and temporal distribution of repeating earthquake sequences and to the post-seismic period following the 1984 Morgan Hill earthquake. Our preliminary findings indicate that, as at Parkfield and on the creeping section of the SAF, the locations of repeating earthquake sequences are confined to the central portion of seismicity on large faults. However, repeating quakes are not ubiquitous on all faults.

For example our search for characteristic quakes in our study region failed to identify any repeating sequences on the CF fault north of its juncture with the MF trend between Fremont and San Jose (Figure 15.5). Furthermore, along the MF and southern HF, repeating sequences only appear in the shallow portion of the seismogenic zone and appear to delineate the proposed locked region of the Hayward fault which is presumably the generation zone of 1868 M7 type events (Figure 15.5). In addition,

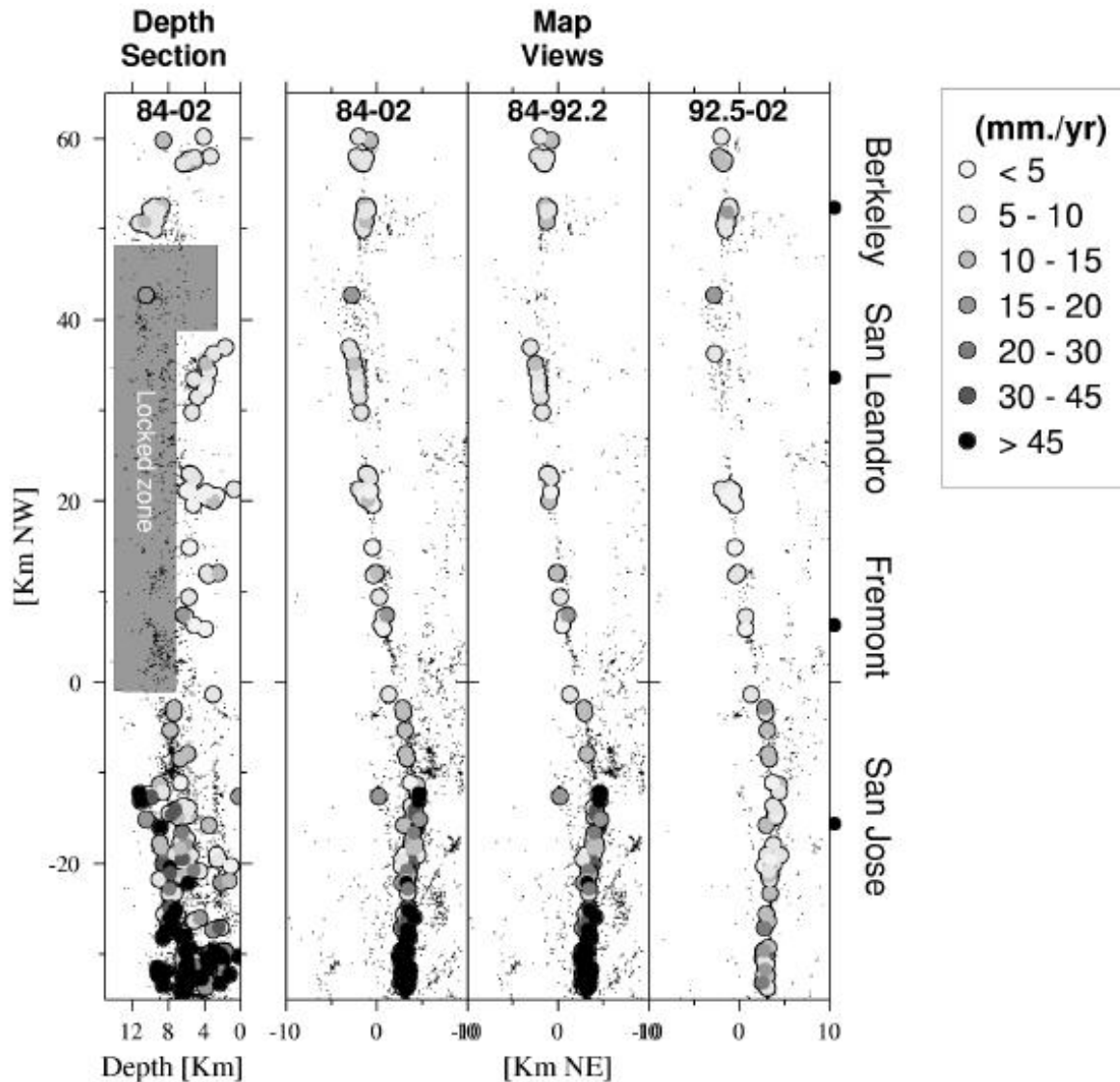


Figure 15.5: Point fault slip rate estimates at depth inferred from recurrence intervals of characteristic micro-earthquakes, superposed on the HypoDD-relocated seismicity along a 120-km-long stretch of the Hayward (HF), Mission (MF) and Calaveras (CF) faults. Locations of characteristically repeating sequences (CS) are shown as large filled (gray) circles. CS and are numerous, widespread and distributed in time and space along these mature actively creeping faults. Rates of slip inferred from the CS recurrence intervals in mm/yr are coded in gray scale as indicated. Black points show locations of non-CS seismicity. Each filled circle represents the average slip rate between time sequential pairs of characteristic events in a sequence. Variations in the rates of repetition are consistent with known variations in slip rate both along strike and through time as determined from surface and space based geodetic methods. For example, sequences NW of Morgan Hill (MH) typically show a steadily decreasing repeat rate with time since the 1984 MH magnitude 6. Left panel shows, in depth section, all slip rate pair estimates and background seismicity for the time period 1984-2002. Second panel shows the same data in map view. Panel three (second from right) shows data in map view for pairs occurring between 1984 to 1992.5, and far left map shows similar data for the period 1992.5 to 2002.2. A time variable slip rate is clear, particularly along the CF where slip rates are high following the 1984 Morgan Hill main shock and slow down significantly afterwards. Slip rate is lowest on the southern HF and MF trends. On these segments, below about 5-6 km, characteristically repeating sequences are absent while background seismicity can clearly be seen. This suggests that the boundary separating the repeating and non-repeating regions delineates the boundary between creeping and non-creeping (locked) fault behavior at depth on this fault system. The locked region of the system, as modeled by *Burgmann et al.*, (2000) shows a reasonable good match to this CS delineated region.

their rate of repetition (indicated by their low, very light gray, slip rates) are low relative to the slip rates on the northern HF and CF segments. Since repeating earthquake activity requires repeated loading from the adjacent slipping fault, we interpret the regions of seismically active but non-repeating seismicity to be non-creeping and locked and the low repeat rates of the shallow repeating sequences to be in response to the shielding effect of the deeper locked section of the southern HF and MF.

If this is the case, high resolution relocations of repeating earthquake activity may prove a valuable tool, generally, for delineating locked fault segment boundaries in more detail at depth. Also of note in this regard is the lack of repeating earthquake activity on two splays of transient earthquake activity emanating from the CF south of San Jose. High precision relocations show that these splays were active during the post-seismic period following the Morgan Hill (MH) earthquake of 1984, but in subsequent years these splays have become aseismic (Figure 15.5, map view, 84-92.5 and 92.5 to 2002). It is not yet clear if the lack of repeating sequences on these splays is due to a relatively minor amount of slip release on the faults after MH or to a fundamental instability in the strength properties of earthquake patches on these subsidiary faults.

In addition to the structural features manifest by the relocations and repeating earthquake analyses, temporal variations are also clearly evident. Shown in the right most panels of Figure 15.5 are map views of the repeating sequences, gray scale coded to their slip rate estimates. On the CF during the period 1984-1992.5 repeat rates (and inferred slip rates at depth) are very high in comparison to repeat rates for sequences from 1992.5 to 2002. In addition, repeating events on the southern HF during the 6 years following the Loma Prieta earthquake nearly ceased, which agrees well with diminished surface deformation rates observed on this fault segment (*Lienkaemper et al.*, 1997; *Burgmann et al.*, 1998).

Our ongoing efforts involve the determination of the the kinematics of slip through joint modeling of surface GPS, creep and space based data so that geologic questions regarding the details of slip in the complex of East Bay faults (particularly the Mission cross over region) can be investigated at much higher resolution (*Schmidt et al.*, (2002).

2.3 San Andreas, Calaveras Juncture

We have also applied similar relocation and repeating earthquake techniques further south in the CF and Quien Sabe fault near the bifurcation of the SAF where little surface or space based deformation data is available.

This juncture of the SAF and the southern CF is a highly complex area where subsurface seismicity does not always follow surface fault traces and where secondary sub-parallel faults, such as the Quien Sabe fault zone,

may play an active role in accommodating local shear deformation. The goal of this investigation is to determine the slip rate distribution of these faults at the juncture using repeating earthquake defined subsurface slip rates and surface geodetic measurements.

Currently we are investigating how slip at depth is being partitioned in this complex juncture zone, by determining a lower bound on creep rates at depth using characteristically repeating earthquakes (CREs) and the empirical formula of *Nadeau and McEvilly* (1999). Essentially, the method treats each CRE sequence as a "creep-meter" at depth, and derives slip from the direct relationship between an event's size and repeat interval relative to those found at Parkfield, CA.

In this region, the seismic structure and repeat rates of the characteristic sequences indicate a very complicated and heterogeneous slip regime apparently reflecting the complex fault geometry at depth, rapid slip transients initiated by moderate earthquakes, and the presence of a significantly greater fraction of locked (i.e. non-creeping) fault behavior (*Templeton et al.*, 2001).

We identified 58 CRE sequences (Figure 15.6). Using the double-difference relocation program HypoDD, we relocated the seismicity to see where in the fault zone the CREs were occurring. On the San Andreas and Calaveras faults, CRE sequences occur along the fault plane on horizontal linear streaks of seismicity. These streaks are more pronounced on the San Andreas than on the Calaveras fault. The smaller Quien Sabe fault zone is much more complex than the more mature San Andreas and Calaveras faults. On the northern end of the fault zone, there is only one CRE sequence which is found on one of three side stepping linear fault strands. On the southern part of the fault zone, fault structures become more complex with several fault strands branching off of the one linear fault strand which hosts most of the CRE sequences found on the Quien Sabe fault zone.

Some CRE sequences seemed to be influenced by larger nearby earthquakes, especially those found on fault traces that are discontinuous at depth. For example, on the Quien Sabe fault zone, sequences tended to cluster within approximately 3 km of larger earthquakes. Their recurrence intervals tended to be aperiodic and appeared to be influenced by the timing of larger nearby events. On the San Andreas and Calaveras faults, however, both periodically and aperiodically CRE sequences were found within approximately 3 km of larger earthquakes. We believe that aperiodically CRE sequences are indicating changes in the local stress regime due to the redistribution of stress caused by larger nearby earthquakes. We also showed that CRE recurrence intervals on the Calaveras and Quien Sabe fault zone tended to be larger than those on the San Andreas fault. This is due to the fact that the San Andreas fault is slipping at a much greater rate than the Quien Sabe fault zone and hence would

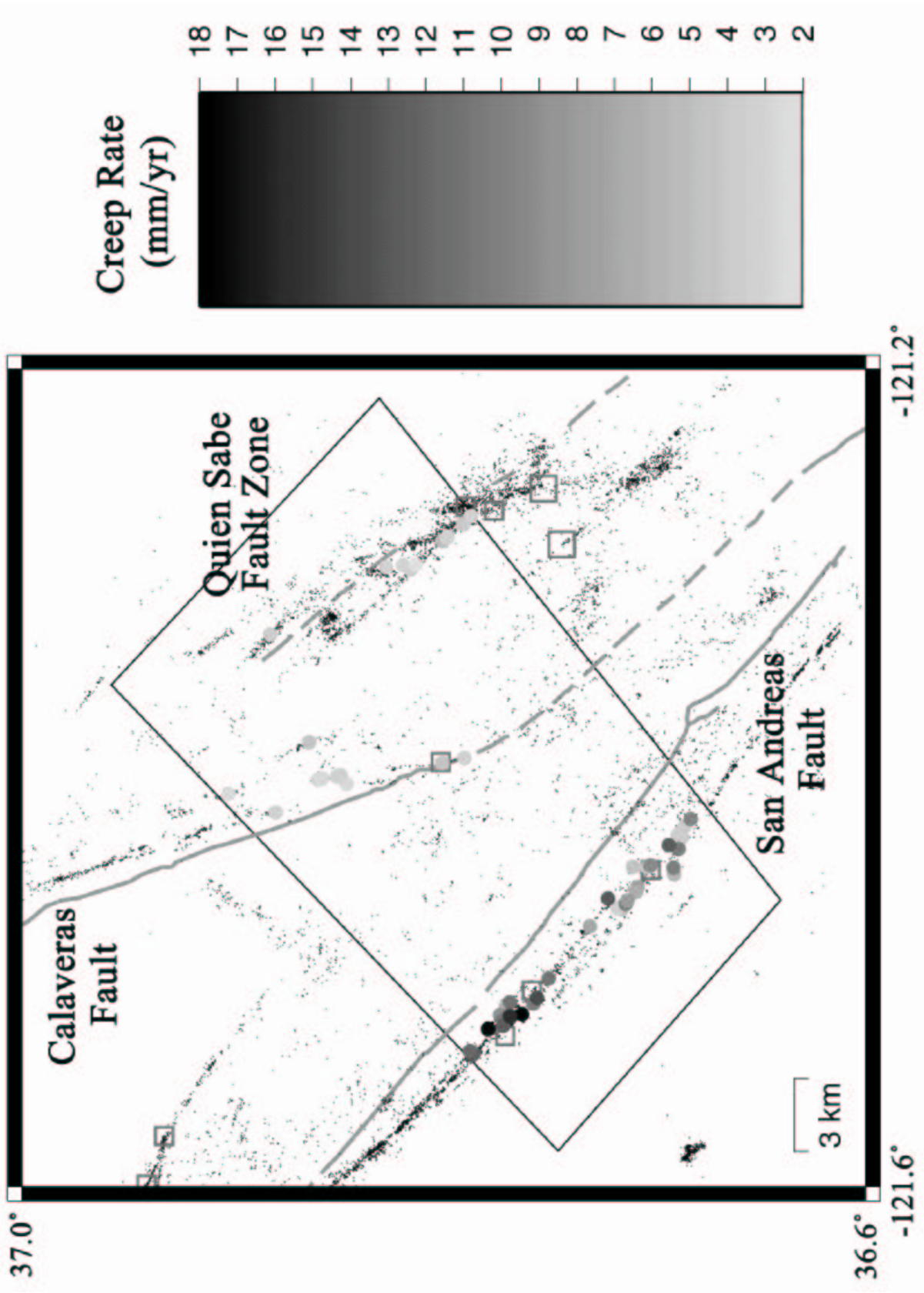


Figure 15.6: San Andreas, Calaveras Fault juncture zone. Location of CREs plotted as filled circles with gray shading scaled to estimated deep slip rates. Grey lines are surface expression of faults and squares indicate location of earthquakes greater than M4.0.

have a greater number of earthquakes over the same time interval.

Since only two or three events per CRE sequence were found on the Calaveras and Quien Sabe fault zone, we chose not to average the creep rates at individual sequence locations. Instead we calculated minimum creep rates. As we expected, creep on the Calaveras and Quien Sabe fault zone was lower, between 2.5-6.9 mm/yr, than that found on the San Andreas fault, between 3.2-18.0 mm/yr. We use these creep rates only as lower end members of creep along the fault trace. Interestingly, the smaller Quien Sabe fault zone seems to be creeping about the same amount as the more mature Calaveras fault in this location.

We plan to combine these subsurface creep rates with surface geodetic data to determine the subsurface creep rate distribution along the fault plane using a homogeneous, linear, elastic half-space model.

2.4 The SAF: Parkfield to Loma Prieta

As part of a more ambitious exploration of the extent to which characteristically repeating microearthquakes characterize active fault zones, we have applied the methodology developed at Parkfield (*Nadeau and McEvilly*, 1999) to examine deep slip rate along the San Andreas Fault from South of Parkfield to the Southern extent of rupture of the 1989 Loma Prieta (LP) earthquake from 1984 through 1999 using the NCSN event catalog.

Initial results are fascinating, revealing portions of the fault extending over many tens of kilometers that exhibit coherent pulsing in slip rate. In addition, the pulses appear closely related to the occurrence of the Loma Prieta earthquake in 1989 (*Nadeau and McEvilly*, 2002).

Relative quiescence on the northern end of the segment is observed prior to LP, after which slip rates increase markedly—the LP locked segment appears to have exerted control on the SAF slip rates at distances greater than 30 km from the termination of its rupture. Also of interest is the fact that LP occurred coincidentally with the initiation of an ongoing pulsing cycle some 40 to 80 km further to the South.

Following LP, the periodic pulsing observed to the South appears to extend northward and shows some correspondence to the occurrence of 3 slow silent quakes in the SJB area. The pulsing observed after LP also appears to be superposed on an exponential decay of slip rate corresponding to aftershock decay in the zone adjacent to and following the LP main event (upper right hand time history panel).

In the middle of the examined fault stretch, quasi-periodic pulsing of slip rates with amplitude variations exceeding 50-100 % are pronounced with the north central portion repeating with about 3 year periodicity and 1.7 year periodicity in the south central portion.

From 60 to about 20 km northwest of Parkfield, an apparent migration pulse is also observed. On this segment the SAF appears to act as a strain guide for the transference of the tectonic slip-load at a rate of about 25 km/yr. The migration pattern also appears to repeat itself as part of the more frequent (1.7 yr.) pulsing pattern.

To the South at Parkfield, pulsing is more difficult to define, although considerable slip rate change is observed, in accordance with observations of surface slip-rate change in that area (*Langbein et al.*, 1999). Also noteworthy at Parkfield is a distinct reduction in slip rate beginning after 1995 and continuing through 1999 that perhaps indicates a transition to a phase of relative slip quiescence preparatory to occurrence of the anticipated M6–similar to the quiescence observed prior to LP in the North.

2.5 Acknowledgements

We appreciate support for this project by the USGS NEHRP through grant numbers 01HQGR0066 and 02HQGR00226.

2.6 References

- Bryant, W.A., Faults in the southern Hollister area, San Benito counties, California, *California Division of Mines and Geology Fault Evaluation Report 164*, 1985.
- Burgmann, R., E. Fielding and J. Sukhatme, Slip along the Hayward fault, California, estimated from space-based synthetic aperture radar interferometry, *Geology*, *26*, 559-562, 1998.
- Burgmann, R., D. Schmidt, R.M. Nadeau, M. d'Alessio, E. Fielding, D. Manaker, T.V. McEvilly, and M.H. Murray, Earthquake Potential along the Northern Hayward Fault, California, *Science*, *289*, 1178-1182, 2000.
- Dimitrief, A. and J. McCloskey, A search for Repeating Microearthquakes in Western Greece (abstract), *EOS Trans. Am. Geophys. U.* *81*, F924, 2000.
- Langbein, J., R. Gwyther, R. Hart, and M.T. Gladwin, Slip rate increase at Parkfield in 1993 detected by high-precision EDM and borehole tensor strainmeters, *Geophys. Res. Lett.*, *26*, 2529-2532, 1999.
- Lienkaemper, J.J., J.S. Galehouse, and R.W. Simpson, Creep response of the Hayward fault to stress changes caused by the Loma Prieta earthquake, *Science*, *276*, 2014-2016, 1997.
- Matsuzawa, T., T. Igarashi and A. Hasegawa, Characteristic Small-earthquake sequence off Sanriku, northeastern Honshu, Japan, *Geophys. Res. Lett.*, in press, 2002.
- Nadeau, R.M., M. Antolik, P. Johnson, W. Foxall, and T.V. McEvilly, Seismological studies at Parkfield III: microearthquake clusters in the study of fault-zone dynamics, *Bull. Seism. Soc. Am.* *84*, 247-263, 1994.

Nadeau, R.M., W. Foxall, and T.V. McEvilly, Clustering and Periodic Recurrence of Microearthquakes on the San Andreas Fault at Parkfield, California, *Science*, 267, 503-507, 1995.

Nadeau, R.M. and T. V. McEvilly, Seismological Studies at Parkfield V: Characteristic microearthquake sequences as fault-zone drilling targets, *Bull. Seism. Soc. Am.*, 87, 1463-1472, 1997.

Nadeau, R.M. and L.R. Johnson, Seismological Studies at Parkfield VI: Moment Release Rates and Estimates of Source Parameters for Small Repeating Earthquakes, *Bull. Seism. Soc. Am.*, 88, 790-814, 1998.

Nadeau, R.M. and T.V. McEvilly, Fault slip rates at depth from recurrence intervals of repeating microearthquakes, *Science*, 285, 718-721, 1999.

Nadeau, R.M. and T.V. McEvilly, Periodic Pulsing of the Tectonic Plate Boundary in Central California, in prep., 2002.

Schmidt, D.A., R. Burgmann, R.M. Nadeau, and M. d'Alessio, Distribution of aseismic slip-rate on the Hayward fault inferred from seismic and geodetic data, *J. Geophys. Res.*, in prep., 2002.

Templeton, D.C., R.M. Nadeau and R. Burgmann, Structure and Kinematics at the Juncture between the San Andreas and Southern Calaveras faults, *Eos Trans. AGU*, 82, F811, 2001.

3. Time-dependent depth distribution of aftershocks: Implications for fault mechanics and crustal rheology

Frederique Rolandone, Roland Bürgmann, and Robert Nadeau

3.1 Introduction

A fundamental property of the continental upper crust is the depth distribution of earthquakes. The maximum depth of seismogenic faulting is interpreted either as the brittle-ductile transition, the transition from brittle faulting to plastic flow in the continental crust, or as the transition in the frictional sliding process from unstable to stable sliding. This transition depth depends on four main factors: rock composition, temperature, strain rate, and fluid pressure (e.g., *Sibson* 1982, 1984; *Meissner and Strehlau*, 1982; *Tse and Rice*, 1986; *Scholz*, 1990). Spatial variations in the maximum depth of seismicity in southern California have been correlated with crustal temperature or lithology (e.g., *Magistrale and Zhou*, 1996; *Williams et al.*, 2001). However, little has been done to examine how the maximum depth of seismogenic faulting varies locally (at the scale of a fault segment) with time during an earthquake cycle.

Many models assume a first-order transition from brittle to ductile deformation at a depth that is determined from regional estimates of the geotherm and strain rate. In the vicinity of a large fault this may be misleading because of the effects of strain localization. Strain rate values at depth around active faults are not known but recent mechanical models of strike-slip fault deformation (e.g., *Chery et al.*, 2001; *Rolandone and Jaupart*, 2002) show high strain rate localization around the base of the fault. Thus the brittle-ductile transition is not a sharp and fixed discontinuity in the crust but is expected to vary near the fault with strain rate and therefore to change with time through the earthquake cycle.

The objectives of this study are to apply high-resolution earthquake relocation techniques to resolve the time-dependent depth distribution of aftershocks and thus constrain models of the brittle-ductile transition and the rheology near the base of seismogenic faults.

3.2 Methodology

We investigate the time-dependent depth distribution of aftershocks following moderate to large earthquakes on strike-slip faults in southern California. Southern California offers a dense network of active strike-slip faults and high seismic activity. It is a very well instrumented area. Catalogs of seismicity provide a large observational time interval of seismicity records. We plan to examine the pattern of seismicity on different strike-slip fault segments to determine either spatially stable pattern (long-lived seismic structures) or systematic temporal varia-

tions related to recent earthquakes.

We use the 69-year catalog of the Southern California Seismic Network (SCSN) to identify target events. We use the catalog of relocated 1975-1998 earthquakes using the source specific station term method of *Richards-Dinger and Shearer* (2000), and the catalog of relocated events using a three-dimensional velocity model based on a joint-hypocenter-velocity (JHV) from 1981 to 2000 of *Hauksson* (2000) to do preliminary studies of aftershocks sequences.

Recently developed relative relocation techniques improve relative hypocenter locations (in favorable cases relative errors can be typically less than 20 m (*Waldhauser et al.*, 1999; *Waldhauser and Ellsworth*, 2000) and reveal greater details of the patterns of deformation during an earthquake cycle. We apply cross-correlation techniques and the double difference method of *Waldhauser and Ellsworth* (2000) to relocate earthquakes in the areas of interest (with the HypoDD relocation code).

3.3 Preliminary results

We begin this study analysing the seismicity around the 1987 Superstition Hills earthquake ($M_s=6.6$) as a first test case. Figure 15.7 shows a map view of the seismicity relocated using HypoDD around Superstition Hills for the time period 1983-2000. The inside box shows the zone of our study along the surface rupture of the earthquake.

We compare the time-dependent depth distribution of seismicity given by the different published catalogs (Figure 15.8). Figure 15.9 shows our relocated earthquake catalog for different velocity models. The different catalogs and our own relocation results show large variations of hypocentral depths. These variations seem mainly related to the choice of the velocity model for the upper crust. However, a persistent feature of the depth distribution of aftershocks is that in the immediate post-seismic period the aftershocks are deeper than the background seismicity and these deepest aftershocks become shallower with time following the mainshock. Preliminary analysis of other historic ruptures in the Mojave Desert show a similar pattern. In order to quantify these variations, we are working on obtaining a sharper picture of the time-dependent depth variation of the seismicity.

3.4 Future work

Temporal changes in depth of seismicity may serve to increase our knowledge of (1) the depth to which upper crustal deformation is coupled to deformation within the

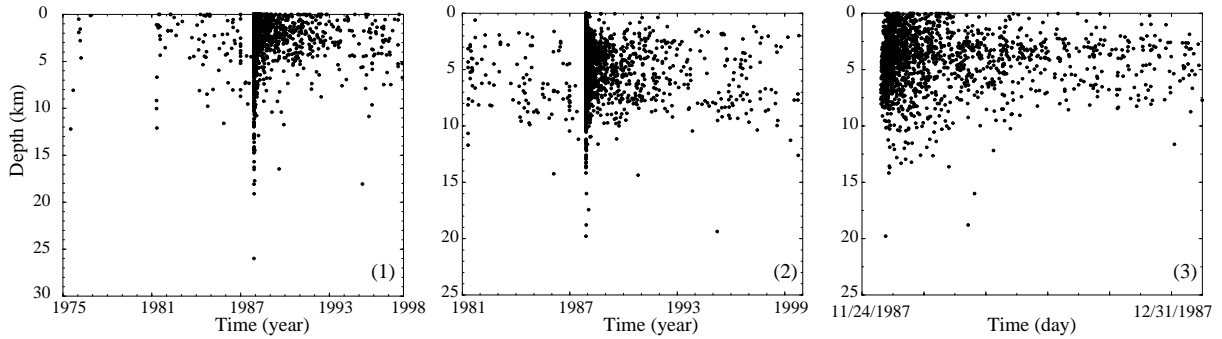


Figure 15.8: Time-dependent depth distribution of the seismicity from (1) the *Richards-Dinger and Shearer* catalog (2000), and from (2) the Hauksson catalog. (3) Detail of the distribution of seismicity from the Hauksson catalog from November 24 1987 to the end of 1987.

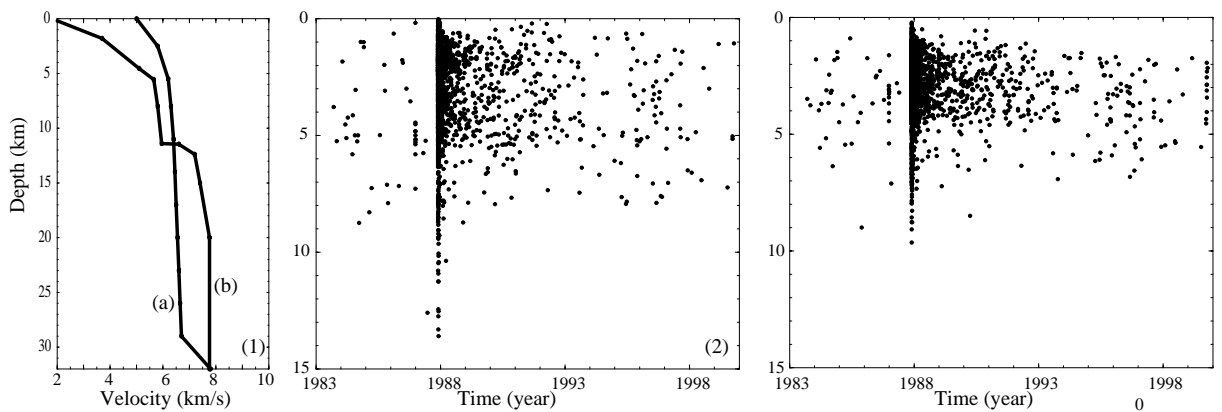


Figure 15.9: (1) Velocity structures used for relocation with HypoDD: (a) derived from *Shearer* (1997), (b) derived from *Fuis et al.* (1982). (2) Our relocation results obtained for velocity model (a), and (3) for velocity model (b). Note the difference in the depth scale with Figure 15.8.

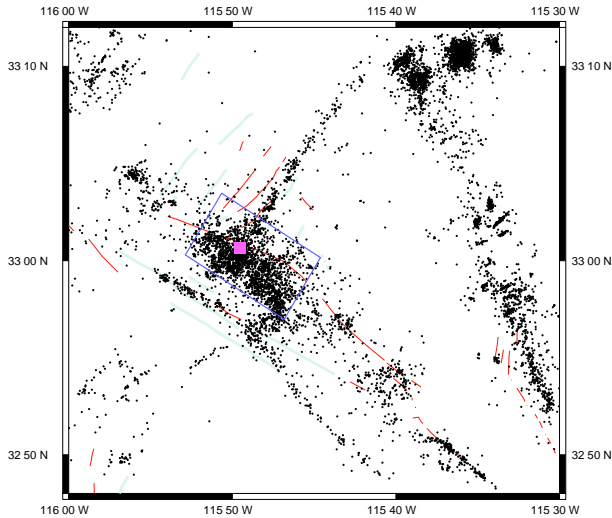


Figure 15.7: Seismicity (dots) around Superstition Hills from 1983 to 2000 relocated with HypoDD. The box indicates the seismicity used in this study around the surface rupture of the 1987 Superstition Hills earthquake (square). Active faults are shown.

lower crust, (2) the mechanics of fault zones near the base of the seismogenic zone where large earthquakes tend to nucleate and (3) of the transient deformation processes and their rheological parameters that are active during the postseismic period.

We are working on developing numerical finite-element models to compare these observations and the mechanical evolution of strike-slip faults and to infer fault slip and rheologic stratification. Our objective is to relate the depth distribution of hypocenters during an earthquake cycle to the evolution of the brittle-ductile transition to place constraints on strain rate at depth and on the partitioning of deformation between brittle faulting and distributed deformation.

3.5 References

Chery, J., M.D. Zoback, and R. Hassani, An integrated mechanical model of the San Andreas Fault in central and northern California, *J. Geophys. Res.*, *106*, 22,051-22,066, 2001.

Hauksson E., Crustal structure and seismicity distribution adjacent to the Pacific and North America plate boundary in southern California, *J. Geophys. Res.*, *105*, 13,875-13,903, 2000.

Magistrale, H. and H. Zhou, Lithologic control of the depth of earthquakes in southern California, *Science*, *273*, 639-642, 1996.

Meissner, R. and J. Strehlau, Limits of stresses in continental crusts and their relation to the depth-frequency distribution of shallow earthquakes, *Tectonics*, *1*, 73-79,

1982.

Richards-Dinger, K.B. and P. Shearer, Earthquake locations in southern California obtained using source-specific station terms, *J. Geophys. Res.*, *105*, 10,939-10,960, 2000.

Rolandone F. and C. Jaupart, The distribution of slip rate and ductile deformation in a strike-slip shear zone, *Geophys. J. Int.*, *148*, 179-192, 2002.

Scholz, C.H., The mechanics of earthquakes and faulting, pp. 439, *Cambridge University Press*, 1990.

Sibson, R.H., Fault zone models, heat flow, and the depth distribution of earthquakes in the continental crust of the United States, *Bull. Seismol. Soc. Am.*, *68*, 1421-1448, 1982.

Sibson, R.H., Roughness at the base of the seismogenic zone: contributing factors, *J. Geophys. Res.*, *89*, 5791-5799, 1984.

Tse, S.T. and J.R. Rice, Crustal earthquake instability in relation to the depth variation of frictional slip properties, *J. Geophys. Res.*, *91*, 9452-9472, 1986.

Waldhauser, F., W.L. Ellsworth, and A. Cole, Slip-parallel seismic lineations on the northern Hayward fault, California, *Geophys. Res. Lett.*, *26*, 3525-3528, 1999.

Waldhauser, F. and W. L. Ellsworth, A double-difference earthquake location algorithm: method and application to the northern Hayward fault, California, *Bull. Seismol. Soc. Am.*, *90*, 1353-1368, 2000.

Williams, C.F., L.A. Beyer, F.V. Grubb, S. Galanis, Heat Flow and the Seismotectonics of the Los Angeles and Ventura Basins of southern California, *Eos Trans. AGU*, *82(47)*, Fall Meet. Suppl., Abstract S11A-0534, 2001.

4. Moment-Length Scaling of Large Strike-Slip Earthquakes and the Strength of Faults

Barbara Romanowicz and Larry Ruff (University of Michigan)

4.1 Introduction

There has been a long lasting controversy in the literature as to whether earthquake moment (M_0) scales with L^2 or L for large earthquakes, where L is the length of the fault. In simple terms, the issue hinges on whether the average slip d during an earthquake grows with L or the width W of the fault. The issue of scaling is particularly important for seismic hazard estimation based on lengths of fault segments, since significantly different estimates of maximum possible earthquake size can be obtained for a given region, depending on the scaling law.

Several large strike slip earthquakes have occurred in various tectonic settings in the past 5 years, adding well documented data to the global collection of moment and length estimates for such earthquakes. Based on this augmented dataset, we have reexamined the controversial issue of scaling of seismic moment with length of rupture (Romanowicz and Ruff, 2002).

4.2 Background

Dislocation theory predicts that stress drop $\Delta\sigma$ is proportional to d/W , hence slip scales with W for constant $\Delta\sigma$. This implies scaling of M_0 with L^n , where $n = 3$ for small earthquakes and $n = 1$ for large earthquakes with $W = W_0$. Scholz (1982) proposed an alternative model, in which the slip scales with L . This model was motivated by inspection of slip versus length data that were available at that time. It implied that $n = 2$ for large earthquakes. On the other hand, Romanowicz (1992) compiled the existing dataset for large strike-slip earthquakes on quasi-vertical transcurrent faults. She concluded that moment scales with $n = 3$ for moments smaller than $\sim 0.6 - 0.8 \times 10^{20} Nm$, as known previously, while for larger moments, the data favored a scaling with $n = 1$, compatible with dislocation theory. Romanowicz and Rundle (1993) then showed, based on scale invariance arguments (e.g. Rundle, 1989), that the $n = 1$ and $n = 2$ scalings could also be differentiated on the basis of frequency-moment statistics, favoring of the "W-model".

Since then, the controversy has continued, using theoretical (e.g. Sornette and Sornette, 1994) as well as observational arguments (e.g. Pegler and Das, 1996; Mai and Beroza, 2000). On the other hand, new compilations of slip versus length data indicate that the increase of slip with L tapers off at large L (e.g. Bodin and Brune, 1996). This view has recently received further support from numerical modelling (Shaw and Scholz, 2001).

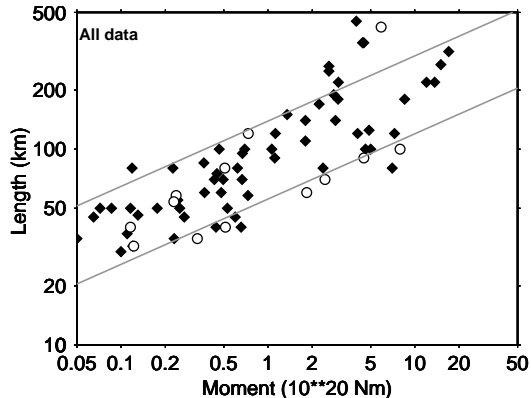


Figure 15.10: Moment-length plot for the dataset described. Lines corresponding to $n = 3$ bracketing most of the data have been drawn for reference. Circles correspond to recent data for which length was estimated from the NEIC catalog.

4.3 Dataset used

We considered the catalog of Pegler and Das (1996) (PD96 in what follows), who have combined M_0 estimates from the Harvard CMT catalog, with L for large earthquakes from 1977 to 1992 based on relocated 30-day aftershock zones. We add to this dataset the standard collection of reliable M_0/L data for large strike-slip earthquakes since 1900 (e.g. Romanowicz, 1992), data for great central Asian events since the 1920's (Molnar and Deng, 1984), as well as data for recent large strike-slip events (e.g. Balleny Islands '98; Izmit, Turkey '99 and Hector Mines, CA, '99) that have been studied using a combination of modern techniques (i.e. field observations, waveform modelling, aftershock relocation).

We also considered 15 other strike-slip events of moment $M_0 > 0.05 \times 10^{20} Nm$ that occurred in the period 1993-2001. Three of these events were recently studied by Henry and Das (2001), and we used their length estimates. For the other 12, we obtained estimates of length based on the distribution of aftershocks of $M > 4$ in the month following the event, as given in the NEIC contribution to the Council of National Seismic Systems (CNSS) catalog. We only kept those events with a clearly delineated aftershock zone.

4.4 Results and Conclusions

Most of the data follow the $n = 3$ trend, albeit with significant dispersion, except for the largest events (Fig-

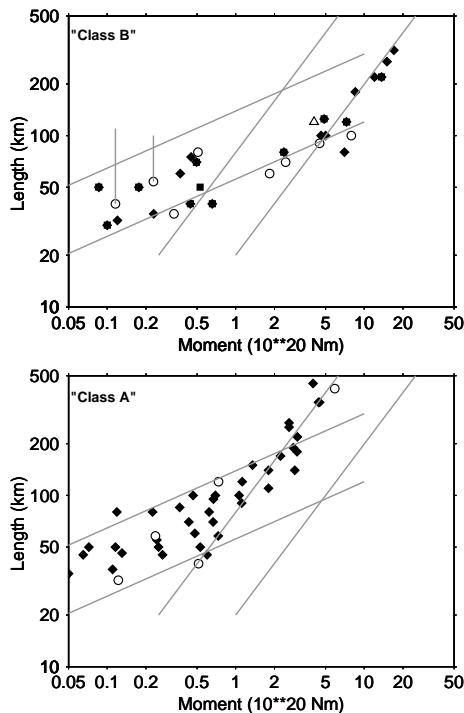


Figure 15.11: Moment-length plots for A (bottom) and B (top) events. Best fitting $n = 1$ trends are indicated for each subset of data. Circles as in Figure 1, diamonds from other sources. Triangle is Luzon'90 event. Vertical lines point to the length estimates of PD96 for Aegean Sea events

ure 15.10). We separated our dataset into two subsets: subset A comprises mostly events that occurred in a continental setting, and/or which, if their moment is larger than $1 \times 10^{20} Nm$, follow the trend of events on the San Andreas and Anatolian faults, on which the analysis of Romanowicz (1992) was based. The second subset ("B") comprises the 12 large "anomalous" events mentioned above, four great earthquakes in central Asia, as well as smaller events occurring in an oceanic setting. The resulting separate M_0/L plots are shown in Figure 15.11.

We infer that each data subset can be fit rather tightly with an $n = 1$ trend for the largest events. The change of scaling simply corresponds to a larger moment for events in subset B ($M_0 \sim 5 \times 10^{20} Nm$) than for those in subset A ($M_0 \sim 0.8 - 1 \times 10^{20} Nm$). For both subsets, the change in scaling occurs for $L \sim 80 km$. For smaller events, the dispersion is large, but, on average, the best fitting $n = 3$ trend plots lower for subset B.

This difference in the position of the break in scaling in each subset can originate either from a difference in W_o , or from a difference in $\Delta\sigma$. If we assume that W_o cannot be much larger for events that occur in oceanic versus continental crust (at most a factor of 2 difference), Figure 15.11 implies that subset B has larger $\Delta\sigma$ than subset A. In other words, in the latter case, the corresponding

faults are weaker. This result is consistent with studies that have compared intra-plate and inter-plate events (e.g. Kanamori and Anderson, 1975; Scholz et al., 1986), or determined that a continental inter-plate fault such as the San Andreas Fault in California is "weak" (e.g. Zoback and Zoback, 1987).

4.5 References

Bodin, P. and J. N. Brune, On the scaling of slip with rupture length for shallow strike-slip earthquakes: Quasi-static models and dynamic rupture propagation, *Bull. Seismol. Soc. Am.*, **86**, 1292-1299, 1996.

Henry, C. and S. Das, Aftershock zones of large shallow earthquakes: fault dimensions, aftershock area expansion and scaling relations, *Geophys. J. Int.*, **147**, 272-293.

Kanamori, H. and D. L. Anderson, Theoretical basis of some empirical relations in seismology, *Bull. Seism. Soc. Am.*, **65**, 1073-1095, 1975.

Mai, P. and C. Beroza, Source scaling properties from finite fault rupture models, *Bull. Seism. Soc. Am.*, **90**, 605-615, 2000.

Molnar, P. and Q. Denq, Faulting associated with large earthquakes and the average rate of deformation in central and eastern Asia, *J. Geophys. Res.*, **89**, 6203-6227, 1984.

Pegler, G. and S. Das, Analysis of the relationship between seismic moment and fault length for large crustal strike-slip earthquakes between 1977-92, *Geophys. Res. Lett.*, **23**, 905-908, 1996.

Romanowicz, B. Strike-slip earthquakes on quasi-vertical transcurrent faults: inferences for general scaling relations, *Geophys. Res. Lett.*, **19**, 481-484, 1992.

Romanowicz, B.; Ruff, L. J., On moment-length scaling of large strike slip earthquakes and the strength of faults, 10.1029/2001GL014479, 2002.

Romanowicz, B. and J. B. Rundle, On scaling relations for large earthquakes, *Bull. Seism. Soc. Am.*, **83**, 1294-1297, 1993.

Scholz, C. H., C. A. Aviles and S. G. Wesnousky, Scaling differences between large interplate and large intraplate earthquakes, *Bull. Seism. Soc. Am.*, **76**, 65-70, 1986.

Shaw, B. E. and C. H. Scholz, Slip-length scaling in large earthquakes: observations and theory and implications for earthquake physics, *Geophys. Res. Lett.*, **28**, 2995-2998, 2001.

Sornette, D. and A. Sornette, Theoretical implications of a recent non-linear diffusion equation linking short-time deformation to long-time tectonics, *Bull. Seism. Soc. Am.*, **84**, 1679-1983, 1994.

5. Historical Earthquake Re-analysis Project

R. A. Uhrhammer

5.1 Introduction

The objective of this USGS NEHRP funded two-year project, that commenced in March, 2000, is to characterize the spatial and temporal evolution of the San Francisco Bay Region (SFBR) seismicity during the initial part of the earthquake cycle as the region emerges from the stress shadow of the great 1906 San Francisco earthquake. The problem is that the existing BSL seismicity catalog for the SFBR, which spans most of the past century (1910-present), is inherently inhomogeneous because the location and magnitude determination methodologies have changed, as seismic instrumentation and computational capabilities have improved over time. As a result, the SFBR seismicity since 1906 is poorly understood.

Creation of a SFBR catalog of seismicity that is homogeneous, that spans as many years as possible, and that includes formal estimates of the parameters and their uncertainty is a fundamental prerequisite for probabilistic studies of the SFBR seismicity. The existence of the invaluable BSL seismological archive, containing the original seismograms as well as the original reading/analysis sheets, coupled with the recently acquired BSL capability to scan and digitize historical seismograms at high resolution allows the application of modern analytical algorithms towards the problem of determining the source parameters of the historical SFBR earthquakes.

Our approach is to systematically re-analyze the data acquired from the archive to develop a homogeneous SFBR catalog of earthquake location, local magnitude (M_L), moment magnitude (M_w), and seismic moment tensor (mechanism), including formal uncertainties on all parameters which extends as far back in time as the instrumental records allow and which is complete above appropriate threshold magnitudes. We anticipate being able to compile a new SFBR catalog of location and M_L which spans 1927 to the present and is complete at the $M_L \sim 3$ threshold, and of M_w which spans 1911 to the present and which is complete at the $M_w \sim 4.5$ threshold.

In addition to the above analysis, we will also search for sequences of repeating earthquakes. Identification of repeating earthquakes, which are nearly identical in all source properties, provides an internal consistency check on the location and magnitude homogeneity in the catalog over time.

5.2 Background and Motivation

Although the 1910 to present BSL catalog of earthquakes for the SFBR appears to be a simple list of events, one must remember that it really is a very complex

data set. It is easy to misinterpret observed variations in seismicity if we do not understand the limitations of this catalog. The existing 1910 to present BSL catalog of earthquakes for the SFBR is inhomogeneous in that it suffers from the three types of man-made seismicity changes identified by *Habermann*, 1987, namely detection changes, reporting changes, and magnitude shifts. The largest change in the detection capability of the BSL seismic station network occurred circa 1927-1931 with the installation of the Wood-Anderson and Benioff seismometers at four seismic stations (BRK, MHC, PAC, and SFB as shown in Figure 15.12) in the SFBR and the resulting increase in sensitivity lowered the threshold for detection of SFBR earthquakes by about 2 M_L units. The most significant reporting change occurred circa 1942 when the BSL began determining M_L for some earthquakes and by 1948 M_L was routinely determined and reported for all SFBR earthquakes listed in the BSL Bulletin (*Romney and Meeker*, 1949). A magnitude shift occurred in 1954 when the response of the Wood-Anderson seismographs changed (owing to changing the free period from 1.0 to 0.8 seconds) (*Bolt and Miller*, 1975).

The lack of a homogeneous catalog of earthquake for the SFBR which spans most of the past century, the availability of the invaluable BSL seismological archive, the interest in the Working Group on California Earthquake Probabilities (WGCEP, 1999), the funding of an initial effort with support from the USGS-PG&E CRADA, and the purchase and loan of a high-resolution wide-format digitizer by the USGS, combine to provide both an incentive and a unique opportunity to systematically re-process, using modern algorithms, the BSL seismographic records and data for SFBR earthquakes and to produce a homogeneous catalog of earthquakes for the region.

5.3 Initial Effort

During the summer of 1998, the USGS funded two students, via a USGS-PG&E CRADA, to transcribe the data from the original BSL reading/analysis sheets to computer readable form. With this funding, they were able to transcribe the reading/analysis sheets for SFBR earthquakes, working back in time from 1983 through 1944 (1984 onward was already in a computer database). The newly transcribed data along with the data already in the database were used to determine systematically the location, M_L , and corresponding uncertainties of earthquakes which have occurred in the SFBR. An interim catalog of SFBR earthquakes was subsequently developed

which includes hypocenter, M_L , and their uncertainties, and which spans from 1951 through 1998. The catalog starts in 1951 because amplitude data, used in the determination of M_L , were not registered on the reading/analysis sheets prior to that time. The interim catalog events are plotted in Figure 15.12 and available at <http://www.seismo.berkeley.edu/seismo/herp/>.

The rate of SFBR seismicity (see Figure 15.13) inferred from the 1951-1998 Interim Catalog is: $\log N = 4.105 - 0.890 M_L$. Assuming that the annual rate of SFBR seismicity ($M_L \geq 3$) is stationary, we expect to observe an average of 27 earthquakes per year.

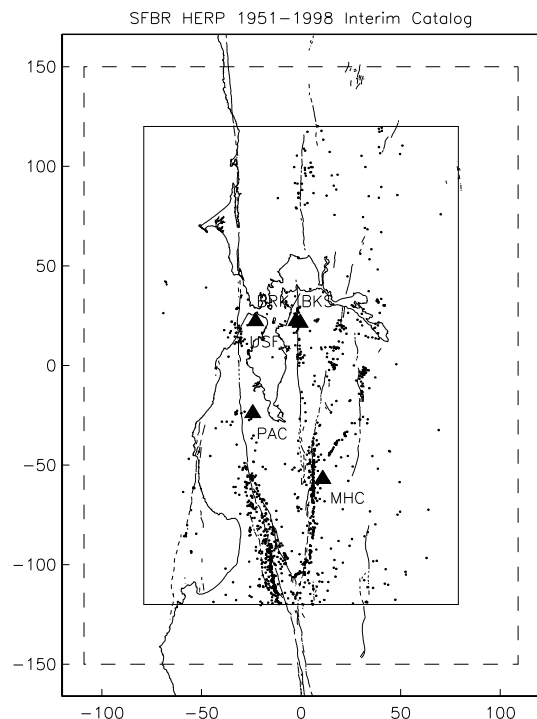


Figure 15.12: Map of the San Francisco Bay Region showing the Interim 1951-1998 Seismicity and the Stations which have housed Wood-Anderson seismographs. The solid inner box defines the SFBR (as given in the WGCEP 99 Report) and the dashed box is a 30 km buffer zone in which candidate SFBR events are also analyzed.

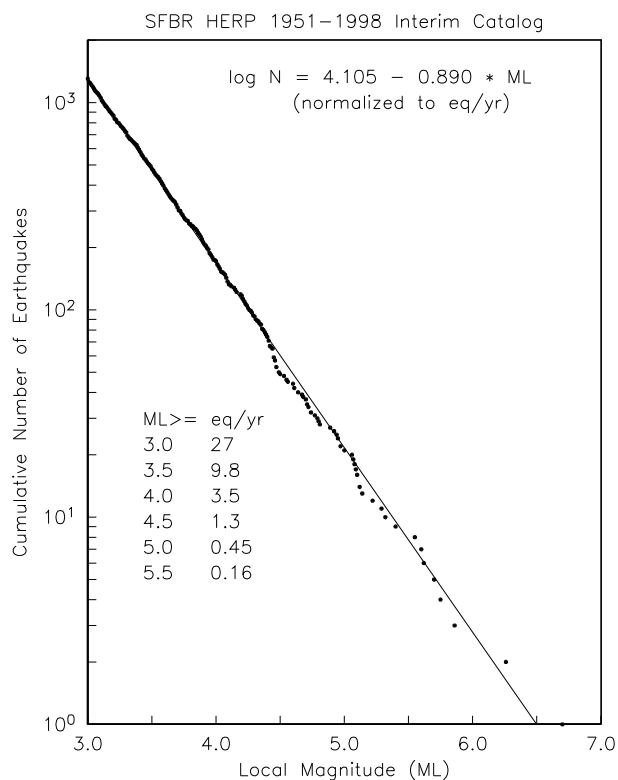


Figure 15.13: SFBR rate of seismicity inferred from the 1951-1998 catalog.

5.4 Progress During the First Year

Since the Wood-Anderson maximum trace amplitude data used in the determination of M_L were not registered on the original reading/analysis sheets kept in the BSL archive, we read the maximum trace amplitudes recorded by the Wood-Anderson seismographs in order to calculate M_L and its uncertainty. The manpower intensive task of reading the maximum trace amplitudes registered by the Wood-Anderson seismographs for Berkeley (BRK), Mt. Hamilton (Lick Observatory; MHC), Palo Alto (Banner Station; PAC), and San Francisco (USF) that are kept on store in the BSL seismogram archive in Edwards Sta-

dium was completed by June 2001. We began with the 1950 records and worked backward in time and finished reading the earliest Wood-Anderson records (circa 1927) in June 2001.

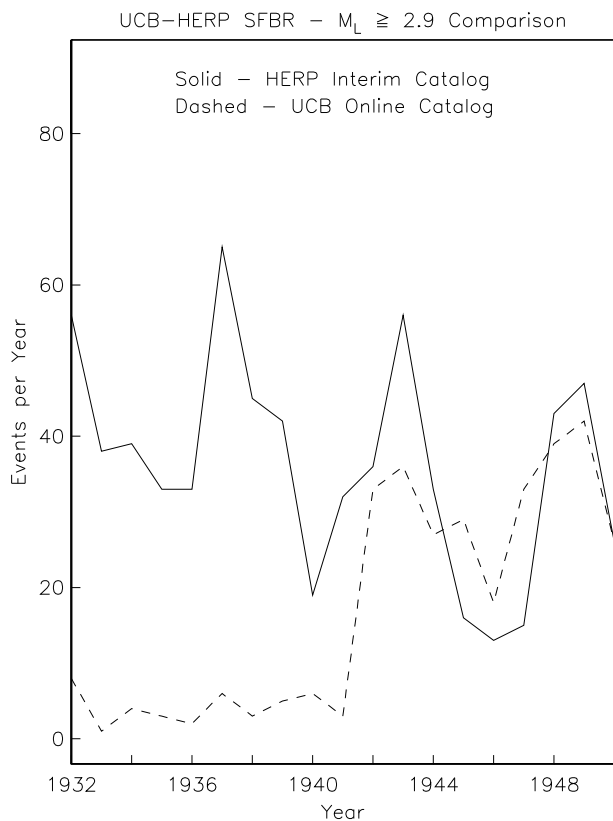


Figure 15.14: Number of 1932-1951 SFBR events analyzed (solid line) compared to the number of events listed in the BSL on-line catalog. Note that prior to 1942, the BSL on-line catalog does not list a large number of the events occurring in the SFBR owing to the fact that, since they had only a descriptive location rather than geographical coordinate location listed in the Bulletin, they were not transcribed when the computer readable database was initially compiled in the mid-1960's.

A list of candidate SFBR events, which included all events in the UCB catalog of earthquakes and also all events in the BSL Bulletins that were within the SFBR (including the 30 km buffer zone) and which either had a M_L of 2.8 or larger or else no M_L assigned, was compiled. The UCB catalog for the pre-1951 era is a composite based on the analysis of instrumental recordings and felt reports (*Bolt and Miller, 1975*). As we progressed back in time prior to 1951, the proportion of events with no M_L assigned increases and prior to 1942 it is virtually 100 percent. The number of 1932-1951 events analyzed is shown in Figure 15.14. To expedite the processing, we read the microfilm copies of the MHC Wood-Anderson

seismograms (*Uhrhammer, 1983*) to cull out events which are below the M_L 2.8 threshold and thus minimized the number of records that we had to deal with in the BSL seismogram archive.

Originally, we did all the seismogram reading in the seismogram archive in Edwards Track Stadium and the students spent a significant amount of time shuttling between the BSL facilities in McCone Hall and Edwards Track Stadium. To expedite the processing, we transferred the seismogram bundles for the years that were being read to McCone Hall and this proved to be much more efficient.

5.5 Progress During the Past Year

We discovered a significant number of instances where the phases and maximum trace amplitudes were easily readable on the Wood-Anderson seismograms but there were no corresponding phase entries on the original reading/analysis sheets. Consequently we had to read the phase onset times for a numerous events that occurred prior to 1951. This process was quite tedious and time consuming owing primarily to the necessity of determining the clock corrections that convert the time on the record to Universal Time (UT). Clock corrections relative to a radio time standard were tabulated daily and linearly interpolated to determine the clock correction for a given event. The time corrections were occasionally unreliable (particularly so at USF) so we had to use relative times (the time difference between the P-wave and S-wave onsets) in place of absolute times when using the data to locate an event. The photographic paper was occasionally placed on the recording drums emulsion side down which resulted in faint and unreadable traces. Seismograms were occasionally fogged (inadvertently exposed to light) which also rendered them generally unreadable. Some seismograms are also difficult or impossible to read owing to the trace being out of focus due to misaligned optics.

We have finished transcribing the 1910-1927 data (pre-Wood-Anderson instrument) data. Prior to the advent of the Wood-Anderson seismographs, there were only two seismic stations operating in the Berkeley network, namely at the Student Observatory on the Berkeley Campus (BRK) and at the Lick Observatory at Mt. Hamilton (MHC). It should be noted that the earliest stations were operated at astronomical observatories primarily because these observatories had the means to routinely determine accurate clock corrections required for interpretation of data recorded on the seismograms. During the pre-1927 era, the primary seismic instrumentation at BKS and MHC consisted of Bosch-Omori and Wiechert seismographs which operated at low magnification (100x) and recorded on smoked paper.

We are also scanning and digitizing selected pre-1934 events recorded by Weichert and Bosch-Omori seismo-

graphs and the corresponding Wood-Anderson seismograms for those cases where the event was also recorded by Wood-Anderson seismographs. The primary objectives are to calibrate the determination of magnitude from the pre-Wood-Anderson recorded events and to begin the process of acquiring digital representations of the pre-1932 smoked paper seismograms. Obtaining digital representations of the Bosch-Omori and Weichert smoked paper seismograms is crucial particularly because the earliest smoked paper records, kept on store in the Berkeley Seismogram Archive, are becoming quite brittle and difficult to handle. We have been scanning these seismograms mostly on a flat bed scanner because some of the records could be damaged if they are passed through the rollers in the large format scanner.

5.6 Fuzzy-Logic-Based Location Algorithm

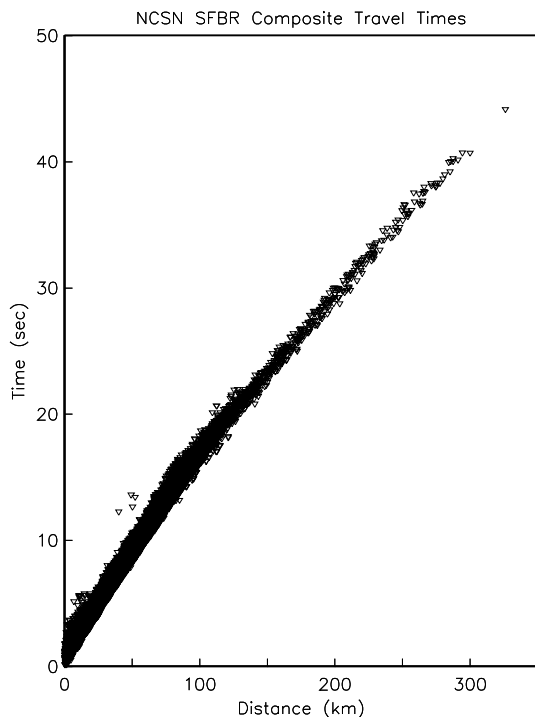


Figure 15.15: Observed travel times from SFBR earthquakes to NCSN SFBR stations. Plotted are travel time data from 1984-2000 for which the original waveforms are available on the NCEDC.

The end goal of HERP is to develop a uniform and internally consistent catalog of SFBR seismicity for instrumentally recorded earthquakes which have occurred during the past century in the region. As a part of this goal, we need to develop and calibrate a procedure for obtaining robust earthquake locations throughout a time when the number of SFBR seismic stations

evolved from the initial two stations (BRK and MHC) at the turn of the last century to the more than 100 seismic stations at present. The complex geology and faulting observed in the SFBR results in seismic wave propagation times which scatter significantly over differing propagation paths in the region as shown in Figure 15.15. Initially, the events are being located using a one-dimensional velocity model with appropriate station adjustments. Ultimately, however, a three-dimensional velocity model will be preferable for locating SFBR earthquakes.

We found that the existing earthquake location algorithms do not provide robust solutions when using the potentially imprecise data available from the sparse four-station pre-1960 SFBR seismic network. The distribution of observed P-wave travel times for the SFBR is shown in Figure 15.15. Consequently, a fuzzy logic based algorithm was developed to facilitate the determination of robust earthquake locations (Uhrhammer, 2001). The algorithm inherently has a high tolerance for imprecision in the observed data and it can yield robust sparse network solutions without requiring that the problematic observed data be either identified, down-weighted, or removed. This characteristic also renders the algorithm ideally suited for use in automated systems, such as the REDI Project, which provide rapid earthquake information.

5.7 Acknowledgements

We thank William Bakun of the USGS who encouraged us to pursue this project. UC Berkeley students Tom Fournier, Karin Spiller, Gabe Trevis, and Sierra Boyd participated in this project and we thank them for their efforts.

This project was supported by the USGS, through the NEHRP External Grants Program.

5.8 References

- Bolt, B. A. and R. D. Miller, Catalog of Earthquakes in Northern California and Adjoining Areas: 1 January 1910 - 31 December 1972, *Seismographic Stations, University of California, Berkeley*, iv + 567 pp., 1975.
- Habermann, R. E., Man-made changes of seismicity rates, *Bull. Seism. Soc. Am.*, 77, 141-159, 1987.
- Romney, C. F. and J. E. Meeker, Bulletin of the Seismographic Stations, *University of California Press*, 18, pp. 89, 1949.
- Uhrhammer, R. A., Microfilming of historical seismograms from the Mount Hamilton (Lick) seismographic station. *Bull. Seismo. Soc. Am.*, 73, 1197-1202, 1983.
- Uhrhammer, R. A., The San Francisco Bay Region Historical Earthquake Re-analysis Project: A progress report and locating pre-1960 instrumentally recorded earthquakes using a fuzzy-logic-based algorithm, *Seism. Res. Lett.*, 72, 245, 2001.

6. Northern California Seismicity Project

R. A. Uhrhammer

6.1 Introduction

The Northern California Seismicity Project (NCSP) is a counterpart to the San Francisco Bay Region (SFBR) - Historical Earthquake Re-analysis Project (HERP) reported in the research chapter on HERP. The initial objective of this project which commenced in August, 2000, is to transcribe the pre-1984 data for $M_L \geq 2.8$ earthquakes which have occurred in Northern and Central California (NCC) (outside of the SFBR covered by HERP), from the original reading/analysis sheets, kept on store in the Berkeley Seismological Archives, to a computer readable format.

As is the case with HERP, characterization of the spatial and temporal evolution of NCSP seismicity during the initial part of the earthquake cycle as the region emerges from the stress shadow of the great 1906 San Francisco earthquake is the long term goal. The problem is that the existing BSL seismicity catalog for the SFBR, which spans most of the past century (1910-present), is inherently inhomogeneous because the location and magnitude determination methodologies have changed, as seismic instrumentation and computational capabilities have improved over time. As a result, NCC seismicity since 1906 is poorly understood.

Creation of a NCC seismicity catalog that is homogeneous, that spans as many years as possible, and that includes formal estimates of the parameters and their uncertainty is a fundamental prerequisite for probabilistic studies of the NCC seismicity. The existence of the invaluable BSL seismological archive, containing the original seismograms as well as the original reading/analysis sheets, coupled with the recently acquired BSL capability to scan and digitize historical seismograms at high resolution allows the application of modern analytical algorithms towards the problem of determining the source parameters of the historical SFBR earthquakes.

6.2 Background and Motivation

Although the 1910 to present BSL catalog of earthquakes for NCC appears to be a simple list of events, one must remember that it really is a very complex data set. It is easy to misinterpret observed variations in seismicity if we do not understand the limitations of this catalog. The existing 1910 to present BSL catalog of earthquakes for NCC is inhomogeneous in that it suffers from the three types of man-made seismicity changes identified by *Habermann, 1987*, namely detection changes, reporting changes, and magnitude shifts. The largest change in the detection capability of the BSL seismic station net-

work occurred starting circa 1927 with the installation of the Wood-Anderson and Benioff seismometers at several sites in NCC (see Figure 15.16) and the resulting increase in sensitivity lowered the threshold for detection of NCC earthquakes by about 2 M_L units. The most significant reporting change occurred circa 1942 when the BSL began determining M_L for some earthquakes and by 1948 M_L was routinely determined and reported for all SFBR earthquakes listed in the BSL Bulletin (*Romney and Meeker, 1949*). A magnitude shift occurred in 1954 when the response of the Wood-Anderson seismographs changed (owing to changing the free period from 1.0 to 0.8 seconds) (*Bolt and Miller, 1975*).

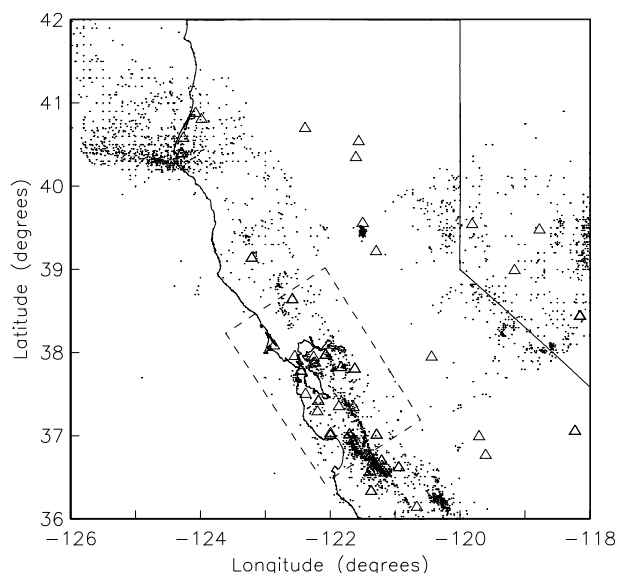


Figure 15.16: Map of the NCC Region showing the 1951-1983 $M_L \geq 2.9$ seismicity (small dots). The triangles are the seismic stations, operated by Berkeley and adjacent networks between 1951 and 1983, for which data are available. Events occurring in the dashed inset box are being transcribed and analyzed via HERP (see the HERP research chapter).

The lack of a homogeneous catalog of earthquake for the SFBR which spans most of the past century, the availability of the invaluable BSL seismological archive, the interest in the Working Group on California Earthquake Probabilities (WGCEP, 1999), the funding of an initial effort with support from the USGS-PG&E CRADA, and the purchase and loan of a high-resolution wide-format digitizer by the USGS, combine to provide both

an incentive and an unique opportunity to systematically re-process, using modern algorithms, the BSL seismographic records and data for SFBR earthquakes and to produce a homogeneous catalog of earthquakes for the region.

```

NEIS 1977/01/09 23:24:39 39.50N 121.64W 2 14 Northern
California
NEIS M~L3.3(BRK), AFTER BRK.
NEIS IO=V MM AT DOBBINS. ALSO FELT AT GRIDLEY, GOLD RUN, RACKERBY,
MARYSVILLE, BROWNSVILLE AND OROVILLE.
BRK 1977/01/09 23:24:39 39.50N 121.64W 2 3.4L Northern
California
ISC *1977/01/09 23:24:37 39.55N 121.53W 2 15 Northern
California
ORV 0.02 84 -iP Pn 23:24:42.00 -2.6
KPK 0.17 80 iP/PN Pn 23:24:44.10 -2.7
MIN 0.79 356 +iP/PKP Pn 23:24:56.00 0.4
WDC 1.29 323 +iP/PKP Pn 23:25:02.60 -0.1
WCN 1.39 99 iP/PN Pn 23:25:05.10 0.9
BKS 1.76 198 +iP/PKP Pn 23:25:09.00 -0.5
BKS S/(SKS) 23:25:30.00 -2.9
JAS 1.82 152 +iP/PKP Pn 23:25:10.20 -0.1
ARN 2.20 181 ePN Pn 23:25:15.60 -0.2
MHC 2.21 183 iP/PKP Pn 23:25:16.00 0.1
SAO 2.78 178 P/PKP Pn 23:25:24.00 -0.1
MNV 2.86 112 eP/PKP Pn 23:25:26.00 0.9
FRI 2.93 150 +iP/PKP Pn 23:25:26.90 0.7
BMN 3.42 74 ePN Pn 23:25:34.30 1.1
TNP 3.67 112 ePN Pn 23:25:37.40 0.7
EUR 4.30 89 iP Pn 23:25:46.00 0.4 Al.56E01 T 0.4
EUR i 23:26:53.80

```

Figure 15.17: Example of printer file of data for Berkeley network data extracted from ISC CDROM.

6.3 Current Effort

To expedite the transcription process, we converted all relevant available data from the online NCEDC event catalogs and the in-house phase data to the flat transcription file format as shown in Figure 15.17 for the years 1978 through 1983. We also acquired a copy of the International Data Center (ISC) CDROM which contains events and associated station data published in the ISC Bulletins from January 1964 through December 1977 (Version 1.2). This ISC data set includes event and station data contributed by Berkeley and the CDROM also contains a algorithm to search the database and extract and translate the ISC coded phase Berkeley data to a readable print format for years 1963 through 1977. This enabled us to start with transcription files that contained approximately half of the data that is on the original reading/analysis sheets for the years 1964 through 1983. The primary data from the original reading/analysis sheets, that was not included in this process, was the Wood-Anderson maximum trace amplitude data that is crucial for the determination of local magnitude.

During the past year five students worked on the process of transcribing the data from the original BSL reading/analysis sheets to computer readable form. They started by transcribing the original reading/analysis sheets from 1983 and they have been working back in time. The data from 1964 through 1983 has now been transcribed.

We are currently transcribing reading/analysis sheet

data from 1963. Since none of the data on the pre-1964 reading/analysis sheets exists in a computer readable form, all data has to be transcribed and consequently it takes more time to transcribe each event.

```

E 010977 232439.5 39-30.1 121-38.6 2.0 3.4
C 5KM SOUTHWEST OF OROVILLE, CALIFORNIA
F MMI V at Oroville
F Also felt at Gridley, Gold Run, Rackerby, Marysville and
F Brownsville
P BKS Ben Z e P c 232509.0
P BKS Ben E e S - 232529.5
A BKS WA - 0.65 0.7
P MIN Ben Z i P c 232456.0
A MIN WA - 5.2 6.0
P PCC Ben Z e (P) - 232515
A PCC Ben 11 - -
P MNV Ben Z e P - 232526.-
P PRI Ben Z e - - 232538
P ORV Ben Z i P d 232442.0
P JAS Ben Z e P c 232510.2
P WDC Ben Z i P c 232502.6
A BRK Ben Z e (P) - 232510
A BRK Ben 6 - -
P SAO Ben Z e (P) - 232524.2
P FRI Ben Z e P c 232526.9
P MHC Ben Z e P (c) 232516.0
A MHC WA - 0.35 0.25
P GCC Ben Z e - - 232520
P PRS Ben Z e (P) - 232530.8
P LLA Ben Z e - - 232527
A LLA Ben 19 - -
P FHC Ben Z e - - 232518
X

```

Figure 15.18: Example of completed transcription file format for the event shown in Figure 15.17.

6.4 Acknowledgements

UC Berkeley students Tom Fournier, Karin Spiller, Gabe Trevis, Maxwell Wilmarth, and Jennifer Epstein participated in this project and we thank them for their efforts.

This project was partially supported by the USGS funding of the Northern California Earthquake Data Center.

6.5 References

Bolt, B. A. and R. D. Miller, Catalog of Earthquakes in Northern California and Adjoining Areas: 1 January 1910 - 31 December 1972, *Seismographic Stations, University of California, Berkeley*, iv + 567 pp., 1975.

Habermann, R. E., Man-made changes of seismicity rates, *Bull. Seism. Soc. Am.*, 77, 141-159, 1987.

Romney, C. F. and J. E. Meeker, Bulletin of the Seismographic Stations, *University of California Press*, 18, pp. 89, 1949.

7. Accelerated Stress Buildup on the Southern San Andreas Fault and Surrounding Regions Caused by Mojave Desert Earthquakes

Andrew M. Freed and Jian Lin (Woods Hole Oceanographic Institution)

7.1 Summary

Scientists have hypothesized for decades that one major earthquake can trigger another earthquake on a nearby fault through stress interaction. More recent studies have further suggested that this interaction may be delayed by the slow viscous creeping of rocks in the Earth's lower crust and upper mantle. This is best illustrated by the 1999 magnitude 7.1 Hector Mine earthquake, which occurred only 30 km away from the 1992 magnitude 7.3 Landers quake, but seven and half years later. The delay between these events can be explained by viscous flow consistent with observations of continuous ground deformation following the Landers quake (Freed and Lin, 2001). In our more recent study (Freed and Lin, 2002), we further calculated how the Landers, Hector Mine, and two other earthquakes in the Mojave Desert have changed stresses on the nearby southern San Andreas and adjacent fault systems. We calculated that these earthquakes and continuous viscous creeping at depth are causing a rapid increase of stresses on a section of the San Andreas Fault, called the San Bernardino Mountain segment, that is located only 80 km from Los Angeles (Figure 15.19). The San Bernardino Mountain segment is worthy of special attention because it is capable of producing major earthquakes with magnitude greater than 7. Since the last major earthquake on this segment was over 190 years ago, the fault may be late in its earthquake cycle, and thus the calculated ongoing stress increase on the fault is of added significance. In addition, we calculated that parts of the San Jacinto, Elsinore, and Calico faults are also experiencing accelerated stress buildup. In particular, the Calico fault, which lies just north of the Landers rupture (near Barstow), appears to have the calculated stress patterns and the observed post- Landers aftershock clustering quite similar to the Hector Mine region before the 1999 quake. This makes the Calico fault another candidate for a potential earthquake in the future, where seismic activity should be watched closely.

7.2 References

Freed, A.M., and J. Lin, Delayed triggering of the 1999 Hector Mine earthquake by viscoelastic stress transfer, *Nature*, 411, 180-183, 2001.

Freed, A.M., and J. Lin, Accelerated stress buildup on the southern San Andreas fault and surrounding regions caused by Mojave Desert earthquakes, *Geology*, 30, 571-574, 2002.

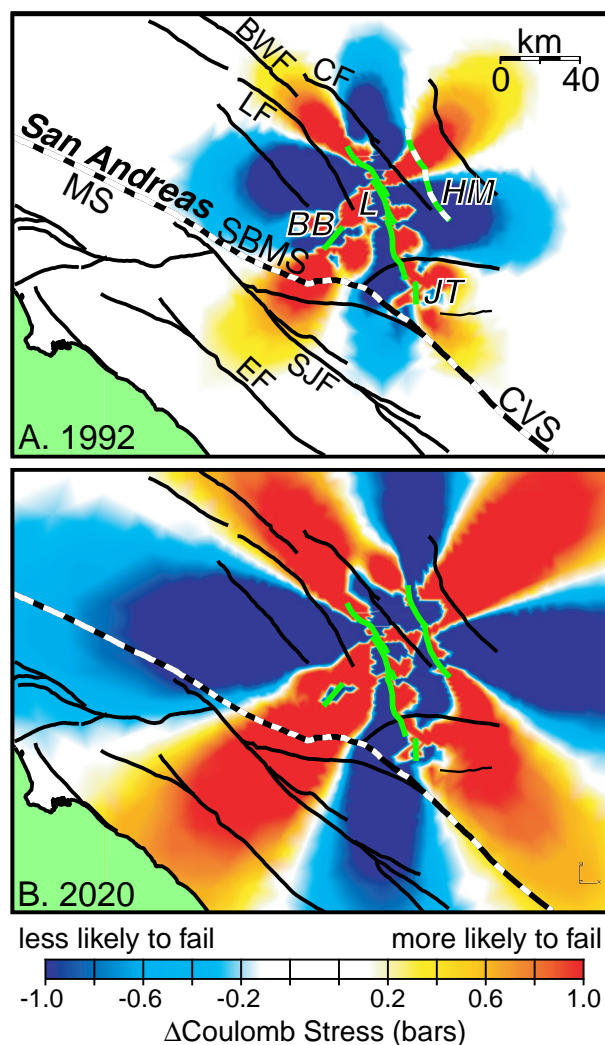


Figure 15.19: A. Calculated coseismic Coulomb stress changes caused by fault slip associated with the 1992 Joshua Tree (JT), Landers (L), and Big Bear (BB) earthquakes (green lines). Other faults: MS - Mojave segment, SBMS - San Bernardino Mountain segment, and CVS - Coachella Valley segment of San Andreas fault; SJF - San Jacinto fault, EF - Elsinore fault, CF - Calico fault, LF - Lenwood, and BWF - Blackwater fault. Location of future 1999 Hector Mine (HM) earthquake (green dashed line) is also shown. B. Same as A but with addition of stresses associated with 1999 Hector Mine earthquake and postseismic relaxation to the year 2020.

8. Land Uplift and Subsidence in the Santa Clara Valley

David Schmidt and Roland Bürgmann

8.1 Introduction

The Santa Clara Valley is a sedimentary basin whose stratigraphy forms a series of interbedded aquifers and aquitards (Clark, 1924). Land uplift and subsidence in the valley due to the recharge and withdrawal of fluids is well documented by several public agencies such as the Santa Clara Valley Water District (SCVWD) and the USGS (see Poland and Ireland, 1988). An increase in the withdrawal of water from the aquifer and a decrease in rainfall for the first half of the twentieth century resulted in a substantial drop in well levels and a corresponding land subsidence of ~ 4 m. Recovery efforts over the past quarter century, such as the import of water from outside sources and the construction of percolation ponds, have allowed water levels to partially recover. Preservation of the aquifer requires the continual monitoring through extensometers, well water levels, and level line observations.

InSAR is an attractive method for monitoring land subsidence because of its spatial coverage and precision (e.g., Galloway et al., 1998; Hoffmann et al., 2001). However, individual interferograms are often difficult to interpret because the amount of deformation that is observed is highly dependent on the time of the season that the first and second SAR scenes are acquired. A time-series analysis has the potential to overcome this limitation by resolving the temporal variability of the surface deformation. We perform an InSAR time-series analysis using 115 interferograms spanning the time period from April of 1992 to June of 2000. The time-series analysis inverts for the incremental range-change between SAR scene acquisitions, producing a time-dependent signal of land uplift and subsidence.

8.2 Time-Series Result

The InSAR time series reveals an overall pattern of uplift since 1992 (Figure 15.20). The uplift is attributed to an increase in the ground water levels. The increase in pore pressure reduces the vertical effective stress on the skeletal matrix resulting in regional uplift. We observe as much as 41 ± 18 mm of uplift centered north of Sunnyvale. Most of this uplift took place between 1992 and 1998 with a mean uplift rate of 6.4 ± 2.2 mm/yr. Uplift is also observed in the Evergreen Basin located in the eastern portion of the Santa Clara valley. Significant subsidence relative to Oak Hill is also observed along the western margin of the valley. The southwestern portion of the valley shows insignificant uplift with no distinctive pattern. Continual uplift extends along several ma-

ior tributaries, especially along Garabazas and Saratoga creeks.

The time series also resolves a seasonal uplift pattern with the largest magnitude centered near San Jose (Figure 15.20b). The seasonal signal is sharply bounded on the east by a structure that aligns with the northward extension of the Silver Creek fault. Both ascending and descending interferograms show consistent deformation across this fault suggesting that the relative motion is vertical and not related to strike-slip fault motion. The fault appears as a sharp discontinuity in the deformation field of several interferograms that can be explained by differential subsidence across the structure. A seasonal subsidence pattern is also observed in the northwest portion of the region, however this signal is more complex and difficult to characterize.

8.3 Interpretation of Subsidence Pattern

The InSAR time-series results suggest that the aquifer can be further subdivided into three domains based on the deformation pattern: two regions experiencing net uplift (1992-2000) centered in Sunnyvale and the Evergreen basin, and a central region dominated by seasonal deformation. The seasonal uplift is bounded on the west where the thickness of unconsolidated sediments decreases along the northwesterly-striking basement high extending from Edenvale Ridge and Oak Hill.

The magnitude of elastic rebound is expected to correlate with the thickness of unconsolidated alluvium, or the depth to basement assuming that a change in pore pressure is translated to the full thickness. Unfortunately, the depth to basement is unconstrained for much of the valley; few of the wells reach consolidated bedrock. At several localities, such as in San Jose and north of Sunnyvale, the depth to basement is believed to be in excess of 420 m (Meade, 1967; California Department of Water Resources (CDWR), 1967). Well data suggests that the depth to basement is highly variable throughout the San Francisco Bay region where faulting and erosion during periods of low sea level have created an irregular bedrock surface.

The thickness of the alluvium is not the only property of the aquifer that may control the elastic response. The heterogeneity of sediment type and the connectivity of permeable beds may also play a significant role. The effective time constants of flow depend on the thickness of interbeds and the vertical hydraulic diffusivity of aquitards. The petrology and grain size of sediments from well cores were cataloged in an effort to character-

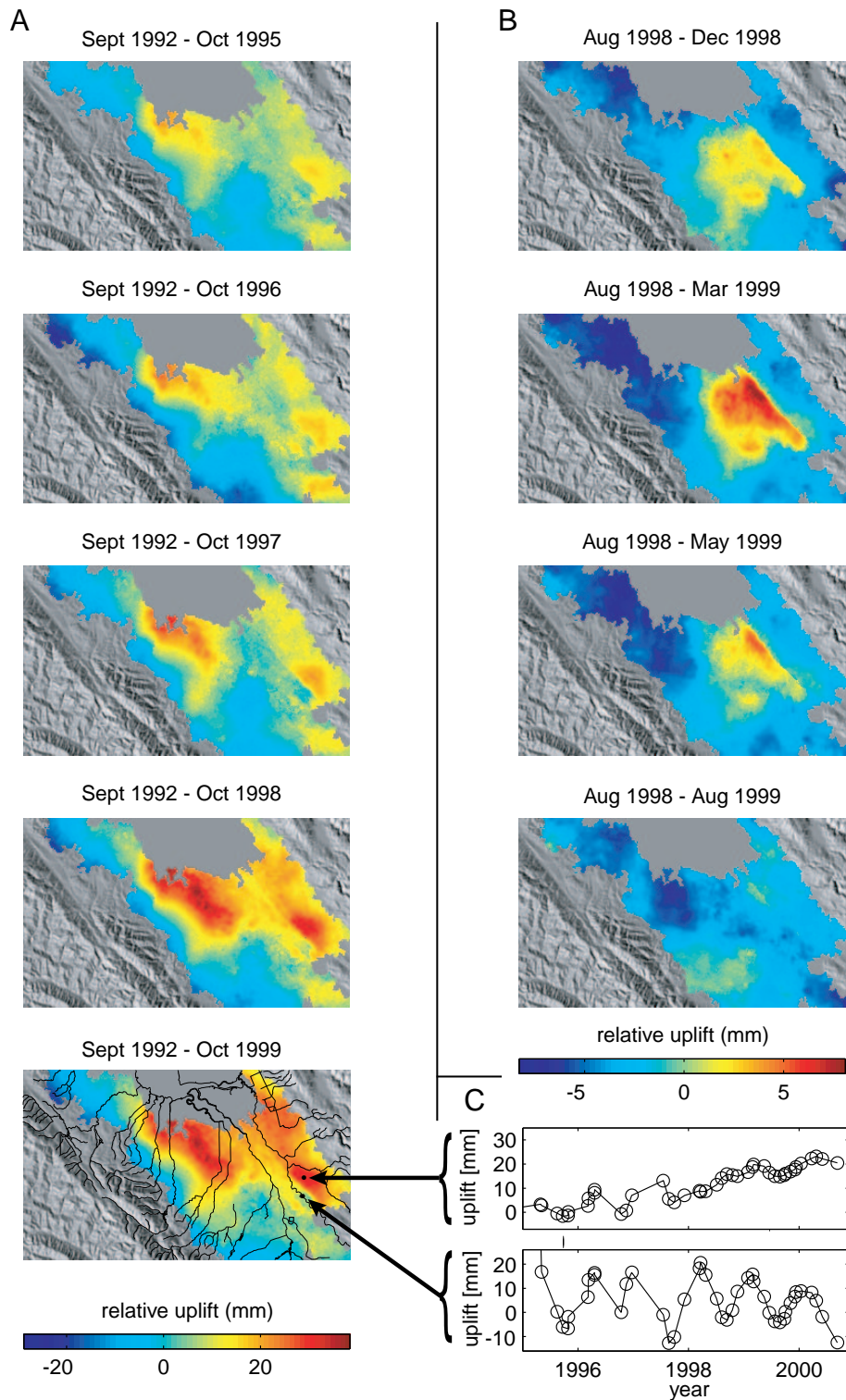


Figure 15.20: (A) Five frames from the InSAR time series show the pattern of net uplift since September of 1992. Uplift is centered north of Sunnyvale and east of the Silver Creek fault in the Evergreen Basin. Uplift is relative to Oak Hill (open square in final frame). The drainage network for the Santa Clara valley is also shown in the final frame. (B) The seasonal uplift pattern during a period from August of 1998 through August of 1999. (C) Time series at two points (dots in final frame of A) are compared to illustrate the seasonal versus long term deformation pattern. The points are separated by the Silver Creek fault which partitions the aquifer.

ize the constituents of the aquifer system. Meade (1967) and Johnson *et al.* (1968) analyzed core samples from the Sunnyvale and San Jose extensometer sites. Fine sands and clays dominate the sediment found at the Sunnyvale site with grain sizes ranging from 0.001 to 0.2 mm. In San Jose, grain sizes were generally larger ranging from 0.004 to 1.5 mm with often abrupt transitions between fine and coarse deposits. Developing geologic cross sections from well logs can be difficult because stratigraphic units may not correlate, especially if the units have an appreciable dip. Johnson (1995) used statistical correlations between well-perforation indicators to determine the lateral extent of water-bearing units. Coarse-grained units were found to be correlated over a wider area near San Jose than in Sunnyvale with an average bed thickness of 2.5 versus 1.3 m, respectively.

Despite the difficulty in correlating units from one well to the next, well log data and hydraulic head levels at different depths identified a sequence of productive water-bearing units identified as the Agnew aquifer (CDWR, 1967; Johnson, 1995). The deposition of these units is associated with the ancestral drainage of the Coyote creek and the Guadalupe river, both of which transport sediment down the valley axis on the way to the bay (Meade, 1967; CDWR, 1967). Seasonal uplift and subsidence shown in Figure 15.20b outlines a tabular region that broadens towards the north and may reflect the seasonal recharge of the Agnew aquifer. The InSAR data is not sufficient to resolve whether recharge has occurred in the shallow or deep sequence of the Agnew aquifer. The southern end of the seasonal uplift signal is co-located with the southernmost limit of the confined zone. Recharge of the basin is accommodated through the flow of subsurface water from the Coyote valley located to the south of the Santa Clara valley. Subsurface water flows through a narrow alluvial channel between Oak Hill and the Edenvale Ridge before cascading into the deeper aquifer (CDWR, 1967).

The long term uplift pattern also suggests that the permeable beds extend along stream channels to the west; however, these regions do not exhibit much seasonal deformation. The subsidence along the west side of the valley observed in Figure 4a outlines the Santa Clara formation which is traditionally characterized as the recharge zone. The coarser sediment found in the San Jose well log implies higher hydraulic conductivities. The large seasonal uplift pattern in San Jose may be explained by a system where the seasonal influx of groundwater is redistributed over short periods of time. In contrast, the aquifer north of Sunnyvale and in the Evergreen basin may be characterized by lower hydraulic conductivities because of a greater percentage of fine sediment and clay layers resulting in the slow influx of groundwater into these parts of the aquifer.

The uplift pattern observed using the InSAR time se-

ries highlights the spatial complexity of the aquifer system in the Santa Clara valley. The temporal and spatial pattern of uplift and subsidence afforded by InSAR provides important constraints on the lateral distribution of water bearing units and the time scales over which the groundwater is exchanged. Ultimately, knowing the lateral extent and connectivity of water bearing units will improve numerical studies which attempt to model the mechanics of the aquifer system.

8.4 Acknowledgements

SAR data was provided to the WInSAR Consortium by the European Space Agency (ESA) through their North American distributor, Eurimage. Original SAR data ©ESA (1992-2000). Additional data provided by an ESA (ENVISAT) data grant.

8.5 References

- California Department of Water Resources, Evaluation of groundwater resources, South San Francisco Bay, appendix A: Geology, Bulletin 118-1, 153 pp., 1967.
- Clark, W. O., Ground water in Santa Clara valley, California, *U. S. Geol. Surv. Water-Supply Pap.*, 519, 209 pp., 1924.
- Galloway, D.L., Hudnut, K.W., Ingebritsen, S.E., Phillips, S.P., Peltzer, G., Rogez, F., and P. A. Rosen, Detection of aquifer system compaction and land subsidence using interferometric synthetic aperture radar, Antelope valley, Mojave Desert, California, *Water Resour. Res.*, 34, 2573-2585, 1998.
- Hoffmann, J., Zebker, H., Galloway, D., and F. Amelung, Seasonal subsidence and rebound in Las Vegas valley, Nevada, observed by synthetic aperture radar interferometry, *Water Resour. Res.*, 37, 1551-1566, 2001.
- Johnson, A. I., Moston, R. P., and D. A. Morris, Physical and hydrologic properties of water-bearing deposits in subsiding area in central California, *U. S. Geol. Surv. Prof. Pap.*, 497-A, 71 pp., 1968.
- Johnson, N. M., Deterministic and stochastic approaches for evaluating multiple scales of Santa Clara valley hydrostratigraphy, in Sangines, E. S., Anderson, D. A., and A. V. Busing, Recent Geologic Studies in the San Francisco Bay Area, Pacific Section of the Society of Economic Paleontologists and Mineralogists, 76, 193-208, 1995.
- Meade, R. H., Petrology of sediments underlying areas of land subsidence in central California, *U. S. Geol. Surv. Prof. Pap.*, 497-C, 83 pp., 1967.
- Poland, J. F., and R. L. Ireland, Land Subsidence in the Santa Clara valley, California, as of 1982, *Mechanics of Aquifer Systems, U. S. Geol. Surv. Prof. Pap.*, 497-F, 61 pp., 1988.

9. Application of Point Measurements from InSAR to Study Slow Earthquakes on the Central San Andreas Fault

Ingrid A. Johanson and Roland Bürgmann

9.1 Introduction

In 1992, 1996 and 1998, creepmeters and strainmeters on the San Andreas fault (SAF) near San Juan Bautista recorded slip transients identified as slow earthquakes (SEQs) (Linde *et al.*, 1996; Gwyther *et al.*, 2000). These authors determined that SEQs in this area had moment magnitudes equivalent to the largest seismic quakes (M_w 4.8-5.1) in this region. Their size and frequency suggest that SEQs are an important contributor to strain release. Additionally, SEQs primarily occur in areas of transition between locked and stably sliding faults, and may offer clues as to why and how these transitions take place. However, the low density of creep- and strainmeters makes it difficult to determine basic rupture parameters, such as the area or depth of the slip patch, with much certainty. In fact, the instrument density is so low that the network may fail to record many slow earthquakes. We are using high resolution geodetic measurements adjacent to the fault in an attempt to significantly improve our observations of SEQs and to possibly identify unrecorded SEQs. In particular, we would like to know: how common slow earthquakes are, how much of the fault's total slip they accommodate, whether they consistently rupture the same fault patch and how their occurrence depends on depth. Ultimately, our results should give us a better understanding of how episodic, aseismic slip events fit into the overall mechanics of fault systems.

9.2 InSAR

The extensive spatial coverage, good resolution and sub-centimeter precision of Interferometric Synthetic Aperture Radar (InSAR) makes it an ideal tool for measuring surface deformation due to slow earthquakes. However, the ground cover for this section of the SAF is largely vegetation and many interferograms are reduced to random scatter as a result of decorrelation noise (Figure 15.22). We must remove any decorrelation noise before we can identify a geophysically based signal. Our observations of InSAR amplitudes and air photos reveal that small buildings and rock outcrops exist within the vegetated areas that could provide stable and accurate measurements (Figure 15.21). These isolated stable patches ('stable scatterers'), ranging in size from a small town to a single pixel, can be extracted from the sea of decorrelation noise and pieced together to increase the useful area of an interferogram.

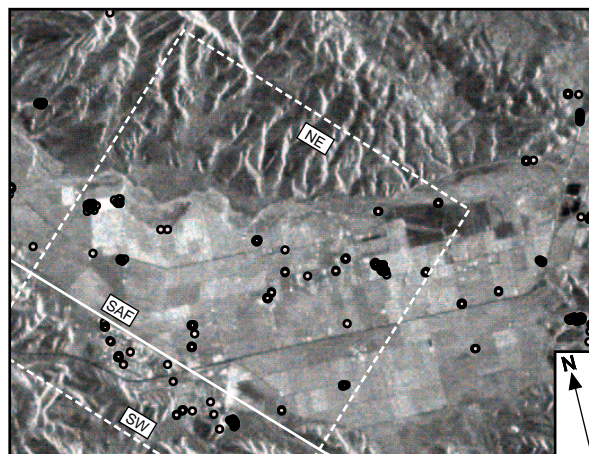


Figure 15.21: InSAR amplitude image of the San Juan Valley showing the locations of 'stable scatterers' (black circles). The dotted line delimits the swath box from which the profile in Figure 3 is extracted. Also shown is the San Andreas Fault (solid line).

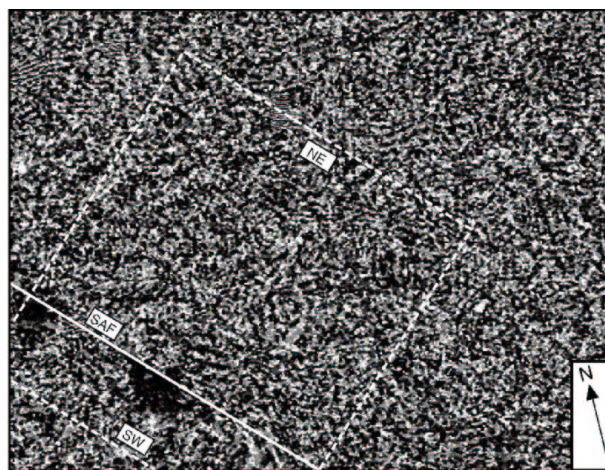


Figure 15.22: Wrapped interferogram corresponding to the area covered in Figure 1 and spanning from May 19, 1996 to August 8, 1998; with a perpendicular baseline of 7 meters. Although the image has been spatially filtered to enhance any signal, random noise still dominates.

9.3 Stable Scatterers

Ferretti et al. (2001) proposed, as a part of their Permanent Scatterer Method, that the stability of individual amplitude and phase measurements across many interferograms be used to identify stable pixels. Buildings (which are often picked as ‘Permanent Scatterers’ because of their good stability) have corner reflecting walls that reflect much more brightly than any surrounding vegetation. ‘Stable scatterers’ can therefore also be identified as points with consistently high amplitudes (Johanson and Bürgmann, 2001). We are implementing this adaptation of the Permanent Scatterer Method to accurately measure surface deformation due to slow earthquakes on the central SAF. InSAR amplitude suggests that there is a sufficient number of potential ‘stable scatterers’ to make this approach viable (Figure 15.21). Across-fault profiles of stable scatterers from our preliminary results are more coherent than randomly chosen points and exhibit geophysically reasonable motions (Figure 15.23). However patches of high scatter in the profile show that additional refinement of our ‘stable scatterer’ definition may be necessary.

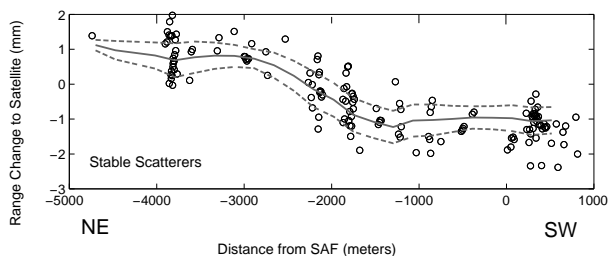


Figure 15.23: Unwrapped profile across the San Andreas Fault of ‘stable scatterers’ contained within the swath box as shown in Figure 1, extracted from an unfiltered version of Figure 2. Wrapped range change values can vary between 1.4 & -1.4 cm. This profile represents a 26% reduction in angular deviation as compared with randomly selected points.

9.4 Future Work

With nearly 100 available interferograms of the central SAF, we plan to construct a time series that can be analyzed together with a campaign GPS data set spanning 1989-2002. Yearly observations of a GPS network covering the Santa Cruz, Hollister, and Salinas areas, have yielded precise measurements of the post-seismic deformation from the 1989 Loma Prieta earthquake and of the regional interseismic deformation. The pattern of ground movement from these processes overprints the deformation pattern from SEQs and should be removed from the InSAR analysis. Another benefit of GPS data is that it measures ground movement in three components and can

provide a basis for differentiating between horizontal and vertical ground movement in the interferograms.

9.5 References

- Ferretti, A., C. Prati, and F. Rocca, Permanent scatterers in SAR interferometry, *IEEE Transactions on Geoscience and Remote Sensing*, 39 (1), 8-20, 2001.
- Gwyther, R.L., C.H. Thurber, M.T. Gladwin, and M. Mee, Seismic and aseismic observations of the 12th august 1998 San Juan Bautista, California m5.3 earthquake, in *3rd San Andreas Fault Conference*, pp. 209-213, Stanford University, 2000.
- Johanson, I.A., and R. Bürgmann, Using point measurements from InSAR to detect transient deformation (abstract), *EOS Transactions, AGU*, 82 (47), 266, 2001.
- Linde, A.T., M.T. Gladwin, M.J.S. Johnston, R.L. Gwyther, and R.G. Bilham, A slow earthquake sequence on the San Andreas Fault, *Nature*, 383 (6595), 65-8, 1996.

10. Crustal Deformation Along the Northern San Andreas Fault System

M. H. Murray

10.1 Introduction

The 100-km wide San Andreas fault system in northern California is composed of three sub-parallel right-lateral faults: the San Andreas, Ma'acama, and Bartlett Springs faults. The San Andreas fault has been essentially aseismic since it last ruptured from San Juan Bautista to Cape Mendocino in the great 1906 San Francisco earthquake. No major earthquakes have occurred during the historical record on the more seismically active Ma'acama, and Bartlett Springs faults, northern extensions of the Hayward-Rodgers Creek and Calaveras-Concord-Green Valley faults in the San Francisco Bay area, but the slip deficit on the Ma'acama fault, based on a high slip rate found by previous geodetic studies, may now be large enough to generate a magnitude 7 earthquake, posing a significant seismic hazard.

In Fall 2002 we will resurvey about 40 monuments that form 4 profiles across the northern San Andreas fault system (Figure 15.24). Most of the monuments were last observed in 1993 or 1995, so the new observations will significantly improve estimates of their relative motion and models of average interseismic strain accumulation, including possible spatial variations along the fault system, and will form the basis for future observations to detect temporal variations in deformation. The monitoring network will provide roughly 10-station profiles every 50 km from Pt. Reyes to Cape Mendocino. We will reprocess the GPS observations using more modern techniques and apply recently developed modeling techniques to provide a more self-consistent description of deformation across northern California and strain accumulation on the northern San Andreas fault system.

10.2 Geodetic Measurements

The northern segment is the youngest portion of the San Andreas fault system, forming in the wake of the northward propagation of the Mendocino triple junction (MTJ) where the Pacific, North America, and Gorda (southern Juan de Fuca) plates meet. The Pacific plate moves northwestward about 35-40 mm/yr relative to central California across a broad 100 km zone in northern California, with the additional motion accommodated in eastern California and the Basin and Range province making up the total relative Pacific-North America, about 50 mm/yr predicted by NUVEL-1A.

Geodetic measurements, which are particularly useful for detecting deformation and strain on deep structures throughout the seismic cycle, currently provide only weak constraints on average strain accumulation for much of

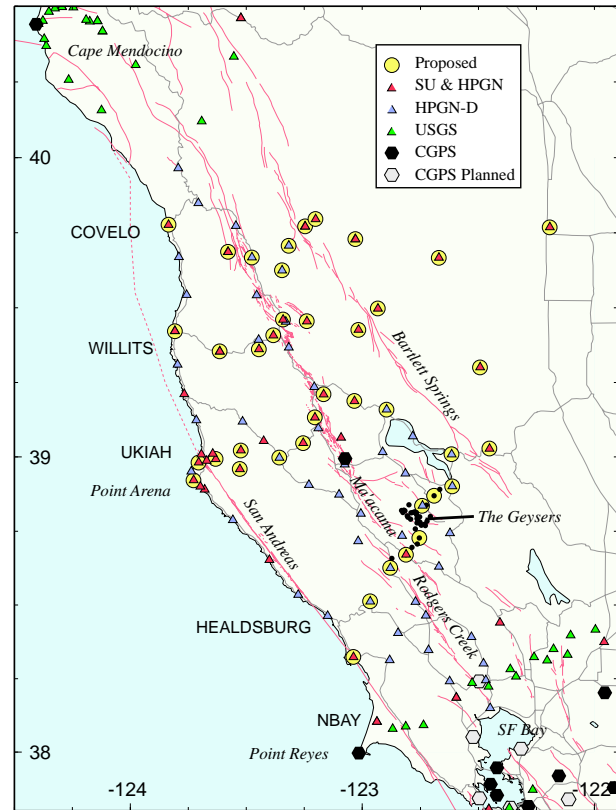


Figure 15.24: GPS sites (circled) to be resurveyed along the northern San Andreas fault system in Fall 2002. Profile names are capitalized. USGS survey-mode sites are observed annually along the NBAY profile and their network near Cape Mendocino were observed in Summer 2001. Only one continuous GPS station (HOPB) at a BSL broadband seismic site near Hopland currently operates in this region.

this region. This is particularly true north of Point Arena, where the San Andreas fault lies offshore and bends 20 clockwise as it comes onshore at Point Delgada before terminating at the Mendocino triple junction near Cape Mendocino. The Ma'acama and Bartlett Springs faults also undergo clockwise rotation to a lesser degree and appear to reactivate older subduction structures as the triple junction migrates northwestward. This complex geometry and other features, such as surface creep on the Ma'acama fault, suggest the deformation may be spatio-temporally variable, similar to deformation that has been observed, and is now being monitored by continuous, frequent survey-mode GPS, and other geodetic

observations, on the southern extensions of these faults in the Bay Area that share many of the same characteristics. Understanding how this spatio-temporal variability affects strain accumulation on the faults is critical for assessment of the timing and hazards posed by future earthquakes.

In *Freymueller et al.* (1999) we reported on data collected in 1991-1995, primarily from the Ukiah and Willits profiles (Figure 15.24). GPS velocities from this network place some constraints on the total slip rate on the San Andreas fault system, which we estimate to be $39.6 \pm 1.5 - 0.6$ mm/yr (68.6% upper and lower confidence intervals from a nonlinear inversion are indicated by subscripts and superscripts). Slip rates on the individual faults are determined less precisely due to the high correlations between estimated slip rates and locking depths, and between slip rates on adjacent faults. Our estimated slip rate on the San Andreas fault is lower than all geologic estimates, although the 95% confidence interval overlaps the range of geologic estimates. Our estimate of the Ma'acama fault slip rate is greater than slip rate estimates for the Hayward or Rodgers Creek faults, its continuation to the south. The Ma'acama fault most likely poses a significant seismic hazard, as it has a high slip rate and a slip deficit large enough to generate a magnitude 7 earthquake today since there have been no significant earthquakes on the fault in the historical record.

10.3 Deformation Modeling

In our *Freymueller et al.* (1999) study, we used a single station constrained to a VLBI-derived velocity to define the velocity reference frame, and were unable to properly account for the far-field motions in terms of angular velocities. We will reanalyze the observations using a more robust, globally defined reference frame that will facilitate application of the angular velocity-fault backslip model (*Murray and Segall, 2001*), and provide a more self-consistent description of northern California deformation. The method can accommodate the observed creep on the faults, and we will also extend the technique to 3D models using backslip on shallow rectangular dislocations in order to investigate the effects of the fault orientations rotating more clockwise at the northernmost segment.

We will investigate the uncertainties of our strain accumulation models using the bootstrap techniques, which provide realistic uncertainties for nonlinear optimization problems. The correlations between slip-rates and locking depths are highly correlated, so that higher slip rates on the San Andreas fault, for example, can tradeoff with lower slip-rates on the Ma'acama fault with almost equal misfit. We will test methods for adding geologic and other information, using Bayesian techniques, to test whether the additional information can reduce the correlations and provide better resolution on other param-

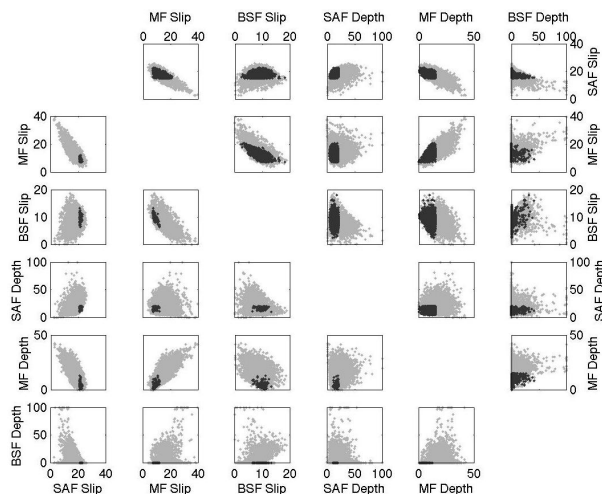


Figure 15.25: Full slip-rate and locking depth covariance for the *Freymueller et al.* (1999) study of the San Andreas (SAF), Ma'acama (MF), and Bartlett Springs (BSF) faults. Shaded areas, the best 95% of the original 10,000 bootstrap trials. Dark shaded areas only, resolution improved by applying Bayesian constraints based on seismic, geodetic, and paleoseismic observations, including maximum locking depths on SAF and MF faults, and minimum slip-rate on the MF. SAF slip-rate constrained to estimates from two recent studies: 21-27 mm/yr (bottom triangle), and 15-23 mm/yr (top triangle).

eters. For example, the previously determined slip-rate on the San Andreas fault ranged from 10.5-22.6 mm/yr at 95% confidence with locking depths ranging 4.7-44.6 km. By applying constraints derived from other seismic, geodetic, and paleoseismic observations, the estimated parameters can be much better resolved (Figure 15.25).

10.4 Acknowledgments

This project is supported by the USGS, through the NEHRP External Grants Program.

10.5 References

- Freymueller, J. T., M. H. Murray, P. Segall, and D. Castillo, Kinematics of the Pacific-North America plate boundary zone, northern California, *J. Geophys. Res.*, *104*, 7419-7442, 1999.
- Murray, M. H., and P. Segall, Modeling broadscale deformation in northern California and Nevada from plate motions and elastic strain accumulation, *Geophys. Res. Lett.*, *28*, 4315-4318, 2001.

11. Urban Geodesy: Monitoring Active Deformation near the Hayward fault

Matthew A. d'Alessio, David Schmidt, Roland Bürgmann, and the UC Berkeley Active Tectonics Group

If you need to take measurements in the middle of a busy intersection, or in a stadium that houses thousands of voracious football fans, or even at a freeway offramp in the middle of rush-hour, you need an urban geodesist. And the Hayward fault, which passes through one of the most densely populated strips in California, is a place where urban geodesy is king.

Geodesy, the science of surveying and measuring the earth's surface, is one of the many tools used by earthquake scientists to understand the behavior of faults. This paper describes the Berkeley Seismological Laboratory's ongoing effort to use geodesy to monitor the movement of the Hayward fault, as well as some of the challenges introduced by doing science in a densely populated urban region.

11.1 Hayward Fault GPS Campaign

The Hayward fault is unique because it not only produces large earthquakes like the estimated M7 1868 earthquake, but it also slowly slips along in a process called aseismic creep. In recent years, the Berkeley Seismological Laboratory has begun utilizing measurements with the Global Positioning System (GPS) to monitor creep along the Hayward fault. This work will provide an unprecedented spatial resolution of GPS measurements about a creeping fault and should allow us to determine where the fault is creeping, how fast it is creeping, and most importantly, how deep the creep extends. Since aseismic creep relieves stress along the fault, identifying locked patches at depth can give us clues to determine where large earthquakes might eventually nucleate and how big they could be.

In a GPS "campaign", we use research-grade GPS equipment to determine the location of a point on the ground to a precision of less than 5 mm. In other words, we can determine locations on earth to within an area half the size of a dime. The next year, we repeat the campaign and return to the exact same location to determine the position again. Because the Hayward fault is slowly creeping along, the spot will have moved; with our high precision positioning, we hope to determine exactly where and how fast. The precision and reliability of our measurements depend on several factors that are all more difficult in the urban setting. See the table on the following page for more details.

As part of the Berkeley Seismological Laboratory's ongoing effort to monitor active deformation along the Hayward fault, we determine positions of over fifty bench-

marks within ten kilometers of the fault (Figure 15.26). Of these fifty monuments, about two thirds of them are in logistically difficult urban settings while the remainder are in the scenic rolling hills that flank the fault. The first surveys of most benchmarks were made in 1998, and our group has been returning each summer to take new measurements.

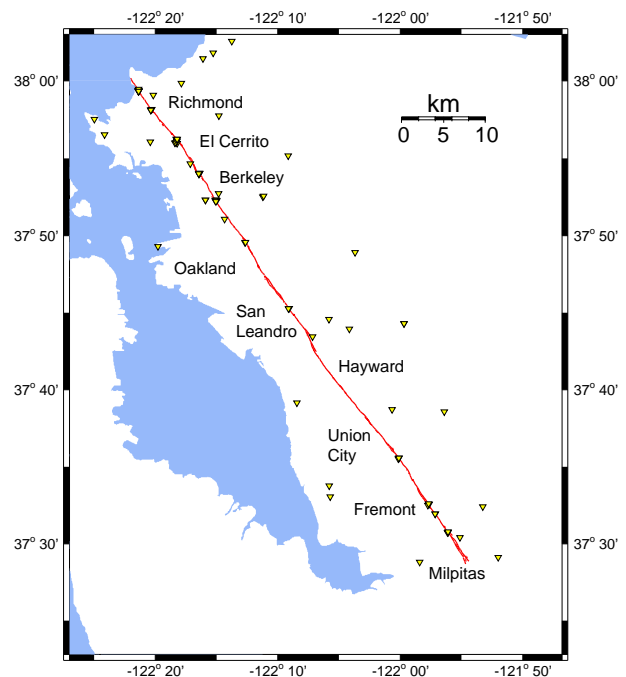


Figure 15.26: The Hayward fault and urban areas of the East Bay. Each triangle shows the location of a benchmark surveyed annually since 1998

11.2 Current Progress

In the last year, the Active Tectonics group purchased seven new, state of the art, geodetic grade GPS receivers. The Trimble 5700 receivers are smaller, lighter, and draw less power than receivers used in the past, making them ideal for both urban geodesy and more remote GPS sites that can only be accessed by hiking. Initial trials using the new receivers show that they produce good quality data that is consistent with the receivers used in past campaigns. The 2002 campaign, which is currently underway, promises to yield excellent estimates of the velocities over the last four years.

Results from our test site at UC Berkeley’s Memorial Stadium appear in Figure 15.27. We should note that in order to take measurements at this site, three of the stations must be set up on staircases inside the stadium, meaning that the operator must make sure that the tripod is perfectly level even though the legs are on a completely uneven surface. Further, the tripod at station STAA must carefully straddle a railing along one stairway. Despite these difficult conditions, our calculations of the fault-parallel velocity across the stadium from these observations is $4.2 \pm 0.3 \text{ mm} \cdot \text{yr}^{-1}$ – in very close agreement with the creep rate determined from off-set curbs along nearby Dwight Way of 3.9 ± 0.1 and $4.1 \pm 0.1 \text{ mm} \cdot \text{yr}^{-1}$. We expect results from the rest of our 2002 campaign (currently underway) to yield equally reliable velocities.

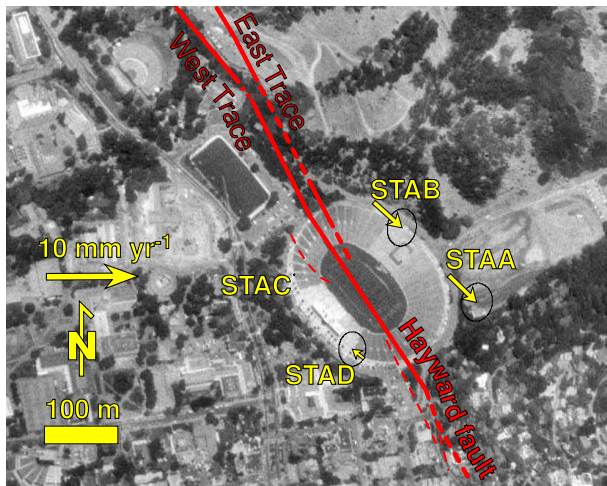


Figure 15.27: Velocities for 1998 - 2002 of four benchmark in UC Berkeley’s Memorial Stadium, shown relative to station STAC. The Hayward fault cuts down the middle of the stadium. These observations show that the Hayward fault creeps at a rate of about $4.2 \pm 0.2 \text{ mm} \cdot \text{yr}^{-1}$. The locations of faults are from a recent paleoseismological report by Geomatrix Consultants, 2001.

11.3 The Challenge

The more densely populated the region, the more valuable seismic hazard assessment becomes. Unfortunately, the more densely populated the region, the more difficult it is to collect reliable data. This is the challenge to the urban geodesist.

11.4 Recipe for High Precision

The following table describes conditions that contribute to high quality estimates of position during a GPS campaign, and why it is challenging to achieve these conditions in the urban environment:

Benchmark Stability	
<i>Explanation</i>	If the location we survey is on unstable ground, the movement we record may not be related to fault motion at all.
<i>Urban Challenges</i>	Near-surface rocks in urban areas are often artificial fill which can be less stable.
Consistent Setup	
<i>Explanation</i>	We must position our instruments in exactly the same location each time with less than a millimeter of tolerance – a job that requires a fair amount of patience, skill, and experience.
<i>Urban Challenges</i>	Even with proper safety gear, try achieving millimeter-level precision in the middle of a busy intersection!
Unobstructed Sky View	
<i>Explanation</i>	GPS receivers determine position by recording broadcasts from satellites orbiting overhead. Overhead obstructions can therefore block or distort the signal.
<i>Urban Challenges</i>	Tall buildings, fences, trees, buses, etc.
Long Duration Measurements	
<i>Explanation</i>	We must collect data for at least 6 to 72 hours continuously. During that time, the instrument must not be disturbed and cannot move even a millimeter.
<i>Urban Challenges</i>	An operator must guard the instrument from both theft and disturbance during the entire time. In busy settings with passing cars, the vibrations can often move the instrument slightly. When placed on asphalt, the instrument can sink into the pavement on hot days.

12. Active Tectonics of the Adriatic Region (Central Mediterranean)

M. Battaglia, M. H. Murray, R. Bürgmann
D. Zuliani, A. Michelini, CRS (Italy)

12.1 Introduction

The Adriatic region can be considered an ideal natural laboratory for studying the kinematics and dynamics of micro-plate tectonics because of the wide variety of tectonic processes encompassed. These include continental collision, subduction of continental and oceanic lithosphere, major continental faults such as the Periadriatic Line, and a variety of smaller scale processes associated with African-Eurasian plate interaction. It is widely accepted that the Adriatic block was originally an African promontory that was indented into the European lithosphere by the convergence of the African and Eurasian plates. However, the present-day kinematics of the Adriatic block are more uncertain: is it still closely connected with the African continent or does it behave as an independent microplate? The distribution of seismicity in the Adriatic region is distinguished by very low seismicity in the plate interior compared to intense activity in the high topographic belts that border the region in the SW, NW and NE. One of the strongest clusters of seismic activity is in the greater Friuli region, located at the convergent NE edge of the Adriatic region, where the Ms=6.5 1976 Friuli earthquake caused widespread damage.

12.2 Geodetic monitoring in the Friuli Seismic Zone

The Friuli Regional Deformation network (FReDNet) of continuously operating Global Positioning System (GPS) receivers monitors crustal deformation along northeast boundary of the Adriatic microplate, which in the Friuli region is thought to be on the order of 5 mm/yr north-south convergence. FReDNet is operated by the Centro Ricerche Sismologiche (CRS) of the Istituto Nazionale di Oceanografia e di Geofisica Sperimentale (OGS). The principal goals of the FReDNet program are to determine the distribution of deformation in this region, to estimate interseismic strain accumulation on its active faults to better assess seismic hazards, to monitor hazardous faults for emergency response management, and to provide infrastructure for geodetic data management and processing. FReDNet will also be part of a proposed larger program of geodetic monitoring of the Adriatic microplate that includes repeating episodic measurements of geodetic points (e.g., points of the IGM95 geodetic network).

In June 2002, Maurizio Battaglia and Mark Murray visited the CRS in Udine, located in the central Friuli region, to assist in site reconnaissance, permitting, and

installation of the first FReDNet stations, and to initiate data acquisition, quality checking, archiving, and analysis. Most of the stations will be collocated with broadband seismometers maintained by the OGS, allowing us to employ some of the procedures developed at the BSL to integrate geodetic and seismic data from the BARD and BDSN networks. In April 2002, David Zuliani of the CRS visited the BSL to better study these procedures.

The CRS purchased 6 Ashtech Micro-Z GPS receivers with chokering antennas for the initial deployment of the new continuous stations. We inspected 5 sites with acceptable sky visibility for GPS observations. Four of the sites are collocated with existing seismic stations (ZOU, LSR, CAE, and MPRI, Figure 15.28), all within the southern Alpine foothills in north Friuli. The southern Friuli region is overlain by Quaternary sediment deposits that are not suitable for GPS monuments needing long-term stability. However, at the Medea site a block of Jurassic sandstones has been uplifted, providing a more tectonically stable setting for the GPS monument. Except for ZOU, additional permitting was required at all the sites. Currently, we have obtained permits for all the sites except LSR, although the fees requested for the CAE site were deemed to prohibitive. We are now pursuing an alternative site at Faloria (AFL), collocated with a seismic station in the Dolomites to the west of Friuli. A sixth station will be located near the main OGS campus in Trieste for demonstration purposes.

In June 2002, we installed the GPS station ZOUF at Zouf Plan, collocated with the ZOU seismic station (Figure 15.29). A 1-m concrete pier was attached to surface bedrock using epoxied metal rods, and the chokering antenna was attached to the monument using a SCIGN antenna adapter and covered with a SCIGN dome. The antenna cable was trenched to a nearby building housing the seismic data loggers and GPS receiver. Cellular modems are used to telemeter the data once per day, using SHARC/EGADS to control the data retrieval. A second station (UDIN) was installed on the roof of a CRS building in Udine for testing purposes. In July 2002, the monument at Monte Prat (MPRI) was installed (Figure 15.30). The CRS is currently resolving problems telemetering the data from this station.

We installed the GAMIT/GLOBK GPS analysis package on a Linux computer at CRS, and initiated automatic processing of the data from ZOUF and UDIN, in combination with other EUREF continuous stations. Preliminary analysis shows short-term repeatabilities in the horizontal components of 2 mm in the north and 4 mm

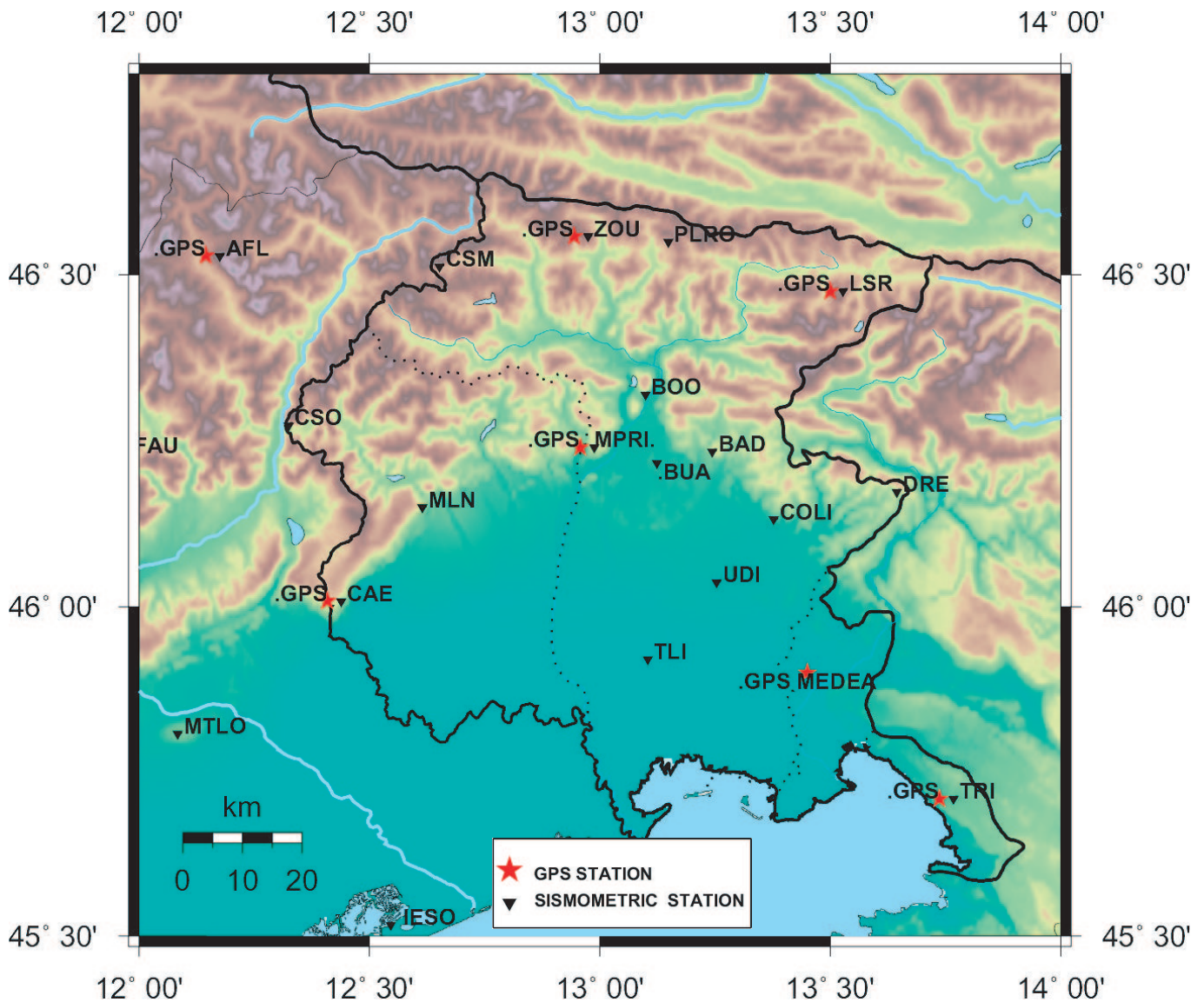


Figure 15.28: Existing and planned GPS continuous stations of the FReDNet in the Friuli region, northeastern Italy. Stations IESO is near Venice, TRI is near Trieste and the border with Slovenia, and ZOU is near the Austrian border. Red stars, GPS stations. Triangles, CRS seismic stations monitoring the Friuli seismic zone. Epicenter of the Ms=6.5 1976 Friuli earthquake is near the station BOO.

in the east. The higher east repeatabilities are mostly likely due to poor phase ambiguity resolution between the FReDNet and EUREF sites, which are over 100 km distant. These results should improve as the other FReDNet stations are installed, providing short distances that can be more easily resolved.

In the coming year, the CRS plans to finish the installation of the 6 initial stations and make the data publicly available, and we will continue to assist them in processing the observations in combination with other European stations in order to obtain initial estimates of the rate of convergence across the Friuli Seismic Zone.

12.3 Acknowledgements

We thank the staff of the CRS/OGS for their abundant assistance and hospitality during the station installations, particularly Alberto Michelini, David Zuliani, Giorgio Duri, Fausto Ponton, Paolo Di Bartolomeo, Gianni Bressan, Aladino Govoni, and Pier Luigi Bragato. This project is partially supported by the Centro Ricerche Sismologiche (CRS) of the Istituto Nazionale di Oceanografia e di Geofisica Sperimentale (OGS), Trieste, Italy.



Figure 15.29: GPS station at Zouf Plan (ZOUF), collocated with seismic station ZOU. The 1-m high concrete pier with GPS antenna and dome mounted on top are on the right. Solar panels and radio antenna mast for the seismic station are on the left.



Figure 15.30: Installation of the GPS monument at MPRI. Concrete pier is tied to near surface bedrock using epoxied steel bars. A compass attached to a wooden rod is here being used to orient the antenna adapter to north.

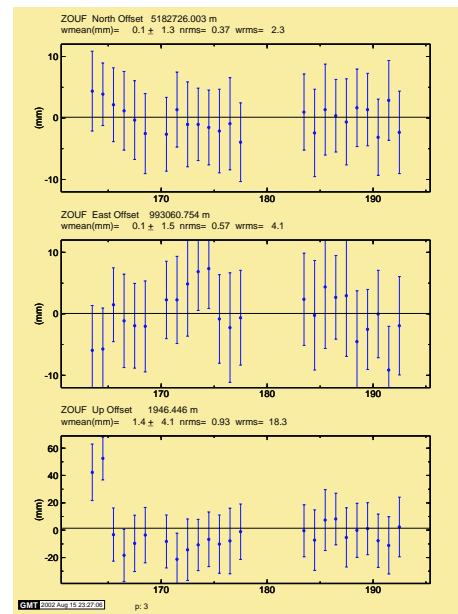


Figure 15.31: Preliminary position estimates of ZOUF relative to a European fixed reference frame defined by several IGS stations. Short-term repeatabilities are typical for unresolved phase ambiguity solutions.

13. Fluid Influenced Faulting in Long Valley Caldera

Dennise Templeton and Douglas Dreger

13.1 Introduction

The most recent episode of unrest in the Long Valley Caldera (LVC) manifested itself in 1997 as an increase in the rate of inflation of the resurgent dome and an increase in seismic activity in the south moat. Ground deformation in the LVC reached a peak in November 1997 and was accompanied by three M4 earthquakes with significant volumetric components, indicating that fluids were involved in the source process of these earthquakes (Dreger *et al.*, 2000). This project seeks to ascertain the extent of fluid influenced faulting triggered by the hydrothermal or magmatic system under LVC.

13.2 Moment Tensor Inversion

We inverted regional broadband data to compute deviatoric and full moment tensor (FMT) solutions for events greater than M4.0 since 1993. We solve for the FMT to determine the coseismic volume changes in the source region and compare it to the deviatoric solution which assumes no volume change. We performed a time domain inversion of complete three-component displacement seismograms. Seven stations were chosen within the Berkeley Digital Seismic Network (BDSN) that provided the best azimuthal coverage and data quality. Green's functions were computed using the SoCal velocity model which is appropriate for the eastern California and Sierra Nevada regions. Both the data and the Green's functions were bandpass filtered between 0.02 to 0.05 Hz using a causal Butterworth filter.

The F-test was used to determine if the improvement in fit between the deviatoric and FMT solutions is significant. The volumetric components of FMT solutions which exceed the 90% confidence level are taken to be statistically significant. To determine the stability of our solution, we use a Jackknife test to iterate over all possible subsets of data. Solutions from different station combinations can be compared to determine if solutions are stable or are influenced by path effects. The results from this test indicate that our solutions are stable for sub-station combinations of two or more.

In the original study of the 1997 swarm, four earthquakes were found to have significant volumetric components including one which had waveforms similar to nearby tectonic events. In this more detailed study, the volumetric component of that earthquake was determined not to be statistically significant. In addition to the three 1997 earthquakes that were previously discovered, two other events were found south of the caldera wall with statistically significant volumetric components

(Figure 15.32). These new events were not located near the 1997 events. Instead, they formed part of a 1998 earthquake swarm within the Sierra Nevada block. Interestingly, this sequence had hints of magmatic involvement that suggested some degree of magma or fluid movement (Hough *et al.*, 2000).

The majority of the events in the LVC area do not have significant isotropic components. Out of the 32 events studied with M4.0 or greater, only five earthquakes had a significant volumetric component in their source region. All of the five earthquakes occurred in areas which had evidence suggesting active magmatic activity.

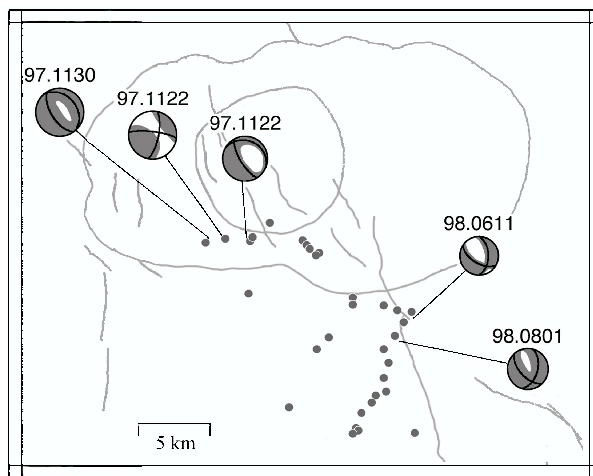


Figure 15.32: Map of LVC, the resurgent dome, and major faults. Seismicity above M4.0 is plotted as circles. FMT solutions are plotted for the five events with significant volumetric components. Event dates, in the form of YY.MMDD, are plotted above the solutions.

13.3 Acknowledgements

We appreciate support for this project by NSF through contract EAR-0087147.

13.4 References

- Dreger, D. S., H. Tkalčić, and M. Johnston, Dilational Processes Accompanying Earthquakes in the Long Valley Caldera, *Science*, 288, 122-125, 2000.
- Hough, S. E., R. S. Dollar, and P. Johnson, The 1998 Earthquake Sequence South of Long Valley Caldera, California: Hints of Magmatic Involvement, *Bull. Seism. Soc. Am.*, 90, 752-763, 2000.

14. Finite Fault Inversion of the September 25, 1999 ($M_w=6.4$) Taiwan Earthquake

Wu-Cheng Chi and Douglas Dreger

14.1 Introduction

More than six M_w 6 and greater aftershocks of the 1999, Chi-Chi, Taiwan earthquake ($M_w=7.6$) were well-recorded. In this study we invert for the finite source rupture process for one of the largest aftershocks (23.86N, 121.01E) that occurred on 1999/9/25 at 23:52:49.5 UTC, 5 days after the mainshock. Through inversions we hope to discriminate the causative fault plane from the auxiliary plane. There are 3 scenarios for the ruptured plane: down-dip extension of the mainshock on the detachment, backthrust above the detachment, and a basement-involved fault below the detachment (Figure 15.33). Although the hypocenter is located in the vicinity of the proposed major shallow east-dipping fault, previous data could not exclude the possibility of a high-angle, west-dipping conjugate fault (backthrust). If true, a backthrust scenario will give us an important constraint on the deep crustal geometry under Taiwan. In addition, recent seismicity studies (e.g. *Carena et. al.*, EOS 82(47), p1176, 2001) show a steep, west-dipping fault below the detachment and the aftershock might have occurred on this fault, if the aftershock focal depth is actually deeper than reported. This scenario implies that large seismic strains can be stored in the footwall of the detachment and future geodynamic studies might need to consider a deformable footwall block that can generate $M_w > 6$ earthquakes. If the rupture was on the proposed detachment, we can delineate its attitude and slip distribution, which can be compared to the mainshock.

14.2 Method and Results

We used strong motion data from the Central Weather Bureau of Taiwan (*Lee at al.*, 2001) to invert the representation theorem for finite source parameters by using the method of *Hartzell and Heaton* (1983). We used a linear least-squares inversion of observed velocity seismograms to compute the spatio-temporal slip distribution. To improve inversion stability, we have applied the following additional constraints: slip-positivity, Laplacian smoothing, and moment minimization. We have performed a grid-search over a range of focal parameters to find the optimal orientation using the variance reduction measure. In total, 1036 inversions were performed and we chose 5/30/100 (variance reduction 73 percent) as our preferred model.

14.3 Interpretation and Conclusion

One surprising outcome from this study is that the strike of our preferred focal mechanism (5) is different from that of teleseismic results (28). An initial teleseismic moment tensor inversion for the Chi-Chi mainshock also gave a strike of 26, compared with the strike of 5 derived from the mainshock surface rupture, thus this discrepancy could be systematic and relate to complex crustal velocity structures underneath Taiwan. The dip is 30 to the east.

The relatively large moment release from this aftershock indicates that its effects should be incorporated into the ongoing aftershock/afterslip studies. Our results might help recalibrate the coseismic/postseismic GPS data. Here we forward modeled the GPS displacements using our slip model in an elastic half space (c.f. *Okada*, 1992). For stations near the aftershock epicenter, most of the horizontal surface displacements are about 1/500 of the observed GPS data from the mainshock. The small displacements are due to the greater depth of this aftershock. However, the displacements can still be up to 3.3 cm at some GPS stations, and thus need to be taken into account in afterslip studies.

14.4 Acknowledgements

We thank Roland Burgmann and David Schmidt for their constructive discussions. This research is partially funded by NSF Grant EAR-0105998.

14.5 References

- Chi, Wu-Cheng, D. Dreger, and A. Kaverina, Finite-source modeling of the 1999 Taiwan (Chi-Chi) Earthquake derived from a dense strong-motion network, *Bull. Seism. Soc. Am.*, 91, 1144-1157, 2001.
- Hartzell, S.H., and T.H. Heaton, Inversion of strong ground motion and teleseismic waveform data for the fault rupture history of the 1979 Imperial Valley, California, Earthquake, *Bull. Seism. Soc. Am.*, 73, 1553-1583, 1983.
- Lee, W. H.K., T.C. Shin, K.W. Kuo, and K.C. Chen, CWB free-field strong-motion data from the 921 Chi-Chi Earthquake: Volume 1. digital acceleration files on CD-ROM, *pre-publication Version (December 6, 1999)*, *Seismology Center, CWB, Taipei, Taiwan*, 1999.
- Okada, Y., Internal deformation due to shear and tensile faults in a half-space, *Bull. Seism. Soc. Am.*, 82, 1018-1040, 1992.

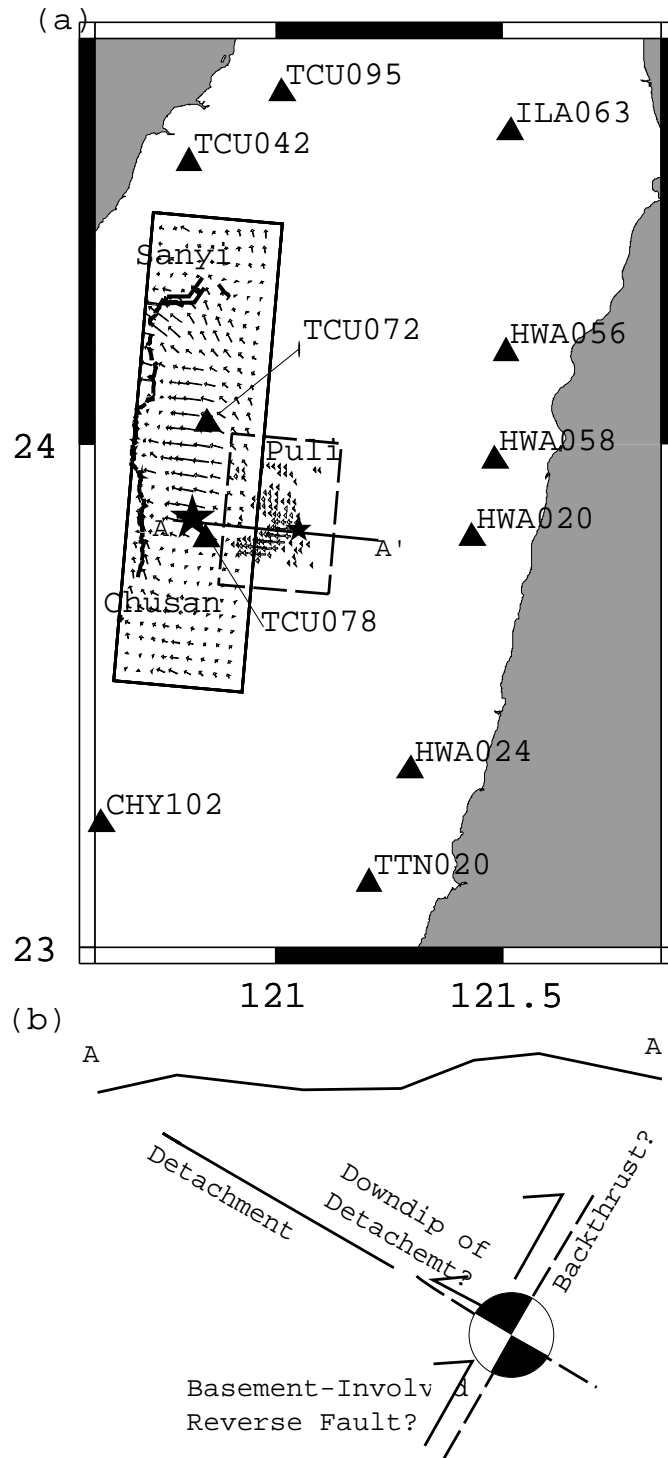


Figure 15.33: (a) Location map. The large star shows the epicenter of the Chi-Chi mainshock and its surface rupture is shown as the thick solid lines. The small star is the epicenter of the 9/25 event from this study. The 11 stations we used to invert the 9/25 event are plotted as triangles. The dense vectors show the 9/25 slip derived from this study. The maximum slip is 1.8 m. The sparse vectors show the mainshock model (*Chi et al.*, 2001), where the maximum slip is 10 m. (b) A schematic cross section along AA', showing 3 possible 9/25 rupture scenarios as discussed in the text.

15. Automated Moment Tensor Software for Monitoring the Comprehensive Test Ban Treaty

Margaret Hellweg, Douglas Dreger, Barbara Romanowicz, Jeffrey Stevens (SAIC)

15.1 Introduction

Seismology makes an important contribution toward monitoring compliance with the Comprehensive Test Ban Treaty (CTBT). One task at the testbed of the Center for Monitoring Research (CMR, Washington DC, USA) and the International Data Center (IDC) of the Comprehensive Test Ban Treaty Organization (CTBTO, Vienna, Austria) is the detection, location and characterization of seismic events in order to distinguish between possible nuclear tests and earthquakes or other natural sources of seismic signals. While this is not particularly difficult for large events, whether natural or man-made, small events present a greater challenge. Although their epicenters and magnitudes can be determined fairly precisely, seismic moment tensor analysis can help in two ways. It not only gives information about the size and mechanism of a source in terms of its seismic moment and the moment tensor components. It provides, in addition, an estimate of the source's depth, which cannot always be reliably determined using normal location techniques. Thus, a large non double-couple component ($> 50\%$) may be an indication for a nuclear explosion, as compared to the typically more than 70-80% double couple for an earthquake (Dreger and Woods, 2002). The source depth determined from moment tensor analysis may also help to weed out tectonic events from among the more than 100000 events of magnitude 4 and greater that occur annually. Only events at shallow depths need be scrutinized by the monitoring process of the Comprehensive Test Ban Treaty (CTBT).

This project's goal is to implement the process for automatic determination of seismic moment tensors routinely used in real-time at the University of California at Berkeley (UCB, Romanowicz et al., 1993; Dreger and Romanowicz, 1994; Pasyanos et al., 1996) on the testbed at CMR. Although the moment tensor process will not be running in real-time on the testbed, in its final implementation it will run automatically, triggered from the Reviewed Event Bulletin (REB). Thus, it will be an additional, potentially powerful event screening procedure (Pechmann et al., 1995; Dreger and Woods, 2002), providing estimates of: (1) the moment magnitude, M_w , a very accurate measure of event size; (2) the source depth, which will help distinguish natural events with typical depths greater than than 1 km from nuclear explosions and (3) radiation characteristics, such as deviations from the typically double-couple radiation of earthquakes.

15.2 Progress and Results

The automated procedure developed at UCB and implemented at CMR uses two methods for determining the moment tensor. One is a time domain, waveform fitting procedure that utilizes the complete, long-period recordings (CW, Dreger and Romanowicz, 1994; Pasyanos et al., 1996; Fukuyama et al., 1998; Fukuyama and Dreger, 2000). The other tensor method fits the surface waves in the frequency domain (SW). It is adapted from the two-step method of Romanowicz (1982).

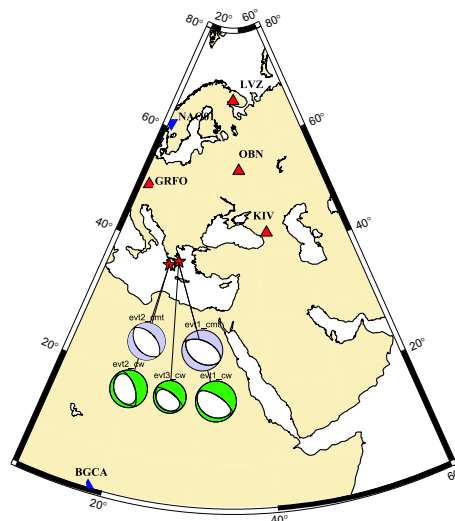


Figure 15.34: Moment tensors solutions (dark, colored) determined using the CW method for events in Greece (Mainshock (evt1): Sep. 07, 1999, M_w 6.0; evt2 M_w 5.6 evt3 M_w 4.8). Inverted triangles denote IMS primary stations, while triangles are auxiliary stations. The light gray solutions for evt1 and evt2 are taken from the Harvard CMT catalog

During the past year, we have completed the installation of the moment tensor codes on the testbed at CMR. The software package now automatically extracts event information and waveform data from the database there, performs basic quality control and preprocesses the waveforms before running the two inversions to produce independent solutions. As testing has proceeded, we have improved the Greens functions produced for the CW method by applying a flattening algorithm to the radially symmetric velocity structures (Müller, 1973, Müller, 1977). We have also adapted the set of periods used for

the SW inversion from those used for the regional application in California to for application world-wide on intermediate-sized events.

We have applied the procedure to events shallower than 200 km with $m_b > 5.4$ in a test dataset, the 90 day interval between from July 19, to October 17, 1999. For the event in Greece on September 7, we have investigated the use of data from auxiliary stations of the IMS network in addition to the primary stations. Figure 15.34 shows results for the mainshock (M_w 6.0) as well as two aftershocks (evt2 M_w 5.6 and evt3 M_w 4.8). Clearly, the method is effective in this region, even for the small aftershock.

For events in the test dataset we have run inversions using two different velocity models. The maps in Figure 15.35 show the IMS stations used for the inversions, as well as the moment tensor solutions determined by the complete waveform inversion and the surface wave method, respectively. In both Figure 15.35 A and B, the solutions derived using two different velocity models are compared with the moment tensors given in the Harvard CMT and USGS catalogs.

While the match between catalog source mechanisms and those calculated using the two automated moment tensor methods is good for some events, for others the process is not so successful. One typical problem is that for this interval, data is not always available from many of the primary stations of the seismic network of the International Monitoring Systems (IMS), the data source for the automatic process. For the CW method, for example, the moment tensors derived for events east and northeast of Australia differ from those given by both the Harvard and USGS catalogs. However, for each of these events, data were only available from one primary station less than 5000 km from the epicenter, STKA. The solutions calculated by the CW method are consistent with the waveforms from this station. The dearth of data is apparent for the SW method in in Figure 15.35 B which shows solutions for only 13 of the 19 events shown in Figure 15.35 A.

15.3 Perspectives

Currently, we are directing our efforts toward three fronts. First, we will attempt to improve the automated procedure by incorporating data from additional stations. Since 1999, the primary stations of the IMS network have been improved, both in their equipment and in their reliability. In addition, many of the auxiliary stations of the IMS network satisfy the need for the broadband, high dynamic range data which is necessary for the methods to work well. We will factor in data from these stations to improve the solutions. Secondly, we are working to develop and apply quantitative comparisons of the moment tensor solutions from various sources, CW or SW methods, as well as Harvard CMT and USGS. Finally,

we are developing a regionalized calibration for the Far East. As part of an advanced concept demonstration, the CMR has collected event information and seismograms, as well as information about the Earth's structure in the region around Lop Nor. We will use this data to generate Greens functions and path information, so that we can calculate moment tensors for events, man-made or natural, occurring in this area.

15.4 Acknowledgements

This project is funded under the Defense Threat Reduction Agency contract DTRA01-00-C-0038.

15.5 References

- Dreger, D. and B. Romanowicz, Source characteristics of events in the San Francisco Bay Region, *USGS Open-file report, 94-176*, 301-309, 1994.
- Dreger D. and B. Woods, Regional Distance Seismic Moment Tensors of Nuclear Explosions, *Tectonophysics*, in press, 2002.
- Fukuyama, E., M. Ishida, D. Dreger, and H. Kawai, Automated seismic moment tensor determination by using on-line broadband seismic waveforms, *Jishin*, 51, 149-156, 1998.
- Fukuyama, E. and D. Dreger, Performance test of an automated moment tensor determination system, *Earth Planets Space*, 52, 383-392, 2000.
- Müller, G., Theoretical Body Wave Seismograms for Media with Spherical symmetry; Discussion and Comparison of Approximate Methods, *J. Geophysics*, 39, 229-246, 1973.
- Müller, G., Earth-Flattening Approximation for Body waves Derived from Geometric Ray Theory; Improvements, Corrections and Range of Applicability, *J. Geophysics*, 42, 429-436, 1977.
- Pasyanos, M., D. Dreger, and B. Romanowicz, Toward real-time estimation of regional moment tensors, *Bull. Seism. Soc. Am.*, 86, 1255-1269, 1996.
- Pechmann, J.C., W.R. Walter, S.J. Nava, and W.J. Arabasz, The February 3, 1995, M_L 5.1 seismic event in the Trona mining district of southwestern Wyoming, *Seis. Res. Lett.*, 66, 25-34, 1995.
- Romanowicz, B., Moment tensor inversion of long period Rayleigh waves: a new approach, *J. Geophys. Res.*, 87, 5395-5407, 1982.
- Romanowicz, B., M. Pasyanos, D. Dreger, and R. Uhrhammer, Monitoring of strain release in central and northern California using broadband data, *Geophys. Res. Lett.*, 20, 1643-1646, 1993.

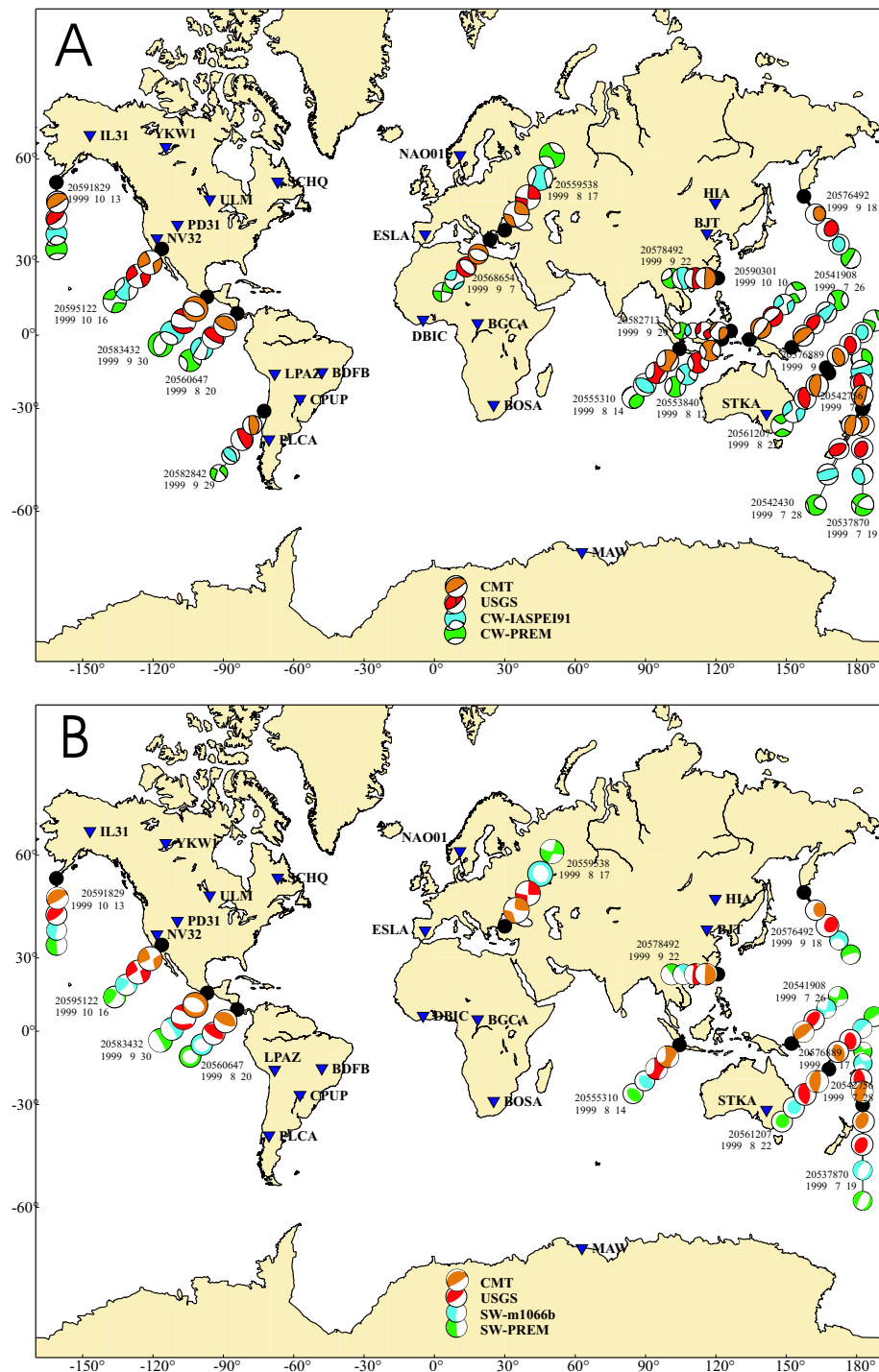
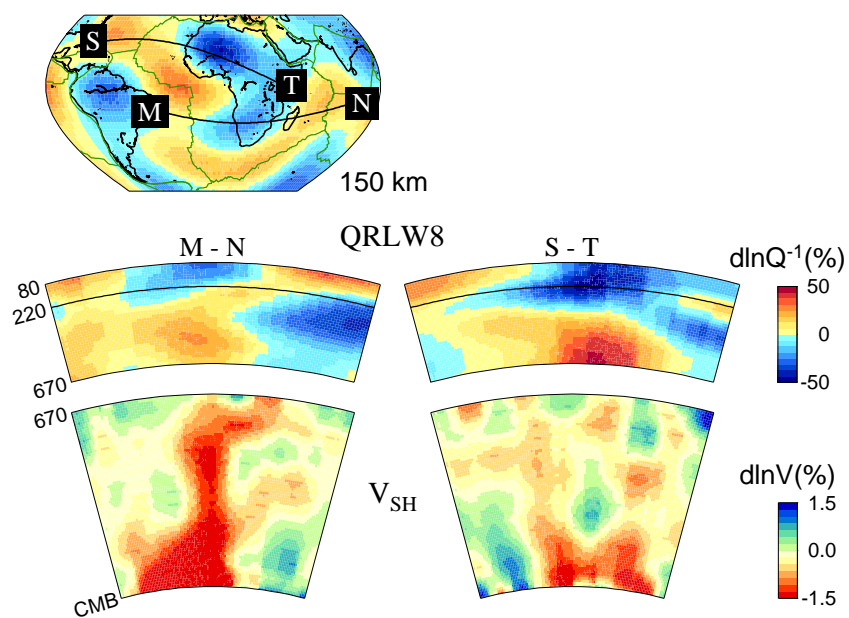


Figure 15.35: (A) Map showing stations (triangles) and inversion results for the complete waveform method. Taken in order from the event hypocenter (dot), focal mechanisms are from the Harvard CMT catalog, USGS catalog, CW method using iasp91 velocity model and CW method using PREM. (B) Map showing stations (triangles) and inversion results for the surface wave method. Taken in order from the event hypocenter (dot), focal mechanisms are from the Harvard CMT catalog, USGS catalog, SW method using m1066b velocity model and SW method using PREM.

Chapter 16

Regional and Global Structure Studies



1. Waveform Constrained Seismic Velocity Structure in Northern California

Junkee Rhie and Douglas S. Dreger

1.1 Introduction

1D and 2D shear wave velocity structure from Mammoth Lakes to Yreka is determined by SH waveform modeling and receiver-function analysis. Three local events are selected by considering epicentral distances from stations and the availability of reliable source parameters (e.g. Dreger *et al.*, 1995). The six teleseismic events are also selected by considering preferred back azimuth and S/N ratio (Figure 16.1). Regional broadband waveforms from the 21 September 1993 Klamath Falls (M_w 6.0), the 15 May 1999 Mammoth Lakes (M_w 6.0), and the 10 August 2001 Portola (M_w 5.2) events were well recorded by 4 to 5 BDSN stations that are also located nearly on the same NNW line (Figure 16.1). This naturally aligned configuration of three local earthquakes and stations provides an excellent opportunity to determine a waveform constrained velocity model along the profile. Before performing the waveform modeling, a receiver function technique is applied to constrain the depth of major discontinuities, especially Moho, at each station. 1D and 2D models are estimated by forward modeling of the broadband waveforms and the receiver-functions.

1.2 Method

Receiver-function analysis is a very appropriate method to look at the discontinuities in the crust and upper-mantle. However, the velocity structure obtained from receiver-function analysis is not unique since receiver-functions, especially the radial components, are mostly sensitive to P to S velocity ratio rather than the absolute velocity at each depth (Ammon *et al.*, 1990). Three component broadband waveforms from regional events are relatively more sensitive to the absolute velocity at each depth. These complementary properties give us a chance to obtain more constrained velocity structure than those obtained by only one or the other of the two methods. Langston (1994) showed that regional broadband waveform modeling based on an initial 1D model obtained by teleseismic receiver function inversion is very promising for the determination of source parameters and to infer details of crustal and upper mantle structure. But he also mentioned that lateral heterogeneity in velocity structure is still an obstacle to overcome. The basic idea of this work is the same as his, but the final goal is to determine 2D or 3D model, which can include the effect of lateral heterogeneities. Many 1D models obtained by waveform modeling of receiver functions and regional broadband waveforms can be used as a basis for

more complex 2D and 3D models. The detailed process of waveform modeling scheme for 1D modeling is as follows; 1) The depth of major discontinuities, especially Moho, is constrained by receiver function inversion. 2) S-wave velocities in each layer are modified to fit the observed SH regional waveform. 3) P-wave velocity is obtained by perturbing P velocity to explain P-SV regional waveforms. 4) The P model can provide more constraint on the depths of major discontinuities identified by the receiver function analysis and then the above process is repeated to obtain a reliable 1D model, which can explain receiver function and regional waveforms simultaneously. The more complex 2D or 3D model will be estimated based on many 1D models.

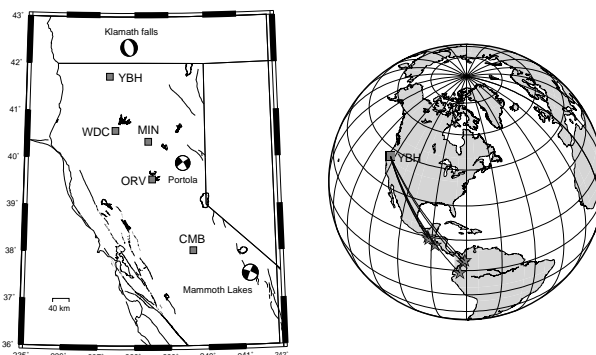


Figure 16.1: Location map of stations and events for regional (left) and teleseismic (right) cases. The regional events and broad band stations are located on the NNW line. The teleseismic events of which back azimuth from BDSN is similar to the trend of NNW line was selected for receiver function analysis

1.3 Discussion and Results

A preliminary 2D shear wave velocity model for NNW profile in northern California was estimated. Three 1D models for the S structure under YBH, ORV and CMB stations are interpolated to get the 2D result. Stacked waveforms from teleseismic events are used as input waveforms for receiver function calculation. Tangential component of regional waveforms recorded at the three BDSN stations are modeled by forward waveform modeling approach with fixed depths of major discontinuities that were obtained from receiver function inversion. The variance reductions of each waveform fit are all about

60 % or larger, even for frequencies up to 0.5 Hz (Figure 16.2). Although we did not give more constraint on depths of major discontinuities by P-SV waveform modeling, the obtained 1D models seem to be able to explain regional tangential waveforms well. However, this 1D model cannot explain receiver functions simultaneously (Figure 16.2). The preliminary 2D model based on an interpolation of given 1D models from waveform modeling cannot explain the waveforms which propagated along the NNW line. However, this model roughly shows the reasonable variation of the velocity structure along the NNW line; deeper Moho and higher velocity layer under Sierra Nevada and shallower Moho and lower velocity layer under Klamath Mountains (Figure 16.3). The further direction of this study will be to estimate 1D models which can explain waveform of regional events and receiver functions simultaneously. P-SV waveforms will be incorporated and the results of the 1D analyses will be used to construct a 2D model for the path. In addition, other source-receiver pairs and receiver functions with wide variety of back azimuth will be used to estimate 3D velocity structure model.

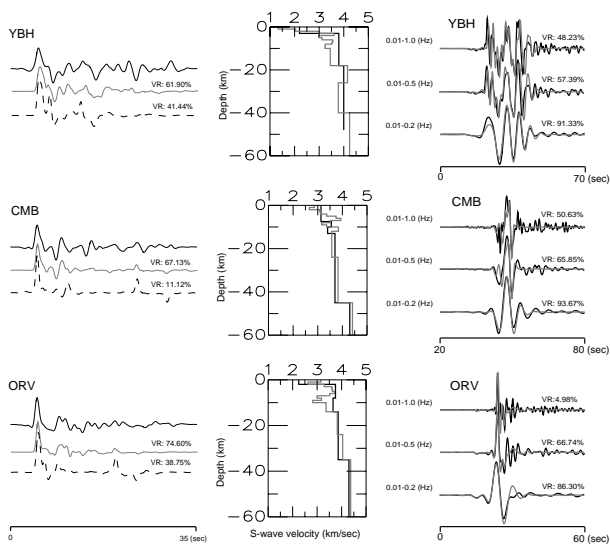


Figure 16.2: Preferred receiver function models (grey) and refined models (black). The refined models were obtained by forward waveform modeling. Left: Radial component receiver function based on receiver function model (grey) and refined model (dotted). Right: Comparison between observed (black) and synthetic tangential waveforms (grey) for refined model

1.4 Acknowledgements

We thank C. Ammon for letting us apply his RFTN software package to all receiver-function related calculations.

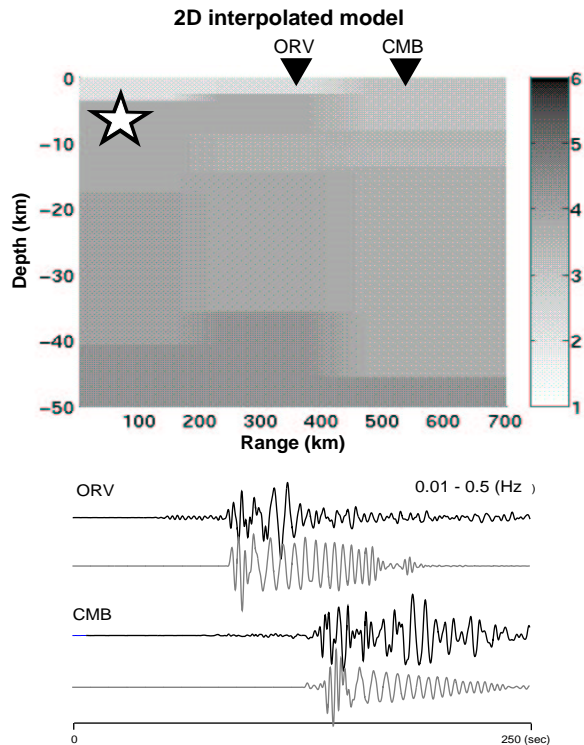


Figure 16.3: The preliminary 2D shear wave velocity model is constrained using three 1D models obtained from regional waveform modeling. Comparison between observed (black) and synthetic tangential waveforms (grey) for interpolated model

1.5 References

Ammon, C. J., G. E. Randall, and G. Zandt, On the non-uniqueness of receiver function inversions, *J. Geophys. Res.*, *95*, 15,303-15,318, 1990.
 Dreger, D., J. Ritsema, and M. Pasyanos, Broadband analysis of the 21 September, 1993 Klamath Falls earthquake sequence, *Geophys. Res. Lett.*, *22*, 997-1000, 1995.
 Langston, C., An integrated study of crustal structure and regional wave propagation for southeastern Missouri, *Bull. Seism. Soc. Am.*, *84*, 105-118, 1994.

2. Detection and Location of Potential Sources of Background Low Frequency Surface Wave Energy

Junkee Rhie and Barbara Romanowicz

2.1 Introduction

Earth's background free oscillations were reported recently by *Nawa et al.* (1998). They observed the excitation of the peaks of fundamental spheroidal modes on superconducting gravimeter data in the frequency range between 0.3 to 5 mHz even during periods of no significant earthquakes. Numerous observations and studies strongly suggest that this phenomenon is real and the coupling of the solid earth with the atmosphere/ocean system is likely involved in source mechanism (*Suda, et al.*, 1998; *Tanimoto et al.*, 1998; *Kobayashi and Nishida*, 1998; *Ekström*, 2001). However, the spatial distribution of the sources remains unknown. Previous studies use stacking of power spectral density and correlating multi-orbit surface waves but provide no spatial resolution of the sources. To locate the sources and better understand the source, an array-based method, a modification of the autogram method (*Ekström*, 2001), can be a useful tool.

2.2 Array-based method

There are two basic assumptions of an array-based method: one is that we can approximately map a long-period surface wave field recorded at given station onto any reference point with same back azimuth by introducing some parameters obtained from the spherically symmetric reference earth model (e.g. PREM). We also assume that the surface wave energy propagates as a plane wave if the source is far from the array (Figure 16.4).

We use vertical component recordings at BDSN array. Instrument response is removed and band-pass filter (100-500 sec) is applied. We first map the surface wave field at a given station onto a reference point which is inside the array. The mapping is performed by deconvolving transfer function $T(\omega, \delta X)$, which represents the propagation effects of surface wave between a given station and reference point. The second step is to break up the deconvolved records into successive time intervals with duration of 500 sec and lagged by 100 sec. The records in each time interval are divided into two subsets, "far" and "near" stations, with respect to the chosen back azimuth. We then stack the records in each subset and each time interval separately. The final step is to compare these two stacked records corresponding to "far" and "near" stations by calculating variance reduction. The above processes are repeated for all possible back azimuths. Final output of the given process is variance reduction as a function of time and back azimuth. Our preliminary results for several known teleseismic events

show that the lower threshold of detection can be down to M_w 5.5. And we can get a rough estimate of back azimuth for the source and arrival time of surface wave energy. To locate the sources of the long period surface wave energy, we need other dense arrays, such as arrays in Japan and Germany. Three different estimates of back azimuths and absolute arrival times will better constrain the source location.

Scanning available records from the past 5 years to search for the sources of long period surface wave energy not related to known events is further direction of this work.

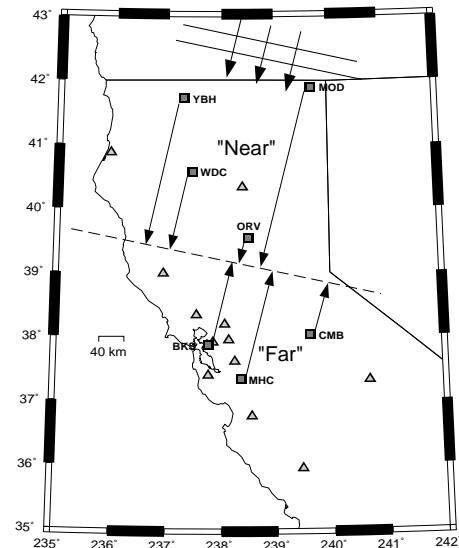


Figure 16.4: Map of northern California showing the incidence of a surface wave as a plane wave (solid lines and arrows) on BDSN. Squares: quietest BDSN stations. These were used in example plot, except MOD which was installed in 2001. Triangles: other BDSN stations. The broken line indicates the reference line onto which the waveforms are back (or forward) projected before stacking

2.3 Discussion

The current goal of this work is to estimate the spatial distribution of the sources of background free oscillations. As we mentioned before, our preliminary result shows that the detection limit of this method is at least M_w 5.5 (Figure 16.5). This magnitude is less than the doc-

umented level of equivalent magnitudes of excitation of background free oscillation, which are 6.0 or 5.75 based on different approaches (Tanimoto and Um, 1999; Ekström, 2001). It implies that we can detect the long period surface wave energy when only one localized source produces equivalent moment. However, it is also possi-

mal stacking scheme and grouping of stations, as well as the choice of traces. Even if we cannot locate the source associated with background free oscillations due to very broad distribution of sources in time and space (Nishida and Kobayashi, 1999), this methodology will still be useful in searching for the silent/slow earthquakes or automatic identification and preliminary location of teleseismic events using a small number of local arrays.

2.4 References

Ekström, G., Time domain analysis of Earth's long-period background seismic radiation, *J. Geophys. Res.*, *106*, 26483-26493, 2001.

Kobayashi, N., and K. Nishida, Continuous excitation of planetary free oscillations by atmospheric disturbances, *Nature*, *395*, 357-360, 1998.

Nawa, K., N. Suda, Y. Fukao, T. Sato, Y. Aoyama, and K. Shibuya, Incessant excitation of the Earth's free oscillations, *Earth Planets Space*, *50*, 3-8, 1998.

Nishida, K. and N. Kobayashi, Statistical features of Earth's continuous free oscillations, *J. Geophys. Res.*, *104*, 28741-28750, 1999.

Suda, N., K. Nawa, and Y. Fukao, Earth's background free oscillations, *Science*, *279*, 2089-2091, 1998.

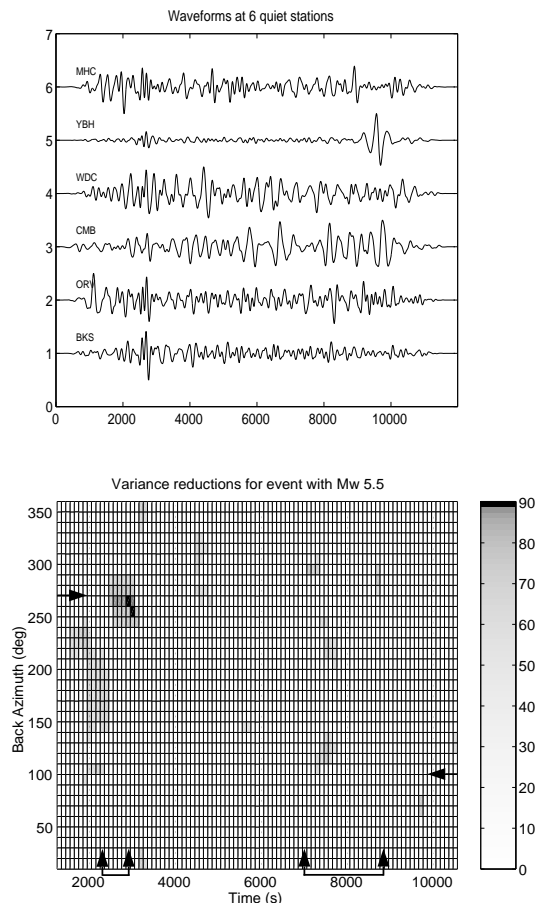


Figure 16.5: Examples of analysis for an event of M_w 5.5 in new Ireland region (10/12/1999), depth = 15km, distance = 89.5 deg, backazimuth = 265.5 deg). Top: waveforms at 6 quiet stations, bandpass filtered between 100 and 500 sec. Time starts from origin time of the event. Bottom: detection result: maximum variance reduction (scale shown on the right) corresponds to the arrival of R1. Arrows indicate expected back azimuths and arrival intervals for R1 and R2 corresponding to group velocities between 4.3 and 3.4 km/s. Station YBH exhibits a glitch around 9000 sec. For this smaller magnitude event, and the period range considered, only R1 is clearly detected

ble that the previous estimates of equivalent moments are due to numerous localized or broadly distributed sources. In this case, we need a more robust method. We are trying to optimize the method to increase the detection limit by fine tuning optimal duration of interval, opti-

3. Global Anisotropy beneath Continental Roots

Yuancheng Gung, Mark Panning and Barbara Romanowicz

3.1 Introduction

The spatial distribution of seismic velocity revealed by global tomography has been a powerful tool in understanding the internal structure of the Earth. In the uppermost mantle, the higher than average velocity under continents is commonly interpreted as the signature of continental roots, as they are presumably colder than their surrounding. In general, the extension of this signature in depth correlates to the lithospheric thickness. However, this seismically defined thickness of continental roots shows diverse features among the recent global tomographic models. Unlike the well documented anisotropic feature under Centre Pacific (e.g. *Montagner and Tanimoto, 1991; Ekström and Dziewonski, 1998*), these dissimilar features below lithospheric depth are less explored, and are generally accepted as a result of various data coverage and different methodology.

Here we present results from a global tomographic model derived by using joint anisotropic inversion of V_{SV} and V_{SH} . Our results demonstrate that these diverse characteristics can be explained by the ubiquitous existence of transverse anisotropy beneath major continental shields.

3.2 Methodology

Separate isotropic inversion of Love and Rayleigh waves is a convenient approach to measure the anisotropy in the uppermost mantle based on the fact that the fundamental modes of Love/Rayleigh waves are mainly sensitive to V_{SH}/V_{SV} . However, the condition is not generally true for overtone phases (Figure 16.6), and it limits the resolution of the anisotropic features derived from the pseudo-isotropic inversion (e.g. *Regan and Anderson, 1984*).

In this study, we implement a joint inversion on three component seismic waveform data. The sensitivity kernels of V_{SV} , V_{SH} , η , $V_{P_{iso}}$ (isotropic V_P), ϕ , and ρ are calculated based on the assumption of weak transverse anisotropy. Starting from our most recent tomographic models, SAW24B16 (*Mégnin and Romanowicz, 2001*) for V_{SH} and SAW16BV (*Gung and Romanowicz, 2002; Romanowicz and Gung, 2002*) for V_{SV} , we invert for V_{SH} and V_{SV} up to degree 16. The scaling relations among anisotropic parameters ϕ , ξ and η based on *Montagner and Anderson (1989)* are applied. This allows us to incorporate the effects of V_{SV} on Love waves, V_{SH} on Rayleigh waves and the effects of P anisotropy. Since SV component data have less sensitivity in the lowermost mantle than SH component data, to avoid the bias from

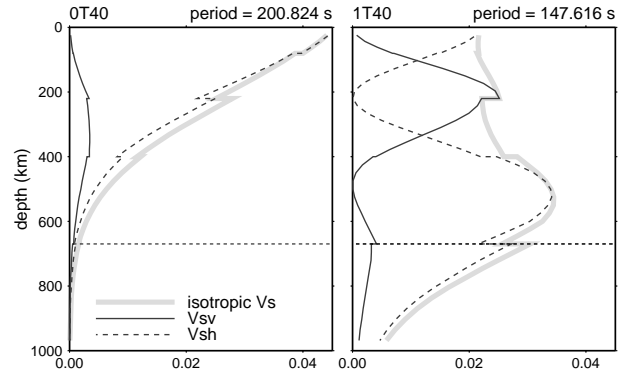


Figure 16.6: Sensitivity kernels of isotropic V_S and anisotropic V_{SV} and V_{SH} for fundamental mode ${}_0T_{40}$ and overtone ${}_1T_{40}$.

anisotropic features from the deep mantle, we have restricted our inversion to the top 1500km of the mantle in this study.

3.3 Data

Three component waveform data composed of surface waves ($\approx 85,000$ wavepackets) and body waves ($\approx 60,000$ wavepackets) are used in this study. In addition to fundamental surface waves, we also include overtone phases, which greatly enhance the resolution in the upper mantle transition zone.

3.4 Preliminary results and discussion

Figure 16.7 shows our preliminary results of depths 175km and 250km. It is observed that the major features in V_{SV} and V_{SH} from the separate inversions are preserved in this depth range. Probably because it is mainly constrained by fundamental surface waves.

At the depth of 175km, the Pacific region shows similar anisotropic features as previous studies (e.g. *Montagner and Tanimoto, 1991; Ekström and Dziewonski, 1998*) most areas at this depth are characterized by $V_{SH} > V_{SV}$. There are two prominent exceptions in our model: East Pacific Rise and regions around Hawaii islands, where we observe strong signal of $V_{SV} > V_{SH}$, presumably due to vertical flow.

The anisotropy under oceanic regions at larger depth (250km) becomes weaker, and the contrast between V_{SV} and V_{SH} is highlighted in the continental regions. We observe that most continental shields are characterized by $V_{SH} > V_{SV}$, such as Canadian shield, Siberia platform,

Baltic shields, West Africa, Amazonian and Australian craton.

We propose that this anisotropy, characterized by $V_{SH} > V_{SV}$, is due to asthenospheric horizontal flow underneath the continental lithosphere. Similar to what happens under the Pacific plate, albeit at shallower depth (because the lithosphere is thinner). We also propose that this strong anisotropy under continents marks the Lehmann discontinuity, and the anisotropy under oceanic plates marks the G discontinuity. This explains the geographic preferential detections of these two discontinuities. (Gu, Dziewonski and Ekström, 2001; Revenaugh J. and T. H. Jordan, 1996)

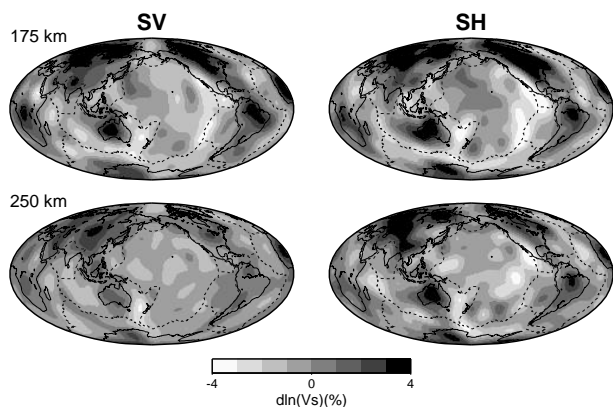


Figure 16.7: Lateral variations in V_{SV} and V_{SH} at the depth 175km and 250km.

3.5 Acknowledgements

We thank the National Science Foundation for support of this research.

3.6 References

Ekström, G. and A. M. Dziewonski, The unique anisotropy of the Pacific upper mantle, *Nature*, 394, 168-171, 1998.

Gu, Yu. J., Dziewonski Adam, and Ekström G., Preferential detection of Lehmann discontinuity beneath continents, *Geophys. Res. Lett.* 28, 4655-4658, 2001

Gung, Y., and B. Romanowicz, Q tomography of the upper mantle using three component long period waveforms, submitted to *Geophys. J. Res.*, 2002

Li, X.D. and B. Romanowicz, Global mantle shear-velocity model developed using nonlinear asymptotic coupling theory, *Geophys. J. R. Astr. Soc.*, 101, 22,245-22,272, 1996.

Mégnin, C., and B. Romanowicz, The 3-D shear velocity structure of the mantle from the inversion of body, surface, and higher mode waveforms, *Geophys. J. Inter.*, 143 709-728, 2001.

Montagner J. P. and Don L. Anderson, Petrological constraints on seismic anisotropy, *Phys. Earth and Plan. Int.*, 54, 82-105, 1989.

Montagner J. P. and T. Tanimoto, Global upper mantle tomography of seismic velocities and anisotropies, *Geophys. J. Res.* 96,, 20,337-20,351, 1991.

Regan, Janice and Don L. Anderson, Anisotropic model of the upper mantle, *Phys. Earth and Plan. Int.*, 35, 227-263, 1984.

Revenaugh J. and T. H. Jordan, Mantle layering from ScS reverberations 3. the upper mantle *Geophys. J. Res.* 96,, 19,781-19,810, 1991.

Romanowicz, B., and Y. Gung, Superplumes from the core-mantle boundary to the lithosphere: implications for heat flux, *Science*, 296, 513-516, 2002.

4. Superplumes from the core-mantle boundary to the base of the lithosphere: evidence from Q tomography

Yuancheng Gung and Barbara Romanowicz

4.1 Introduction

Global seismic tomography aims at improving our understanding of mantle dynamics by providing constraints on three-dimensional (3D) temperature and composition, using elastic velocities as proxies. Much progress has been made in recent years in resolving increasingly finer details in the 3D distribution of elastic velocities from the inversion of seismic phase and travel time data. However, the detailed morphology and role of upwellings, as manifested by two prominent zones of lower than average velocity, commonly referred to as superplumes, in the lowermost mantle, is not yet clear. Their location, under the south-central Pacific and under Africa, correlates with the global distribution of hotspots, as well as two major geoid highs. Recent tomographic S wave velocity models suggest that the superplumes rise high above the core-mantle boundary (CMB) *Mégnin and Romanowicz, 2000; Ritsema et al., 1999*, and joint seismic/geodynamic studies imply that they may be active upwellings (*Forte and Mitrovica, 2001*). However, finer scale resolution is still lacking.

To obtain additional constraints on hotter than average features, we consider amplitudes of seismic waves, which are sensitive to 3D anelastic structure. Owing to the exponential dependence on temperature of attenuation, which we shall express in terms of Q^{-1} , where Q is the quality factor, we expect anelastic tomography to highlight hotter than average regions better than standard elastic tomographic approaches.

4.2 Data and Inversion results

We have developed a waveform tomographic inversion method, originally aimed at constructing global 3D elastic models of the whole mantle (*Li and Romanowicz, 1996*), which now has been extended to iteratively solve for elastic and anelastic structure in the upper mantle, using three-component waveform data of fundamental and higher mode surface waves (*Gung and Romanowicz, 2002*). While we do not directly account for elastic effects in the amplitudes, strict data selection criteria are designed to reject data most strongly contaminated by focusing. The first step (elastic inversion) allows us to align the phases in our waveforms, and we do so separately for SV sensitive (vertical and longitudinal S wave component) and SH sensitive (transverse S wave component) data, to account for anisotropy in the uppermost mantle. In the second step, the Q^{-1} model, *QRLW8*, is derived using all three component data.

In the top 250 km of the mantle, correlation of high Q regions with shields is seen systematically in North and South America, Eurasia, Australia and Antarctica, whereas mid-ocean ridges in the Pacific, Atlantic and Indian Ocean exhibit generally low Q values, as do western Pacific back-arc regions (Figure 16.8). This is similar to what is observed in elastic velocity models, with regions of high/low velocity correlated with regions of high/low Q. A notable exception is an elongated zone of high attenuation in the central Pacific, extending from south of the equator to Hawaii, not seen in *SH* velocity models at these depths. Below 250 km, this tectonics-related Q distribution is gradually replaced by a simpler pattern, with two strong attenuation maxima centered in the southern Pacific and under Africa, throughout the upper mantle transition-zone. At depths greater than 400 km, a majority of hotspots are located above regions of high attenuation.

In model *QRLW8*, the high attenuation regions in the transition zone coincide in location with the minima in elastic velocity associated with the two superplumes in the lowermost mantle. Correlation between Q in the transition zone and velocity in the last 500 km of the mantle is particularly strong at degree 2 (Figure 16.9), but persist at shorter wavelengths. Cross-sections in the Pacific and under Africa (Figure 16.10) comparing upper mantle Q^{-1} with lower mantle velocity distributions, emphasize the vertical correspondence of the lowermost mantle superplumes with transition zone low Q zones. Because our Q^{-1} model does not extend to the lower mantle, and the low velocity zones are only expressed faintly in the upper half of the lower mantle, where they appear to be narrower and have a contorted shape, it is not possible to determine whether the superplumes are simply continuous across the 670 km discontinuity, or whether they induce rising hot currents in the upper mantle through thermal coupling processes. However, our results show that the superplumes must carry enough energy across the lower mantle to create coherent upwelling flow in the upper mantle transition zone, in agreement with mantle flow models. In contrast, ridges are shallow high attenuation features, mostly confined to the upper 200 km of the mantle.

The low Q zones in the transition zone connect with shallower ones whose positions are shifted horizontally, suggesting that the upwelling, plume related flow is deflected horizontally below the cold lithosphere, towards the Indian and Atlantic mid-ocean ridges under Africa,

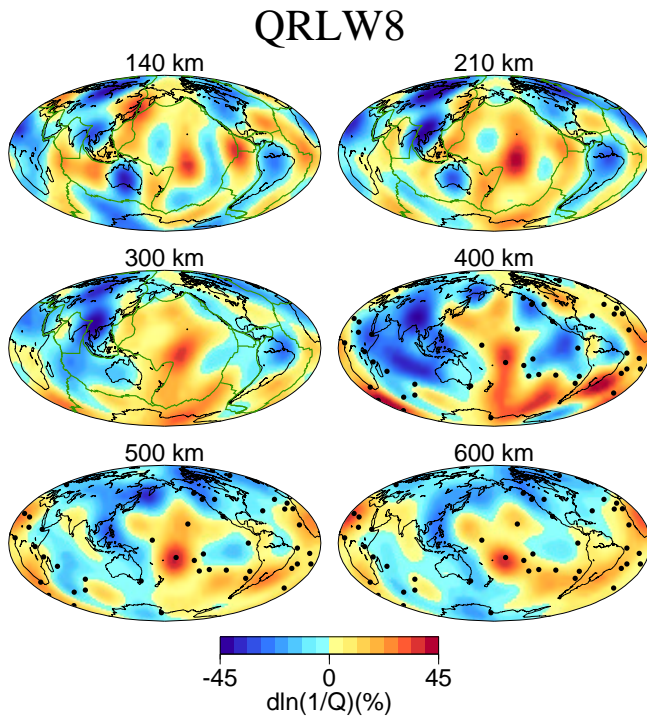


Figure 16.8: Images of model QRLW8 at six different depths. The lateral variations are expressed in terms of relative variations in $1/Q$ with respect to QL6: red and blue indicates regions of high and low attenuation, respectively. The distribution of hotspots is also shown, indicating its correlation with low Q

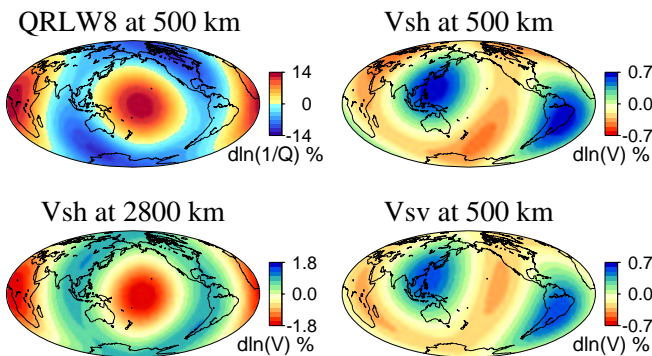


Figure 16.9: Comparison of the degree 2 distribution in Q in the upper mantle transition zone (depth of 500 km), for model QRLW8, with the corresponding distribution in SH and SV velocity as well as SH velocity at 2600 km in model SAW24B16

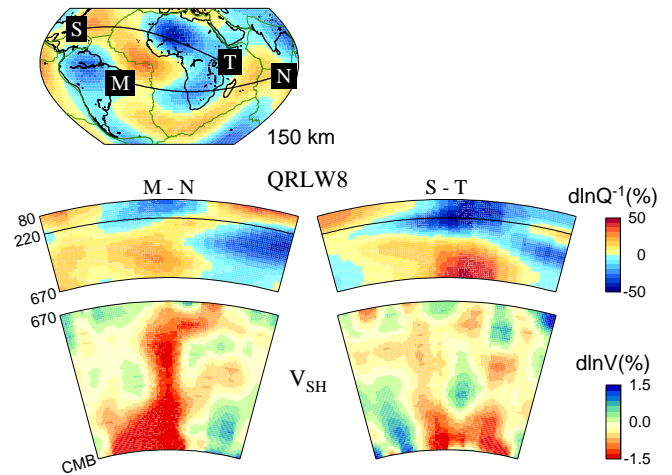


Figure 16.10: Depth cross-sections under Africa along profiles indicated in the top panel showing, for each profile (top to bottom), Q distribution in the upper mantle (to degree 8), and V_{SH} distribution in the lower mantle (to degree 24).

and in the Pacific, towards the East Pacific rise and the center of the Pacific plate. In the latter case, the flow is impeded on the west side by the presence of the Fiji-Tonga subduction zone. This deflection occurs at greater depths under the thicker continental lithosphere ($\sim 350\text{km}$, Fig. 3 b) than under the oceanic one ($\sim 200\text{km}$, Fig. 3a).

4.3 Acknowledgements

We thank the National Science Foundation for support of this research.

4.4 References

Forte, A. M. and J. X. Mitrovica, *Nature*, **410**, 1049 (2001)

Gung, Y.C. and B. Romanowicz, Q tomography of the upper mantle using three component long period waveforms, submitted to *J. Geophys. Res.*

Li, X.D. and B. Romanowicz, Global mantle shear velocity model developed using nonlinear asymptotic coupling theory, *J. Geophys. Res.* **101** 22,245 (1996).

Mégnin, C., and B. Romanowicz, The 3-D shear velocity structure of the mantle from the inversion of body, surface, and higher mode waveforms, *Geophys. J. Inter.*, **143** 709-728, 2001

Ritsema, J. , H. van Heijst and J. Woodhouse, Complex shear wave velocity structure imaged beneath Africa and Iceland, *Science* **286**, 1925-1928, 1999.

Romanowicz, B. and Y. C. Gung, Superplumes from the core-mantle boundary to the base of the lithosphere, *Science*, **296**, 513-516, 2002.

5. Progress in modeling deep mantle isotropic shear and compressional velocity structure using waveform inversion

Mark Panning and Barbara Romanowicz

5.1 Introduction

Seismic tomography is an important tool for determining the structure and dynamics of the Earth's mantle. It is a technique which utilizes geophysical inverse theory to use large amounts of seismic data (both travel times and waveforms) to model the elastic structure of the Earth. With the use of nonlinear asymptotic mode coupling theory (NACT) (*Li and Romanowicz, 1996*) and three component body and surface waveform data, we are able to model 3D isotropic shear and compressional velocity structure throughout the mantle.

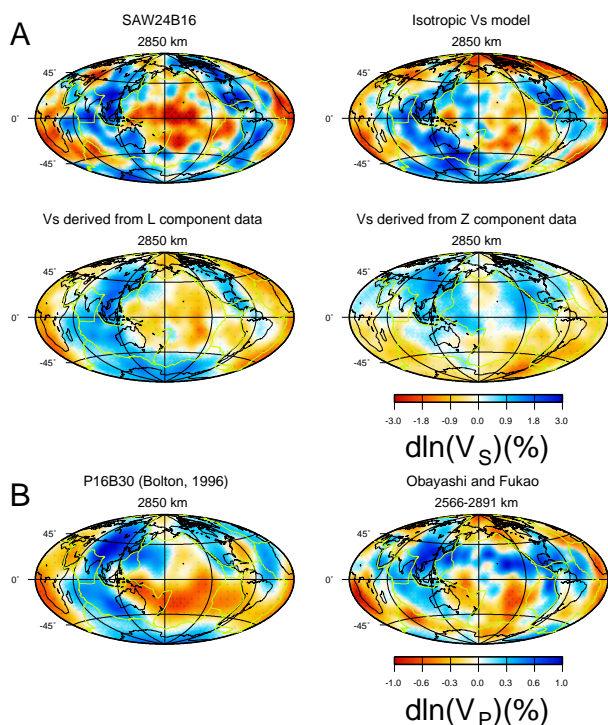


Figure 16.11: (A) Comparison of SAW24B16 and the isotropic S velocity model in the core-mantle boundary region. Inversions are also shown for only the L component data and only the Z component data. (B) P velocity models P16B30 (*Bolton, 1996*) and WEPP2 (*Fukao et al., 2001*) are shown for comparison.

While simultaneous models of shear and compressional velocity (or alternatively shear and bulk sound velocity) with P sensitivity based primarily on travel times (i.e. *Masters et al., 1999*) have been developed, very little

work has been done to explore V_P modeling using waveforms due to the higher dominant frequency of V_P data.

5.2 Degree 24 Isotropic S Velocity Model

We inverted 3 component body and surface wavepackets for mantle S velocity. We used SAW24B16 (*Mégnin and Romanowicz, 2000*), an SH velocity model based only on T component data, as a starting point. However, since our new model uses all three components of data, it is a model of isotropic V_S perturbations. The model obtained has similar T component variance reduction to SAW24B16, while performing significantly better for L and Z component data. Features in the uppermost mantle are what we would expect due to SV/SH anisotropy observed in other upper mantle models (e.g. *Ekström and Dziewonski, 1998; Montagner and Tanimoto, 1991*). An interesting difference can be seen between the two models in the western Pacific in the core-mantle boundary region (figure 16.11). The isotropic model has a pronounced fast anomaly in this area, while it is slow in the SH model. Resolution tests indicate this feature to be robust. Since this model differs from the SH model by including L and Z component data, we inverted only the latter datasets to see where the signal originates. While L component data produces a model similar to the SH model, the model from Z component data is quite different. Since most S sensitivity in the core-mantle boundary region is from vertically arriving phases such as SKS and Sdiff, which will primarily show up on the L component, this provides a hint that the signal may originate from V_P energy. This enters our model through an assumed $d(\ln V_S)/d(\ln V_P)$ scaling relationship. Figure 16.11 also shows two V_P mantle models. While the models differ, both show a fast anomaly in the western Pacific.

5.3 Waveform Inversion for P Velocity Structure

Due to the apparent V_P contamination in the isotropic V_S model, we tested whether we could perform a direct waveform inversion for V_P structure. Coverage tests indicate that there is some coverage throughout the mantle, although significantly less than V_S sensitivity. For the inversion, the S velocity was fixed to that of SAW24B16 truncated to degree 12, and the P velocity was perturbed from the PREM velocities. The degree 8 V_P model in figure 16.12 gives a variance reduction of 45% compared to 39% for truncated SAW24B16 with no P model. For long wavelengths, it is quite similar to P16B30 (*Bolton,*

1996), indicating the method has potential. With a more

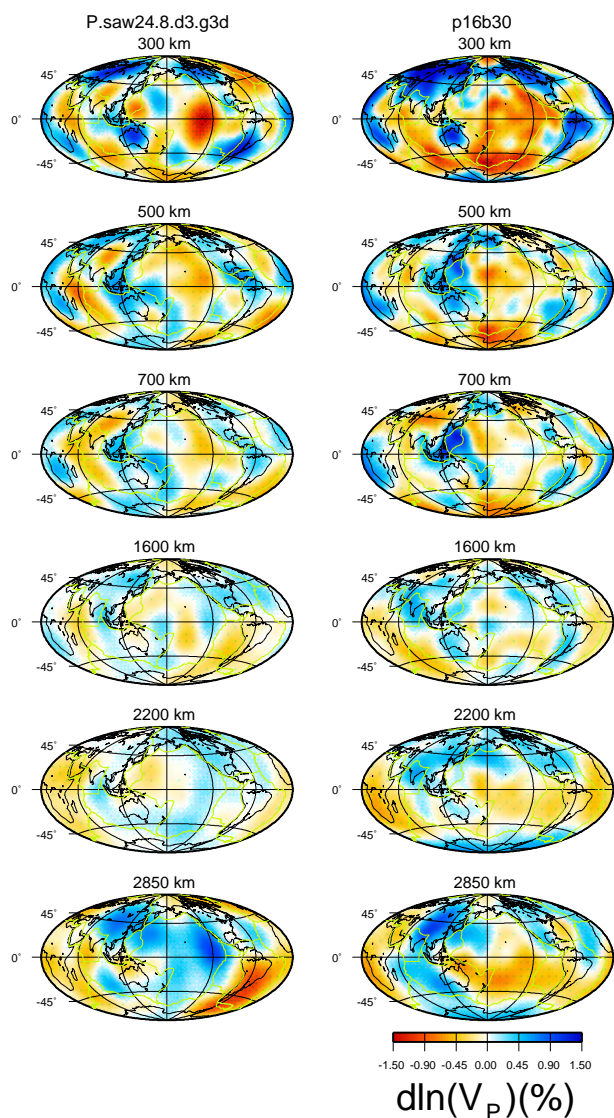


Figure 16.12: Comparison of P velocity models up to degree 8 for this study (left) and P16B30 (right).

optimal dataset (with periods shorter than 32s cutoff here and wavepackets better defined for P phases), a waveform inversion for V_P mantle structure appears to be feasible.

5.4 Conclusions

The degree 24 isotropic V_S model differs from SAW24B16 in several areas of the mantle. While these changes can be due to SV/SH anisotropy or other causes, the differences in the models in the core-mantle boundary region appear to be caused by V_P signal, indicating a potential breakdown in $d(\ln V_S)/d(\ln V_P)$ scaling relationships. Although more data coverage is needed, preliminary tests indicate modeling V_P structure using

waveform inversion is possible.

5.5 Acknowledgements

We thank the National Science Foundation for support of this research.

5.6 References

- Bolton, H., Long period travel times and the structure of the mantle. Ph.D. Thesis, La Jolla, 204 pages, 1996.
- Ekström, G. and A.M. Dziewonski, The unique anisotropy of the Pacific upper mantle, *Nature*, 394, 168-172, 1998.
- Fukao, Y., S. Widiyantoro and M. Obayashi, Stagnant slabs in the upper and lower mantle transition region, *Rev. of Geophys.*, 2001.
- Li, X.D., and B. Romanowicz, Global shear velocity model developed using nonlinear asymptotic coupling theory, *Jour. Geophys. Res.*, 101, 22,245-22,272, 1996.
- Masters, G., H. Bolton, and G. Laske, Joint seismic tomography for P and S velocities: How pervasive are chemical anomalies in the mantle? *EOS Trans. AGU*, 80 S14, 1999.
- Mégnin, C., and B. Romanowicz, The 3D shear velocity of the mantle from the inversion of body, surface, and higher mode waveforms, *Geophys. Jour. Intl.*, 143, 709-728, 2000.
- Montagner, J.P., and T. Tanimoto, Global anisotropy in the upper mantle inferred from the regionalization of phase velocities. *Jour. Geophys. Res.*, 95, 4797-4819, 1990.

6. Investigating Mantle’s density resolution using the Neighborhood Algorithm

Sébastien Rousset and Barbara Romanowicz

6.1 Introduction

Unlike travel times or waveform data, normal mode data are directly sensitive to density. However, the sensitivity kernels for density are much smaller than those for velocities, so the controversy about the possibility of resolution of the mantle’s density is still vivid, especially since the publication of model SPRD6 (*Ishii and Tromp, 1999*). Several authors (*Resovsky and Ritzwoller, 1999, Romanowicz, 2001, Kuo and Romanowicz, 2002*) objected that density cannot yet be constrained and the controversy is still going.

However the inversion processes used by previous studies all rely on least-square inversions and require the use of a starting model, the choice of which is critical for the reliability of the results. Unlike this simple inversion scheme whose result is one "best" model, stochastic methods sample the parameter space, and their result is a set of models whose statistical properties reflect the likelihood function. In this study, in order to investigate the resolution, we use the Neighbourhood Algorithm (*Sambridge 1999a,b*) which uses forward modeling to sample the parameter space preferentially where the fit is better. A second part of the algorithm can use this sampling set to retrieve quantitative information on the distribution of models.

6.2 Dataset and Model Parameterization

Theoretical background and dataset

We use a 2 steps inversion, as was done by *Ishii and Tromp* ; this method is simpler, but the coefficients measured may not correspond to a unique Earth model. Some studies (*Kuo and Romanowicz, 2002*) prefer a 1-step inversion, but this method is not practicable with the neighbourhood algorithm since the forward modeling of synthetic seismograms for each model would require too much computation.

During the first step, splitting coefficients (*Giardini and al., 1988*) of normal mode were obtained by non-linear inversion. Our dataset consist in splitting coefficients of 63 modes (*He and Tromp, 1996* and *Resovsky and Ritwoller, 1998*), corrected for the crust contribution and the effects of rotation. We have excluded a few modes for which 2 measurements were available but incompatible.

These coefficients are linearly related to the aspherical structure of the Earth considered as a perturbation δx of the elastic parameter x of our reference model PREM,

integrated over depth :

$$C_{st} = \int_0^a \left(\frac{\delta x}{x}\right)_{st}(z) K_s^x(z).dz \quad (16.1)$$

where s, t are degree and order in spherical harmonic expansion and a the Earth’s radius. The sensitivity kernel K_s^x is calculated for the reference model and depends only on the degree s of the expansion.

In this study, we limit ourselves to degree 2 perturbations and invert the 5 degree 2 splitting coefficients $C_{20}, C_{21}, S_{21}, C_{22}$ and S_{22} of the selected modes for the corresponding degree 2 structure of V_p, V_s and ρ in the mantle.

Inversion settings

The neighbourhood algorithm (NA) is a stochastic method comparable to Monte-Carlo method, genetic algorithm or simulated annealing (*Moosegard and Sambridge, 2002*). We are using the first part (*Sambridge 1999a*) of the algorithm to sample the parameter space preferentially in good fitting areas, using the geometrical construction of Voronoi cells (closest neighbourhood) to fill the space. At each iteration, n_s new models are randomly generated in the n_r best fitting cells, the cells being defined by all previously generated models. After a sufficient number of iterations, we obtain a large (about 150 000 for our problem) set of models with more models in good fitting areas. The parameters n_s and n_r must be tuned for each problem ; an important value is the parameter space dimension which largely governs the choice of n_s and n_r and seems to be the main limitation of the use of the algorithm : the concentration of models in good fitting areas failed for high dimension, at least in reasonable computation time.

Model parameterization

The model is naturally laterally parameterized by spherical harmonics, but we have the choice of the radial parameterization : layered models (equivalent to gate functions), splines functions, polynomials... Several trials show that 6 to 8 functions are a sufficient number to retrieve feature while keeping the total number of parameters low enough for use with the NA. Layered models oscillate and forcing them to be smooth causes instability and introduces arbitrary constraints that we would like to avoid. The splines-based parameterization that we selected allow smoother models.

6.3 Results

The most acceptable models are obtained when adding a spline-based model to the contribution of tomographic input models (Figure 16.13). The V_s perturbation is well retrieved while the V_p perturbation doesn't agree well with the input. The ρ perturbation is still oscillating, although smoother acceptable models exist.

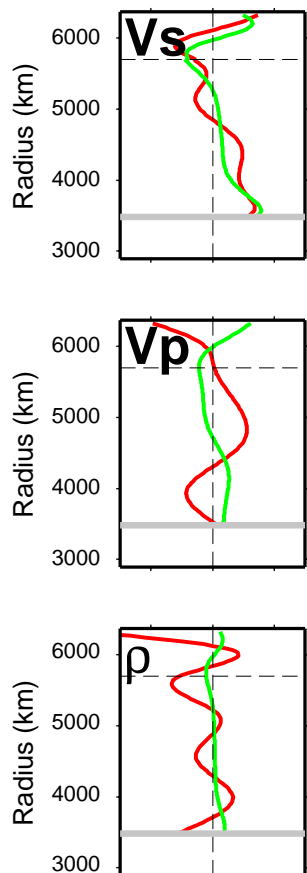


Figure 16.13: Best V_s model (black) obtained when using the tomographic (grey) model as input and 7 splines, for spherical harmonic coefficient C_{20}

One noteworthy feature of all parameterizations is the good fit between the V_s model obtained in our inversion of splitting coefficients and the V_s tomographic model, even when this model is not used as input, the difference residing mostly in the uppermost mantle where simple parameterization like ours is more likely to fail.

Figure 16.14 show the distribution of models for the C_{20} contribution of the shear velocity perturbation. This distribution is stable and satisfactory, giving good confidence in the uniqueness of the V_s solution, but is obtained using tomographic models as input and the stability if the result with respect to the choice of the input model remains to be tested.

Further work will make use of the second part of the

algorithm (Sambridge, 1999b) which use Bayesian integrals to analyze quantitatively the set of model obtained during the first part (or any other method generating a large set of models).

6.4 Acknowledgements

Special thanks to Malcolm Sambridge for making the NA software package available. This package, its very helpful online help and a short description of the algorithm can be found at <http://rses.anu.edu.au/~malcolm/na/na/html>

We thank the National Science Foundation for support of this research.

6.5 References

- Giardini, D., X.D. Li and J. Woodhouse, Splitting functions of long-period normal modes of the Earth, *J. Geophys. Res.*, *93* B11, 1988.
- He, X. and J. Tromp, Normal-mode constraints on the structure of the Earth, *J. Geophys. Res.*, *102*, 17981-17994, 1996.
- Ishii, M. and J. Tromp, Normal-Mode and Free-Air Gravity Constraints on Lateral Variations in Velocity and Density of Earth's Mantle, *Science*, *285*, 1231-1236, 1999.
- Kuo, C. and B. Romanowicz, On the resolution of density anomalies in the Earth's mantle using spectral fitting of normal mode data, *Geophys. J. Inter.*, in press
- Li, X.D., D. Giardini and J.H. Woodhouse, Large-Scale Three-Dimensional Even-Degree Structure of the Earth from Splitting of Long Period Normal Modes, *J. Geophys. Res.*, *91* B1, 551-577, 1991.
- Mosegaard, K. and M. Sambridge, Monte Carlo Analysis of inverse problems, *Inverse Problem*, *18* R29-R54, 2002.
- Romanowicz, B, Can we resolve 3D density heterogeneity in the lower mantle ?, *Geophys. Res. Lett.*, *28*, 15, 1107-1110, 2001.
- Resovsky, J. and M. Ritzwoller, Regularisation uncertainty in density model estimated from normal mode data, *Geophys. Res. Lett.*, *26*, 15, 2319-2322, 1999.
- Resovsky, J. and M. Ritzwoller, New and refined constraints on 3D Earth structure from normal modes below 3mHz., *J. Geophys. Res.*, *103*, 783-810, 1998.
- Sambridge, M., Geophysical inversion with a neighbourhood algorithm I - Searching a parameter space, *Geophys. J. Int.*, *138*, 479-494, 1999.
- Sambridge M., Geophysical inversion with a neighbourhood algorithm II - Appraising the ensemble, *Geophys. J. Int.*, *138*, 727-746, 1999.

Results for Saw_spl3 Vs c20

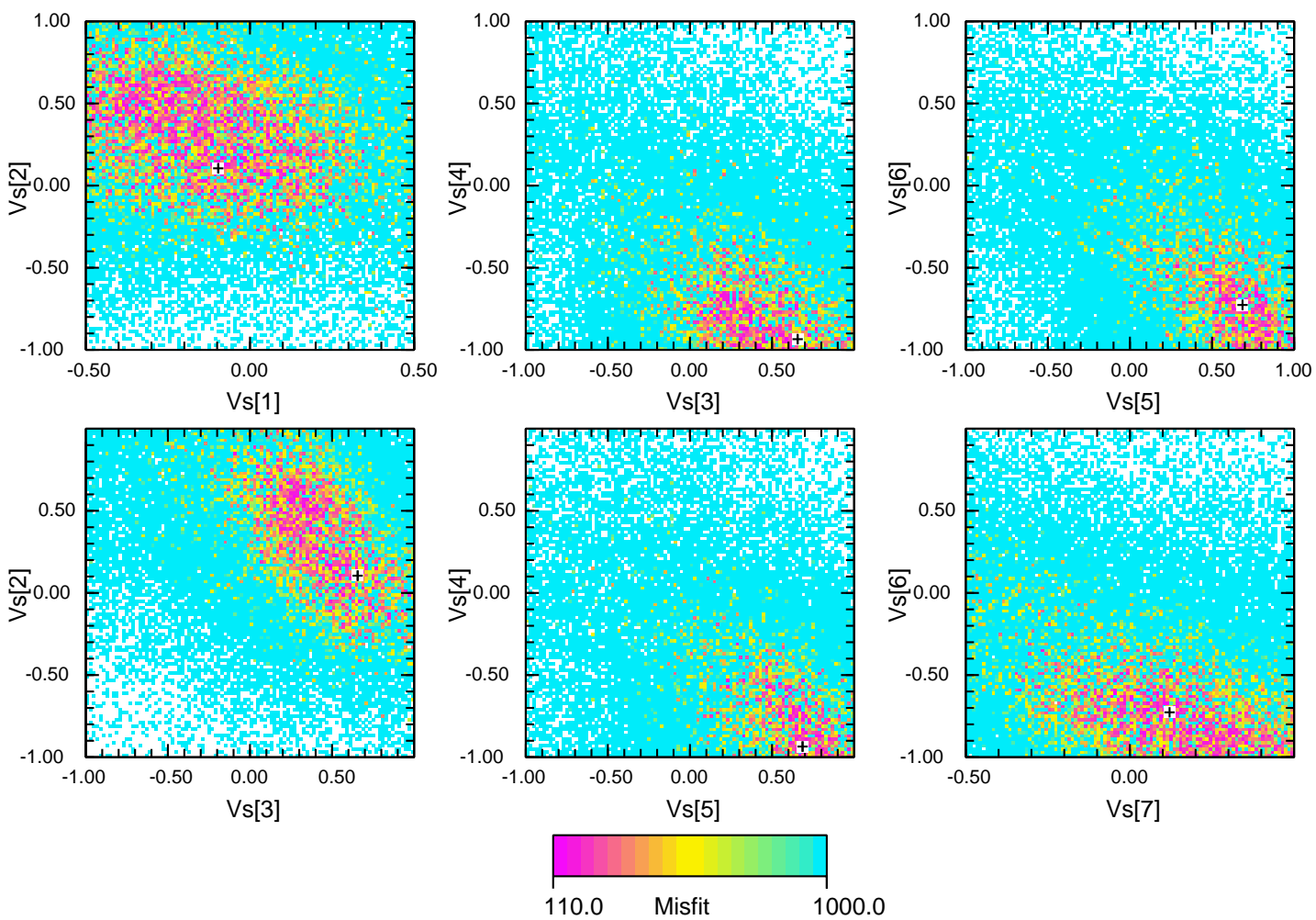


Figure 16.14: Projections of the set of V_s models obtained as output of the NA program ; $Vs[x]$ is the value of the coefficient for the x^{th} spline, 1 being the deepest and 7 the most shallow spline.

7. Towards Forward Modeling of 3D Heterogeneity at the Base of the Mantle

Akiko To, Yann Capdeville and Barbara Romanowicz

7.1 Introduction

At the base of the mantle, strong lateral variations in S velocity structure and anisotropy have been documented, in recent years, at the borders of the two large superplumes in the central Pacific and under Africa. These features undoubtedly hold important clues for understanding the dynamics of the earth's mantle. Current tomographic models of S velocity represents good starting models to fit travel times and some aspects of S and ScS waveforms along selected profiles sampling these regions (e.g. Bréger and Romanowicz, 1998; Breger et al., 2001). Increasing the strength of heterogeneity while keeping the original distribution of velocity highs and lows goes a long way towards explaining the observed trends.

However, these results point to the complex 3D nature of this heterogeneity, appropriate forward modeling tools need to be developed to handle strong 3D heterogeneity in this region, at relatively short periods and including diffracted waves. The coupled mode/spectral element method developed by Capdeville et al.(2001) and adapted to a heterogeneous layer (i.g. D'') between two spherically symmetric shells affords both numerical accuracy and the computational efficiency for this purpose.

Our goal is to extend the forward modeling approach of D'' structure (Bréger and Romanowicz, 1998), so far limited to travel times, to also include waveforms, applying the hybrid spectral element method and further explore 3D structure and anisotropy at the base of the mantle.

7.2 Work plan and Preliminary result

First, we will collect the waveforms of core sensitive phases (Sdiff,SKS,SKKS,ScS) and measure differential travel times within them. Then, starting from the tomographic model, we will adjust the strength and boundaries of the velocity structure to match differential travel times between Sdiff -SKS,Sdiff-SKKS and ScS-S . The advantage of this approach is that while it uses an infinite frequency approximation and therefore inaccurate to model broadband S travel times, it is very expedient and allows to rapidly get closer to an adequate final model. Finally, we will refine the model by computing numerical synthetics in 3D.

Fig 16.15 shows the preliminary result of the comparison between synthetics from 1D, 3D model and observations. 1D synthetics are calculated from PREM (Dziewonski and Anderson, 1981) by normal mode summation. 3D synthetics are calculated from the model

which has 3D structure of SAW24b16 (Megnin and Romanowicz, 2000) at the bottom 370 km of the mantle and sandwiched by PREM for the other part of the Earth. It is calculated by hybrid spectral element and modal summation method. Sdiff and sSdiff phase are shown. 3D model fits better to the observation especially for stations with longer distance (KBS,BOSA,LMN). For some stations, time shift for 3D is too strong (INK,YKW3) and sometimes both amplitude and time shift are poorly explained (CCM).

7.3 Acknowledgement

We thank the National Science Foundation for support of this research.

7.4 References

- Bréger, L. and B. Romanowicz, Thermal and Chemical 3D heterogeneity in D'', *Science*, 282, 718-720, 1998
- Bréger, L., B. Romanowicz and C. Ng, The Pacific plume as seen by S,ScS and SKS, *Geophys. Res. Lett.*, 28, 859-1862, 2001.
- Capdeville Y., E. Chaljub, J.P. Vilotte and J.P. Montagner, Coupling the Spectral Element Method with a modal solution for Elastic Wave Propagation in Global Earth Models, **accepted** in *Geophys. J. Int*, 2001
- Dziewonski A.M. And D.L. Anderson, Preliminary reference Earth model, *Phys. Earth Planet. Inter.*, 25, 297-356, 1981.
- Megnin, C. and B. Romanowicz, The shear velocity structure of the mantle from the inversion of of body, surface and higher modes waveforms, *Geophys. J. Int*, 143, 709-728, 2000

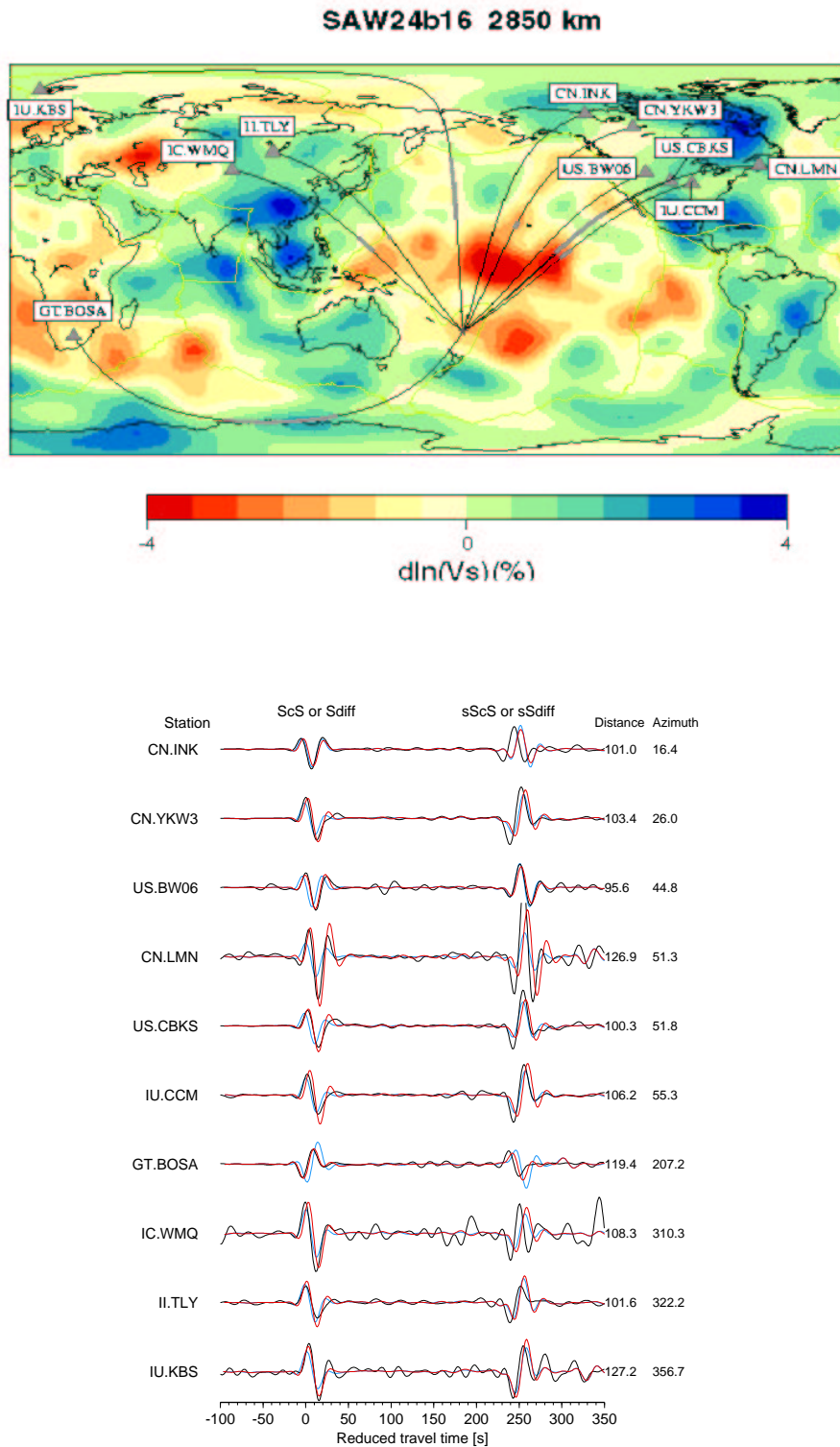


Figure 16.15: Top: The background model is the a velocity tomographic model SAW24b16 just above the CMB. Path between source and stations are plotted. The diffracting portions of Sdiff phase are plotted by bold gray. Bottom: Comparison between data (Black), synthetics for the PREM model (blue) and synthetics for SAW24B16+PREM (red).

8. Using the Coupled Method of Spectral Elements and Modal Solution to study the D'' layer.

Yann Capdeville, Barbara Romanowicz, Akiko To

8.1 Introduction and Research objectives

The D'' region, which encompasses the last 300 km or so of the deep mantle, is thought to be both a thermal and a chemical boundary and the site of vigorous dynamic processes. Its structure is believed to hold the key to many largely unanswered questions in deep Earth geodynamics, such as the ultimate fate of subducting slabs, the origin of hotspots, the amount of bottom heating driving global mantle circulation, electro-magnetic coupling between the core and the mantle, and the nature of chemical heterogeneity in the deep mantle. Strong lateral variations in D'' as well as the presence of topography on the fluid-solid core mantle boundary, has to be addressed by forward modeling approaches. However, present global waveform modeling can not handle wave propagation in this region of the Earth. Another difficulty is that the relevant frequency cutoff is high (0.1 Hz or higher) which leads to very high costs of numerical simulations. The coupled method of Spectral Elements and Modal Solution is very well adapted to such a problem by allowing to restrict the 3D model in the D'' layer and to use a spherically symmetric model is enough in the rest of the Earth. Until now, this method is the only one able to address 3D wave propagation in this region at realistic frequencies. By producing synthetic seismograms using the coupled method in different D'' layer models and confront them to real data, we hope to provide significant advances to our understanding of this region, especially using both amplitude and time shift informations of data.

8.2 Method

This work is based upon an extension to the coupling scheme of the Spectral Element Method (SEM) with a normal mode solution in spherical geometry. This extension allows us to consider a thin spherical shell of spectral elements between two modal solutions above and below. The SEM is based on a high order variational formulation in space and a second-order explicit scheme in time. It combines the geometrical flexibility of the classical finite element method with the exponential convergence rate associated with spectral techniques. In the inner sphere and outer shell, the solution is sought in terms of a modal solution in the frequency domain after expansion on the spherical harmonics basis. The SEM has been shown to obtain an excellent accuracy in solving the wave equation in complex media but is still numerically expen-

sive for the whole Earth for high frequency simulations. On the other hand, modal solutions are well known and numerically cheap in spherically symmetric models. By combining these two methods we take advantage of both, allowing high frequency simulations in global Earth models with 3D structure in a limited depth range. Within the spectral element method, the coupling is introduced via a dynamic interface operator, a Dirichlet-to-Neumann (DtN) operator which can be explicitly constructed in the frequency and generalized spherical harmonics domain using modal solutions in the inner sphere and outer shell. The presence of the source and receivers in the top modal solution shell requires some special treatment. The accuracy of the method is checked against the mode summation method in simple spherically symmetric models and shows very good agreement for all type of waves, including diffracted waves traveling on the coupling boundary.

Simulations in a 3D D'' layer model based on the tomographic model SAW24B16 has been performed up to a corner frequency of 1/12 s. The mesh used is presented on Fig. 16.16. The comparison with data using deep

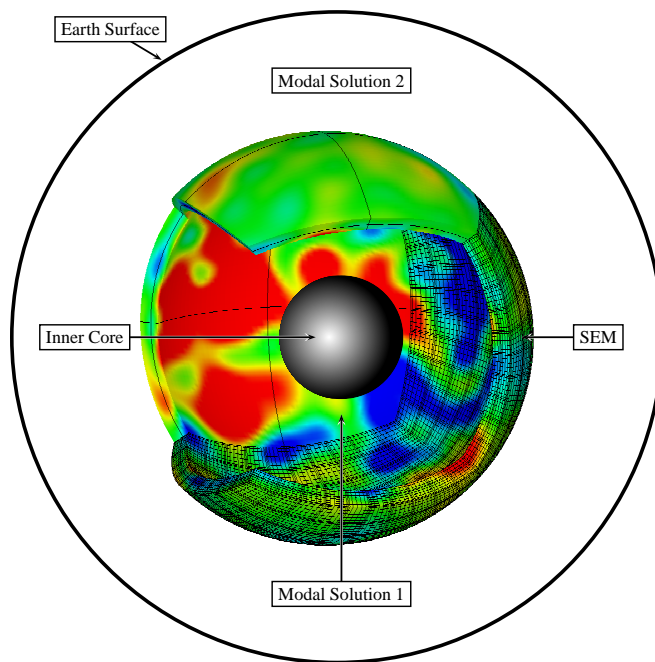


Figure 16.16: Sandwich of spectral elements between two modal solutions for D'' application with SAW24B16 model.

events shows surprisingly good results for the 3D model even when the observed waveform amplitudes differ significantly from the ones predicted in the spherically symmetric reference model (PREM). Some examples of synthetics are given on Fig. 16.17.

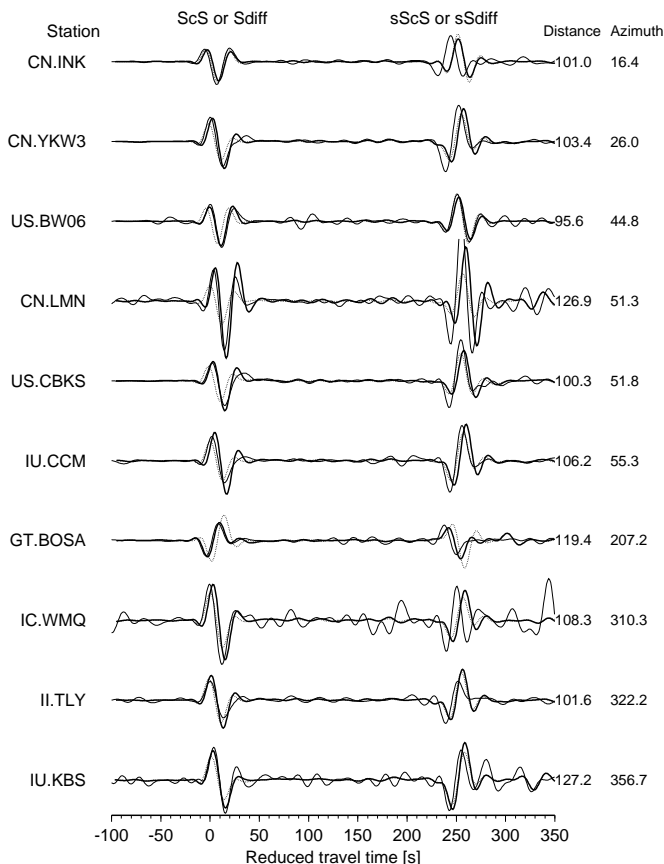


Figure 16.17: Comparison between data (thin line), synthetics in PREM (dotted line) and synthetics in SAW24B16 + PREM (bold line) for an event in the Fidji Island recorded at different stations around the world.

A description of the method with illustrations can be found on <http://www.seismo.berkeley.edu/~yann>

8.3 Accomplishments during 2001-2002

The accomplishments achieved during 2000-2001 include:

- Technical and practical developments and optimizations of the code on the IBM SP of the NERSC.
- Comparison of synthetics seismograms in the tomographic model SAW24B16 and data for several deep events. These comparisons will lead to an improved model of the D" layer.

8.4 Acknowledgements

The computation were made using the computational resources of the NERSC, especially the IBM SP, under repo mp342.

We thank the Miller Insitute for their support.

8.5 References

Y. Capdeville, B. Romanowicz and A. To, Coupling Spectral Elements and Modes in a spherical earth: an extension to the "sandwich" case. **Submitted** to *Geophys. J. Int.*, 2002.

Capdeville Y., C. Larmat, J.P. Vilotte and J.P. Montagner, Numerical simulation of the scattering induced by a localized plume-like anomaly using a coupled spectral element and modal solution method. **In press** in *Geoph. Res. Lett.*, 2001.

Capdeville Y., E. Chaljub, J.P. Vilotte and J.P. Montagner Coupling the Spectral Element Method with a modal solution for Elastic Wave Propagation in Global Earth Models. **accepted** in *Geophys. J. Int.*, 2001.

Chaljub, E. Capdeville, Y. and Vilotte, J.P., Solving elastodynamics in a solid heterogeneous 3D-sphere: a parallel spectral element approximation on non-conforming grids. **Submitted** to *J. Comp Phy.*, 2001.

9. Short scale heterogeneity in the lowermost mantle: insights from PcP-P and ScS-S data

Hrvoje Tkalčić and Barbara Romanowicz

9.1 Introduction and Motivation

An important question in global geodynamics is whether the 3D seismic velocity anomalies, as seen in tomographic models of the mantle, are of a thermal or a compositional nature, or a combination of both. While global tomographic S models consistently show predominance of long wavelength structure at the base of the mantle, and in particular two large slow domains in the central Pacific and under Africa, referred to as "superplumes", seismic evidence for shorter scale heterogeneity at these depths is growing. The existence of strong heterogeneity in the vicinity of the two superplumes has been documented through forward modeling of seismic travel times and waveforms. Recent studies have also found evidence for locally rapid variations in other areas such as middle America.

On the other hand, several studies have compared global variations in S and P velocities from tomographic inversions, and some of them found evidence for a strong increase in $R = \partial \ln V_s / \partial \ln V_p$ near the bottom of the mantle, as well as a possible decorrelation between shear and acoustic velocity variations below 2000 km depth. Furthermore, while there is evidence for zones of strongly reduced P velocity at the base of the mantle, there is no evidence that these are accompanied with a comparable drop in S velocity.

Through an inversion of PcP-P and PKP(AB-DF) data, we recently obtained maps of D" with lateral P velocity variations that show much shorter wavelength features than seen in S tomographic models (Tkalčić *et al.*, 2002). Here, we consider PcP-P and ScS-S travel time residuals, and analyze their spatial relationship in several regions which are sampled both by PcP and ScS, in comparison to tomographic maps. We discuss implications of our results for the relative variations in P and S velocities in the lowermost mantle, in particular from the stand-point of $\partial \ln V_s / \partial \ln V_p$ ratios and their interpretation.

9.2 Results

We compared the lateral variations observed in a global dataset of PcP-P differential travel times sensitive to structure in the bottom 500-1000 km of the mantle, to the predictions of global tomographic models, on the one hand, and ScS-S differential travel times, on the other.

This comparison has shown that the different datasets are in good agreement in some regions, in particular in eastern Asia, where fast anomalies over a broad domain

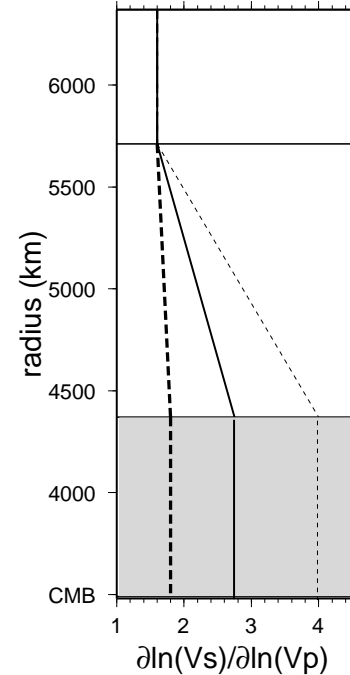


Figure 16.18: Best fitting depth profiles of $R = \partial \ln V_s / \partial \ln V_p$ obtained by comparing PcP-P travel time data to S tomographic velocity models, using a parameter search for the thickness of the bottom layer and the value of R inside it. Comparison restricted to a subset of PcP-P residuals with PcP reflection points under eastern Eurasia with global S tomographic models *SAW24B16* (Méglin and Romanowicz, 2000) (solid line, variance reduction 57%), and models *SB4L18* (Gu and Dziewonski, 2001) and *S362D1* (Masters *et al.*, 2000) (thick dashed line, variance reduction 60% and 52%, respectively). The thin dashed line corresponds to the best fitting depth profile of R using the global PcP-P dataset and model *SAW24B16* (variance reduction 10%). Shaded area represents the uncertainty in the thickness of the lowermost layer for the parametrization used.

are inferred both from tomographic P and S models and from the core-reflected phase data, resulting in a value of R compatible with a thermal origin of heterogeneity at the base of the mantle in this region (solid and thick dashed lines in Figure 16.18). It is interesting to compare this regional result with that obtained by applying the same methodology to the global dataset. The best variance reduction is obtained for model *SAW24B16* (Mégnin and Romanowicz, 2000) and does not exceed 10%. Figure 16.18 also shows the best fitting R profile (thin dashed line) obtained with this model.

On the other hand, the PcP-P data indicate shorter scale lateral variations in many other regions. We studied in detail two such localized regions, under central America and south-east Africa, which correspond to downwelling and upwelling regions respectively, as seen in global tomographic models. In central America, lateral variations in P and S velocity appear to track each other. With only a few exceptions, the variations in PcP-P residuals are in good agreement with the slow (resp. fast) regions delineated by ScS-S from the study of Wyssession et al. (2001). Resulting estimates of the ratio R in the last 500 km of the lower mantle are not particularly high. Under Africa (Figure 16.19a), one profile (AB) shows similar results (Figure 16.19b), whereas a slightly more northerly neighboring path (profile CD) indicates fast P velocities in the heart of the low S velocity African "plume" (Figure 16.19c). A similar situation is found on the eastern edge of the Pacific plume, where the simultaneous availability of PcP-P and ScS-S data allows us to infer the existence of sharp lateral gradients across compositionally different domains.

Our study documents existence of strong lateral variations at the base of the mantle on scale lengths of several hundred kilometers, implying the existence of compositional variations in D". We note however that the computation of meaningful estimates of R at the base of the mantle, as an indicator of the nature of heterogeneity, remains a challenge. In order to do it correctly, better spatial sampling in both P and S data is needed, as different smoothing of short scale structures can lead to biased estimates.

Collecting more PcP-P and ScS-S data with a compatible sampling of the lowermost mantle on the one hand, and increasing the resolution and accuracy of tomographic models on the other is necessary to gain further insight regarding the nature of heterogeneity in the lowermost mantle.

9.3 Acknowledgements

Data were obtained from the IRIS Data Management Center. We thank Nicolas Houy, who measured most of the PcP-P travel times used in this study and Michael Wyssession for sharing his MOMA S-ScS dataset with us. Figures were made with the General Mapping Tools (P.

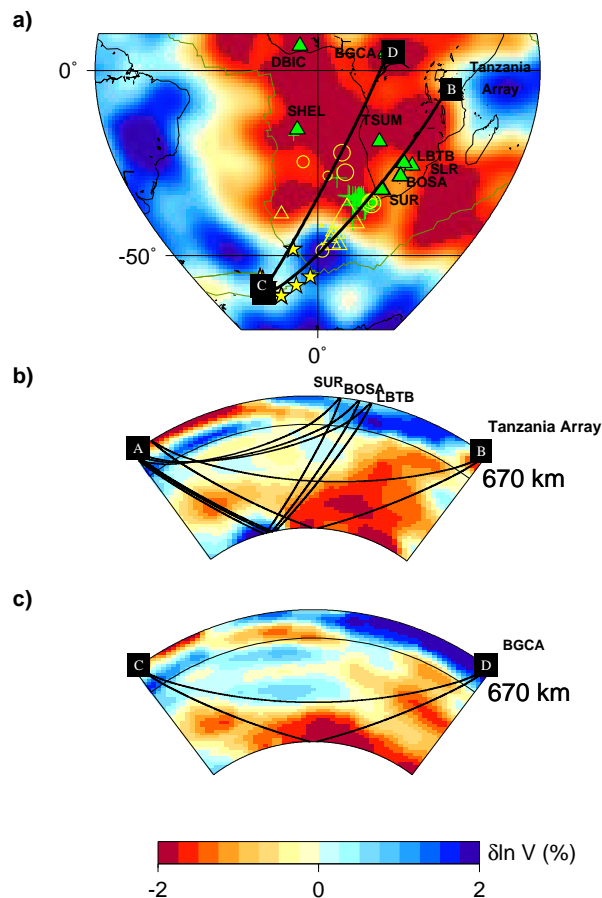


Figure 16.19: PcP-P travel time residuals plotted at the surface projections of PcP bouncing points for south Atlantic/south Africa region. The largest triangle and circle correspond to residuals of +3 s and -1.5 s, respectively. The background model is *SAW24B16*. Green crosses are ScS reflection points. (b) Cross-section through *SAW24B16* along profile AB, with P and PcP paths from a South Sandwich Islands region event to SUR, BOSA and LBTB stations and a south Atlantic ridge event to Tanzania network; (c) Cross-section through *SAW24B16* along profile CD, with P and PcP paths from a South Sandwich Islands region event to BGCA station.

Wessel and W. H. F. Smith, *EOS Trans. AGU* **76**, 329, 1995).

We thank the National Science Foundation for support of this research.

9.4 References

Gu, Y., A.M. Dziewonski, Shear velocity of the mantle and discontinuities in the pattern of lateral heterogeneities, *J. Geophys. Res* 106, 11169-11199, 2001.

Masters, G. , G. Laske, H. Bolton, and A.M. Dziewonski, Earth's Deep Interior: Mineral Physics and Tomography From the Atomic to the Global Scale. *Geophys. Monogr. Ser. (eds Karato. S.-I. et al.)* 117, AGU, Washington, DC, 63-87, 2000.

Mégnin, C., B. Romanowicz, The 3D shear velocity structure of the mantle from the inversion of body, surface, and higher mode waveforms, *Geophys. J. Int.*, 143, 709-728, 2000.

Tkalčić, H., B. Romanowicz, N. Houy, Constraints on D'' structure using PKP(AB-DF), PKP(BC-DF) and PcP-P travel time data from broadband records, *Geophys. J. Int.*, 148(3), 599-616, 2002.

Tkalčić, H., B. Romanowicz, Short scale heterogeneity in the lowermost mantle: insights from PcP-P and ScS-S data, *Earth Planet. Sci. Lett.*, 201(1), 57-68, 2002.

Wyssession, M.E., K.M. Fischer, G.I. Al-eqabi, P.J. Shore, Using MOMA broadband array, ScS-S data to image smaller-scale structures at the base of the mantle, *Geophys. Res. Lett.*, 190, 167-170, 2001.

Part IV
Appendices

